

The Year of the Solar System 2014 Undergraduate Research Conference

Sponsored by:

**NASA Science Mission Directorate
Lunar and Planetary Institute**

Welcome to the 2014 YSS Undergraduate Research Conference

Hello, Everyone!

The YSS Undergraduate Research Conference was created out of a series of conversations between planetary science faculty and the NASA education community regarding the kinds of professional development young scientists need. All of us remember what our first professional scientific conference was like – everyone seemed to know everyone else (though we didn't), we couldn't decide which sessions to go to, and often it was our first time presenting our work to a broader community. Many of us felt it would have been much easier to transition into our chosen field if we had practice and perhaps a guide.

As part of the NASA Science Mission Directorate (SMD) Year of the Solar System, you being given the opportunity to hold a conference of your own, just for undergraduate researchers. You have come from all across the United States, indeed the world, and are at different stages of your own professional development. Some of you already know that you want to be scientists, and others of you may not be quite sure yet. Some of you come from big universities with big laboratories where there are a lot of scientists. Others of you come from smaller schools where the number of scientists is smaller. Some of you have presented your science results before, for others, this is your first time. Regardless of where you are on this continuum, the Undergraduate Research Conference is for you!

2014 marks the fourth year of this conference and every year it has been a great success. I want to thank the people that have made the YSS Undergraduate Research Conference possible. Funding for the conference comes from a NASA SMD grant. The Lunar and Planetary Institute has been essential in providing logistical support and is a primary sponsor of the conference. Special thanks go to Stephanie Shipp, Christine Shupla, Yolanda Ballard, Heather Dalton, Kira Honnoll and Stephen Mackwell. I also would like to thank Sanlyn Buxner and Emily Joseph with the Planetary Science Institute, as well as the panelists that are giving their time for the morning sessions.

I am looking forward to hearing about your work and learning where you are headed!

Andrew Shaner
Education Specialist
USRA – Lunar and Planetary Institute
Houston, TX

2014 YSS Undergraduate Research Conference

- 8:45 a.m. Registration**
- 9:00 a.m. Welcome Remarks**
Andy Shaner, Lunar and Planetary Institute
- 9:15 a.m. Panel: Choosing a Graduate School That's Right for You!**
Dr. Aaron Cavosie, University of Puerto Rico
Dr. Georgiana Kramer, Lunar and Planetary Institute
Dr. Amanda Nahm, University of Idaho
- 10:00 a.m. Break**
- 10:15 a.m. Panel: Women in Planetary Science**
Dr. Jennifer Grier, Planetary Science Institute
Dr. Nina Lanza, Los Alamos National Laboratory
Dr. Cassandra Runyon, College of Charleston
- 11:00 a.m. Break**
- 11:15 a.m. Panel: Alternative Careers in Science**
Barbara David, Space Science Education Journalist & Consultant
Brooke Hsu, Lunar and Planetary Institute
Dr. Kelly Kolb, ExxonMobil
- 12:00 p.m. Lunch**
- 1:00 p.m. Poster Presentations**
Even abstract numbers present during the first hour
Odd abstract numbers present during the second hour
Open round of questions during the third hour
- 4:00 p.m. Closing Remarks**
Andy Shaner, Lunar and Planetary Institute
- 4:15 p.m. Evaluation**
Dr. Sanlyn Buxner, Planetary Science Institute
Emily Joseph, Planetary Science Institute
- 5:00 p.m. Close**

Sunday, March 16, 2014

POSTER SESSION: 2014 YSS UNDERGRADUATE RESEARCH CONFERENCE

1. Albright J. A. Ferrin P. C. Grosfils E. B.
Developing Mapping-Derived Strain Estimates for Giant Radial Lineament Systems on Venus
A new mapping-based method for estimating the total hoop strain along radial lineament systems on Venus, as well as two possible methods for data correction, are proposed and evaluated as a means of investigating feature origins.
2. Arana Morales A. Cavosie A. J.
A Study of Shocked Quartz in Breccia from The Rock Elm Impact Structure
The presence of quartz with planar fractures confirms an impact origin of the breccia found in the Rock Elm Impact Structure.
3. Boatwright B. D. Fassett C. I.
Exploring the Morphometry of Martian Valley Networks and Drainage Basins Using the MARSSIM Landform Evolution Model
Description of the model; initial results using idealized ridge topography to understand how a variety of geomorphic parameters affect Hack's exponent.
4. Boyce J. W. B. Tomlinson S. M. T.
How Can Wet Apatite be Found on a Dry Moon?
Hydrogen rich apatite found in lunar volcanic rocks does not imply an H rich bulk lunar melt, but actually the loss of fluorine through fractional and equilibrium crystallization.
5. Bramble M. S. Flemming R. L. McCausland P. J. A.
Grain Size, 'Spotty' XRD Rings, and CheMin: Two-Dimensional X-ray Diffraction as a Proxy for Grain Size Measurement in Planetary Materials
A 2D XRD grain size estimation is performed on minerals of known sieve fraction grain sizes, and then applied to 2D XRD data from the Mars Science Laboratory.
6. Brown J. J. Thompson L. M. Spray J. G.
Modification-Stage Tectonics Prior to Melt Sheet Emplacement: Constraints from the Manicouagan Impact Structure
Presence of a sedimentary cover to Precambrian metamorphic basement at the time of impact at Manicouagan allows us to constrain modification-stage tectonics.
7. Challa S. P. Scowen P. A. Miller A. D. Veach T. J.
Focal Plane Actuation to Achieve Ultra-High Resolution on Suborbital Balloon Payloads
This project aims to improve the resolution of balloon-borne telescopes by actuating the focal plane to counteract movements caused by small scale jitter. The goal is to reduce the pointing error to within 0.1 arcseconds.

8. Clayton A. N. Strait M. M. Flynn G. J. Durda D. D.
Disruption Experiments with an Artificially Hydrated Ordinary Chondrite
A new method was developed to artificially hydrate an ordinary chondrite. These carbonaceous chondrite analogues were used in disruption experiments.
9. Colón Lugo D. Cavosie A. J.
Detrital Shocked Muscovite from the Santa Fe Impact Structure (USA).
A classification for kink bands was determined based on the geometry of the microstructures found in mica grains from the Santa Fe impact structure using TL and SEM images. EMPA data was acquired to provide a comparison with other shocked mica.
10. Dapremont A. Allen C. Runyon C.
The Gale Crater Mound in a Regional Geologic Setting: Comparison Study of Wind Erosion in Gale Crater and Within a 1000 km Radius
Lower and middle member Medusae Fossae Formation (MFF) yardangs were compared with those of Gale Crater. MFF yardangs exhibited orientations most closely related to the UM of Gale suggesting a varied wind regime history dominated by NW-SE winds.
11. Davis A. C. Bishop J. L. Veto M. Ruff S. Bristow T. Gates W. Blake D.
Comparing VNIR And TIR Spectra of Clay-Bearing Rocks
Coordinated VNIR and TIR spectra were performed on clay-bearing rocks in order to compare these natural analogs with Martian spectra from CRISM and TES.
12. Djordjevic S. Mickol R. L. Kral T. A.
Simulating Martian Conditions: Methanogen Survivability During Freeze-Thaw Cycles
Methanogens are obligate anaerobes found in extreme conditions that use molecular hydrogen as an energy source and carbon dioxide as a carbon source. It is proposed that these Archaea are able to persist and grow in Martian conditions.
13. Feng W. Evans C. Gruener J. Eppler D.
Comparing Geologic Data Sets Collected by Planetary Analog Traverses and by Standard Geologic Field Mapping: Desert Rats Data Analysis
The objective of this project is to produce a geologic map from data collected on an analog mission using Apollo-style traverses and remote sensing data. This map is compared with a geologic map produced using standard field techniques.
14. Frushour A. M. Noble S. K. Christoffersen R. Keller L. P.
Alteration of Lunar Rock Surfaces Through Interaction with the Space Environment
Six lunar rock thin sections with patina are identified, described, and classified from petrographic microscope and SEM observations.
15. Garcia G. C. Fenton L. K.
Determining the Dune-Constructing Wind Regime in Eastern Olympia Undae, Mars.
By observing the morphology of dunes in the eastern region of the Olympia Undae sand sea with the use of HiRISE imagery, data was collected about the orientation of dunes based on size, and how these features are being altered by a new wind regime.

16. Hansen K. T. Osinski G. R.
Revisiting Shatter Cones at Sudbury
Shatter cones in the Sudbury area have lacked detailed study since their discovery. A comprehensive study and GIS mapping of shatter cones continuing in Summer 2014 will provide a greater understanding of these features, as well as the crater itself.
17. Hay H. C. F. C. Collins G. S. Davison T. M.
Complex Crater Collapse: A Comparison of the Block and Melosh Models of Acoustic Fluidization
We compare two models of dynamic weakening in numerical simulations of impact crater formation. Localized regeneration of acoustic energy facilitates collapse.
18. Hernandez J. A.
Geomorphological Features Indicative of Upwelling Groundwater on Mars
In this research, strong geomorphological evidences of groundwater outcrops on the Martian surface, seen in various photographs of the HiRISE (University of Arizona), are reported in the middle section of Cerberus Fossae, and the top Athabasca Valles.
19. Hernandez D. J. Gulic V. C. Narlesky C. A.
Gullies on Mars: Fluvial Geologic Processes as Evidence for Liquid Water on Mars.
Mars Reconnaissance Orbiter HiRISE images show insight into past and present martian geologic activities that provide evidence of present day liquid water.
20. Hopkins R. H. Tornabene L. L. Osinski G. R. McEwen A. S.
Spectral and Morphologic Mapping of the Elorza Crater, Mars
Determining which rocks existed pre-impact, were altered during the impact process, or were deposited after impact in the Elorza Crater, Mars. By analyzing spatial and spectral data, the origin of rocks in the central uplift may be determined.
21. Jack S. J. Strait M. M. Flynn G. J. Durda D. D.
Using Porous Material to Simulate Asteroid Disruption
Results of disruption patterns using pumice to simulate highly porous asteroids.
22. Landry B. L. Munsill L. C. Collins G. C. Mitchell K. L.
Observation About Boulders on the South Polar Terrain of Enceladus
Images were produced from Cassini ISS data. High resolution images were analyzed for boulder number and size. High resolution images were used to classify the South Polar Region based on several qualifiers.
23. Leverone R. L.
Titanium isotopic compositions in lunar and terrestrial samples: Implications for lunar origin
Titanium isotope compositions of Geostandards in comparison to Lunar samples.
24. Lorenzo A. M. Jr.
Simplistic Mass-Radius Relationships of Exoplanets
We develop a simple program to derive a relationship between the mass and radius of exoplanets.

25. Lugo Centeno C. M. Cavosie A. J.
First Report of Shocked Zircon at the Santa Fe Impact Structure (USA).
Documentation of planar fractures in zircons from the Santa Fe impact structure, USA.
26. Martin D. J. P.
New Geological Map of the Orientale Basin
A new geological map is presented with descriptions and analyses of units both inside and outside of the basin. Properties of the impact and melt sheet are discussed.
27. Martone A. M. Glotch T. D.
The Effect of Grain Size and Abundance on the Deconvolution of Mixtures Using the Shkuratov Model
We use the Shkuratov radiative transfer model to obtain mineral optical constants, and test the model's ability to deconvolve reflectance spectra of mineral mixtures and determine mineral grain sizes and abundances.
28. McDonald G. D. Hayes A. G. Ewing R. C. Tokano T. Lucas A. Chen G.
Examining Effects of Orbital Forcing on Titan's Dune Orientations
We explore the possibility that the orientations of Titan's equatorial dunes reflect integrative winds over orbital timescales of tens of thousands of years.
29. Michaelides R. J. Hayes A. G.
Determining physical properties of Titan's empty lake basins through radar backscatter modeling.
We use repeat SAR observations to study the scattering properties of Titan's paleo-lake basins and infer their physical characteristics in an effort to understand their role in the evolution of Titan's polar surface morphology.
30. Montalvo P. E. Cavosie A. J. Valley J. W.
A Constraint on Shocked Mineral Abundance in the Jack Hills Zircon Suite
The Jack Hills zircon suite offers an opportunity to evaluate if detrital shocked zircons eroded from Hadean impact structure are preserved. Here we report the results of an SEM survey of 1400 Jack Hills zircons for shock microstructures.
31. Murl J. N. Gillis-Davis J. J.
Sulfur Composition Effects on Space Weathering
We investigated the effects of sulfur composition on simulated space weathering of powdered anorthosite. The results of this experiment show that the presence of sulfur in the Mercurian soil can contribute to 16% darker and 72% redder spectra.
32. Neely E. M. Spagnuolo M. G. de Silva S. L. Bridges N. T. Zimbelman J. R.
Methodology of Wind Tunnel Experiments Applied to Gravel Megaripple Formation on Earth and Mars
This abstract discusses the methodology used in analyzing wind tunnel experiments on clasts from megaripples in the Argentine Puna, which may be analogous to Transverse Aeolian Ridges on Mars.

33. Patmore E. B. Strait M. M. Flynn G. J. Durda D. D.
Compression Strength of Pumice
Compression strength of pumice was found to characterize porous materials used in catastrophic disruptions.
34. Sangha S. Diniega S.
Quantitative Investigations of Relationships between Tumuli Morphometrics and Lava Flow Emplacement
Aggregate tumuli orientations within lava fields are proposed as good records of general/local flow direction.
35. Schofield R. E. Hausrath E. M. Steiner M. H.
Dissolution of Nontronite in Brines: Implications for Habitable Environments on Mars
Interest in the habitability of Mars led us to conduct nontronite dissolution experiments in brines to describe the geochemical interactions between the clay mineral and 2 solutions. Results indicate the concentration of calcium increased over time.
36. Slezak T. Keszthelyi L. P. Okubo C. Williams D. A.
Paterae on Io: Compositional Constraints From Slope Stability Analysis
The near-vertical slopes of scarps on Io provide clues into the upper crust. We investigate compositional constraints using numerical slope stability modeling.
37. Stuurman C. M. Osinski G. R. Brothers T. C. Holt J. W. Kerrigan M.
SHARAD Reflectors in Utopia Planitia, Mars Consistent with Widespread, Thick Subsurface Ice
A reflecting interface has been discovered in SHARAD data over Utopia Planitia, Mars. Analysis is suggestive of a widespread (~400 000 square km) subsurface layer of ice ~100 m thick.
38. Trice K. J. Onyilagha J. C. Freeland S.
Biosynthesis of the Standard Amino Acids of the Genetic Code
The research examined the two assertions of The Co-evolution Theory as they relate to the biosynthesis of the 20 standard amino acids, in regard to new available data.
39. Vogler S. V.
Don't Get Burned! Protection from ICME related SEP Events in interplanetary space.
One of the most significant challenges regarding interplanetary travel is space radiation. The purpose of this research is to determine the relevance for a new method of ICME detection and radiation shielding on interplanetary spacecraft.
40. Watkins C. E. Hayne P. O. Bandfield J. L.
Ballistic Cascading as a Formation Mechanism for Lunar Cold Spot Craters: Constraints on the Impact Process from Diviner Thermal Measurements
Diviner identified a class of craters surrounded by cold regions. We developed a power law for the density profile of the area as a function of crater radii and tested models of creation.

41. Wernette B. W. Wright S. P. Farrand W. H.
XRD Patterns of Shocked and Altered Basalts as Analogs for MSL CheMin Data
A database of XRD patterns of basalts with ranges of both alteration state and shock level is being created to compare hydrovolcanic glasses and interpret XRD data from Mars.

42. Wiesman H. Floss C. Haenecour P. Wang A.
Search for Ultra-Carbonaceous Particles in the Interplanetary Dust Collection
We performed NanoSIMS and Raman analysis on a selection of particles classified as 'low-Z' contaminants from the cosmic dust collection in an attempt to characterize them as extraterrestrial low-Z IDPs, similar to ultra-carbonaceous micrometeorites.

43. Zaloumis J.
Microbial Biosignature Preservation in Crystal Geyser, Utah
The rapid mineralization of carbonates from Crystal Geyser, Utah are found to promote the capture and preservation of cellular and extracellular remains of microbial communities living within the spring environment.

DEVELOPING MAPPING-DERIVED STRAIN ESTIMATES FOR GIANT RADIAL LINEAMENT SYSTEMS ON VENUS. J.A. Albright¹, P.C. Ferrin¹, E.B. Grosfils¹, ¹Pomona College, Claremont, CA.

Introduction: Over 150 giant radial lineament systems characterized by extensional structures were first identified on Venus via a C1-MIDR resolution (225 m/pix) reconnaissance survey. On geomorphological grounds many of these radial systems (~3/4) appear to require shallow dike emplacement, with the remainder more plausibly related to domical uplift or a combination of the two mechanisms [1]. The presence of radial dikes has also been inferred from recent quantitative evaluations where fault offsets at large apical grabens permit direct hoop strain calculation [2,3]; however, most radial lineament systems are dominated by extensional structures only 1-2 pixels wide for which direct fault offset measurement is not possible. To address this limitation, here we use two such centers to propose a new mapping-derived technique that can be used to evaluate hoop strain at radially fractured systems, as well as two methods to account for discontinuous or obscured lineaments. Once tested and calibrated against existing models (see Grosfils et. al, Tuesday poster session), our technique has the potential to augment existing quantitative methods by incorporating narrow extensional structures that dominate the structural deformation at most giant radial lineament systems, providing important new insight into the origin of systems where efforts were previously restricted to geomorphological analysis alone.

Methods & Results: FMIDR resolution (75 m/pix) Magellan backscatter data imported into ArcGIS were used to map radial lineament systems centered upon Mbokomu Mons (15°S 215°E) (Fig. 1) and Thaukhud Linea (28.5°S 232°E) (not shown). To constrain the existing radial deformation we employ strain values ranging from 13-100%; since most of the mapped structures are ~1 pixel wide, this translates to a range of 10-75 meters of opening per lineament. A 75 m wide tension crack is the practical maximum limit for the dilatational strain/lineament, while the minimum value must generate sufficient surface deformation to create the relatively higher radar backscatter defining each lineament.

Calculating the hoop strain recorded by the lineaments at any given radial distance from the center of these features then simply requires multiplying an assumed strain/lineament by the number of lineaments that occur at that distance, then dividing by the original corresponding circumference ($2\pi r$). Depending on the assumed strain/lineament, the resulting strain profiles contain peak values ranging between 0.4% and 2.7% (Fig 2).

This technique, however, assumes that the mapped lineaments are the only ones that formed, even though in many cases, as seen in the highlighted region of Figure 1, existing lineaments can clearly be obscured by subsequent volcanism. To account for the hoop strain indicated by these obscured lineaments, we reevaluated the strain profile at Mbokomu Mons after subtracting the lengths of the arcs enclosed by the highlighted region from the circumference in the strain calculation. When compared to our original strain profile (Fig. 3), we see that this correction only raises the recorded strain of the outer annuli by less than 0.2% (absolute) when 50 m extension per lineament is assumed. Given the low total amounts of strain at these radial distances, however, the additional strain incorporated by this correction can account for up to 32% of the original values.

Additionally, if an otherwise continuous lineament is briefly discontinuous where a black annulus in Figure 1 crosses it, it would fail to be counted. To mitigate this mapping problem at Thaukhud Linea, we created small buffers (2% and 5% of radial distance) that thicken each annulus used to count lineament intersections. A new strain profile based on the number of lineaments that intersect these thicker rings is compared to the unadjusted profile in Figure 4. Unlike the correction used at Mbokomu Mons, this method increased strain at all radial distances by up to 42% of original values (0.4% absolute) with the 2% buffer and up to 130% (1.0% absolute) with the 5% buffer.

Discussion: While both of our proposed corrections raise the calculated hoop strain around radial lineament systems in order to negate the effect of uncounted lineaments, the amount of correction necessary remains unclear. The regions removed from strain calculations and the width of the annulus buffers are both subjectively defined; overly wide buffers or the elimination of regions that never contained lineaments could both lead to overestimation of the strain in each system.

Moreover, this technique of lineament mapping assumes the same amount of extension for each lineament, even though large grabens can indicate as much strain (~4% [2]) as entire systems of lineaments. The apices of these features also show relatively low strains when compared to the closest annuli. Further attempts at corrections, however, would only add to the uncertainty of the resulting strain profiles, as seen in the variability of the two methods already proposed.

In the absence of such corrections, however, mapping-derived strain estimates can provide a lower bound for the deformation recorded by radial lineament systems. Because of the underestimating effects listed above, this method produces the minimum strain profile required by each system. By comparing these values against predictions from different models of lineament formation, then, our method can provide a key line of evidence in determining the origins of these systems.

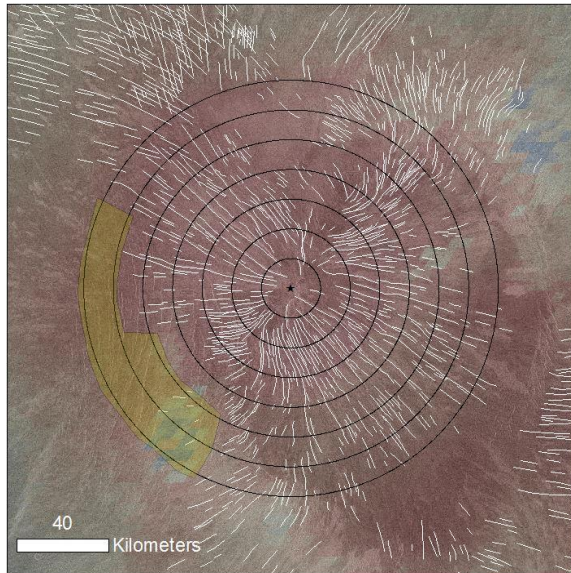


Figure 1. Mbokomu Mons, Venus, with color topography (red high, blue low) over Magellan backscatter data. Radial lineaments mapped in white; annuli used for strain calculations shown in black; obscured section experimentally omitted from calculations shown in orange.

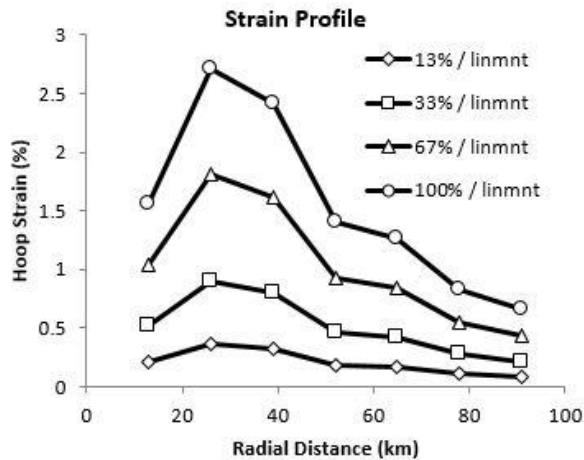


Figure 2. Map-derived hoop strain at Mbokomu Mons. Black lines depict strain assuming 13% (10 m), 33% (25 m), 67% (50 m) and 100% (75 m) strain per radial lineament intersecting a given annulus from Fig. 1.

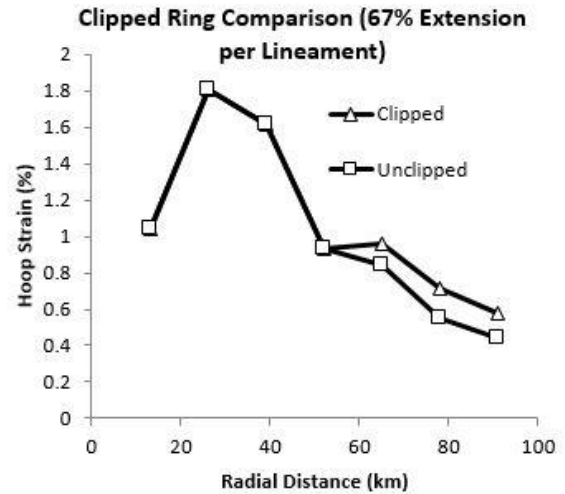


Figure 3. Comparison between calculated hoop strain at Mbokomu Mons including and omitting highlighted region in Fig. 1.

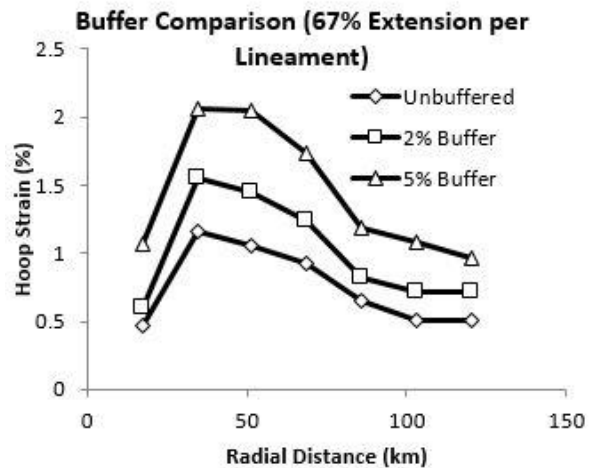


Figure 4. Strain profiles across Thaukhud Linea (not shown) with 2% and 5% buffers along either side of each annulus compared to unbuffered strain.

References: [1] Grosfils, E.B. and Head, J.W. (1994), *GRL*, 21, 701-704. [2] Grindrod, P.M. et al. (2005), *JGR*, 110, E12002, [3] McGovern, P.J. et al. (2014), *Geology*, 42, 59-62.

A STUDY OF SHOCKED QUARTZ IN BRECCIA FROM THE ROCK ELM IMPACT STRUCTURE.

A. Arana-Morales¹ and A. J. Cavosie^{1,2}

¹University of Puerto Rico-Mayagüez; ²University of Wisconsin-Madison

Introduction: Planar fractures resembling cleavage in quartz are a diagnostic indicator of shock metamorphism [1]. Occurrences of shocked-quartz bearing sandstone breccia have been reported at the Rock Elm impact structure in Wisconsin (USA). In this study we report an occurrence of suspected impact breccia from Rock Elm based on the documentation of quartz with planar fractures.

Rock Elm Impact Structure. The Rock Elm structure is recognized as an area of anomalous circular deformation over an area with a diameter of 6.5 km in west-central Wisconsin [2]. Characteristic shock-metamorphic features developed in quartz have provided evidence for the meteorite impact origin of the Rock Elm structure [3,4]. The age of the Rock Elm impact structure is approximately 470 Ma [2,3].

Planar fractures are a common microstructure that occurs in shocked quartz [1], and are believed to form at pressures <10 GPa. At Rock Elm, planar fractures are the most widely recognized indicator of shock metamorphism [3].

Samples/Methods: A sample of suspected impact breccia (sample 13RE07) was collected as ‘float’ from the central uplift of the Rock Elm structure in May 2013 (N 44° 43.025’ W 92° 13.820’). The breccia sample is orange to red in color, and has an overall oxidized appearance (Fig. 1). The sample contains sand to pebble-sized clasts and is poorly sorted; it does not resemble well-bedded outcrops of Mt. Simon sandstone in the vicinity. Rock slabs were cut and thin sections were prepared. Plane polarized and cross-polarized light microscopy were used to search for quartz grains with planar microstructures.

Results: The matrix has a reddish color and is generally opaque. The sample contains individual grains of quartz and plagioclase, and also lithic clasts. Quartz grains range from rounded to angular and vary in size. Lithic clasts contain mostly clay and quartz, and some have rare muscovite; all clasts appear to be sedimentary. A total of 42 shocked quartz grains were found in two thin sections. Shocked quartz grains range from 3 mm to 0.5 mm in size, and range from rounded to angular. Up to two orientations of planar fractures were found in some shocked quartz grains, and also feather features, a previously recognized shock microstructure at Rock Elm [3].

Grain 13RE07-39 is the largest and best example of shocked quartz identified (Fig. 2).

A focused study was made on grain 13RE07-39 to measure the spacing between planar fractures. Measurements of planar fracture spacing were made along three transects. The average planar fracture spacing is 105 μm , although the mode is at approximately 40 μm .



Figure 1: Cut rock slab from sample 13RE07 (unpolished). Note the heterogeneous orange-red color, and many voids. Horizontal dimension of image is approximately 20 cm.

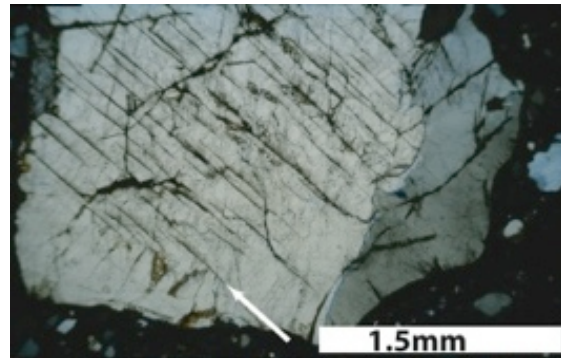


Figure 2: Quartz grain 13RE07-39. This large grain shows one dominant orientation of planar fractures (see arrow). Cross-polarized light.

Discussion: The presence of quartz with planar fractures in sample 13RE07 confirms an impact origin for this sample. We propose that this sample is a sedimentary breccia of impact origin based on the lack of sorting, lack of bedding, chaotic appearance, and highly altered state, which differs substantially from bedrock exposures of the Mt. Simon sandstone in the central uplift. Additional studies of this sample are ongoing.

References: [1] French, B. M. (1998) *LPI*. [2] Cordua W. S. (1985) *Geology*, 13, 372-374. [3] French B. M. et al. (2004) *GSA Bull.*, 116, 200-218 [4] Roig C. I. et al. (2013) *LPS Abstract #2685*.

EXPLORING THE MORPHOMETRY OF MARTIAN VALLEY NETWORKS AND DRAINAGE BASINS USING THE MARSSIM LANDFORM EVOLUTION MODEL. B. D. Boatwright¹ and C. I. Fassett²,
¹Department of Geology, Amherst College, Amherst, MA 01002 (bboatwright14@amherst.edu), ²Department of Astronomy, Mount Holyoke College, South Hadley, MA 01075 (cfassett@mtholyoke.edu).

Introduction: The existence of ancient valley networks and associated lakes and sediments on Mars suggests that fluvial activity once played a significant role in shaping the surface of the planet. This likely required a wetter and warmer climate than exists today [1-13].

Several studies [7, 14, 15] have demonstrated that the morphometric characteristics of drainage basins on Mars differ somewhat from those on Earth. For example, valleys commonly lack the well-graded, concave-up topographic profiles seen on Earth. In addition, the mean Hack's exponent appears to be higher for valley networks on Mars than on Earth. Hack's exponent h relates stream length L to drainage area A :

$$L = kA^h \quad (\text{eq. 1})$$

Typically, valley networks on Earth have $h \sim 0.5$ - 0.6 . On Mars, characteristic values for h are ~ 0.64 - 0.74 [14, 15]. In other words, valleys on Mars seem to possess smaller drainage areas for a given length than their terrestrial counterparts, implying that basins integrate (and widen) less quickly. This discrepancy has not yet been fully explained. Possible reasons may relate to the relative immaturity of the valleys and therefore a closer correlation between valley morphology and regional terrain [10, 12], the disruptive effects of impact cratering [16, 17], or a lack of tectonic uplift [14].

The MARSSIM landform evolution model was introduced by A. D. Howard in 1994 [18]. Its primary purpose is to simulate a variety of geomorphic processes on a digital elevation model (DEM) input file. These files may be created artificially or taken from real topographic data sets. The model can also simulate mass wasting, eolian processes, impact cratering, lava flows, accretion and ablation, and lake evaporation.

The effect of different geomorphic processes on input topography can be modeled in MARSSIM, and the interplay between processes can be examined in a controlled manner. In this way, a set of model runs can be compared with observations from real topography in order to determine which parameter or combination of parameters will create erosional features – specifically valley networks – most similar in morphometry to real drainage basins on Mars whose scaling properties are known. This allows us to quantitatively test hypotheses that might explain the observed discrepancies in valley properties on Mars and Earth. In principle, this can also provide insight into the specific geologic and cli-

matic conditions that prevailed at the time the valleys formed.

Methods: The MARSSIM landform evolution model is accessed through a command-line interface. A parameter file stores all possible inputs, although in most cases a limited number of simulation modes will be applied at any given time; for all experiments described here, the only processes enabled were fluvial erosion and mass wasting. A full explanation of the model parameters is given in [19].

We have used both idealized topographic datasets as well as real topography extracted from preexisting DEMs (MOLA and HRSC) using ArcMap, GDAL [20], and GMT [21] to crop regional terrain models. A command line tool has been created using TauDEM [22] to allow rapid derivation of Hack's exponents from MARSSIM output files. This allows for the determination of valley profiles and drainage areas without the need for manual post-processing.

Initial Numerical Experiments: The goal of our initial numerical experiments has been to understand the behavior of Hack's exponent in MARSSIM with different input parameters on idealized topography. We have run experiments on a domain that is periodic in X with a constant slope in Y , and a double-periodic domain, with a ridgeline separating two slopes in the center of the region (Fig. 1).

Gravity: The effect of the difference in gravitational acceleration between the two planets can easily be assessed in MARSSIM. We experimented by changing gravity, both with and without taking into account other expected differences in bed roughness [23] or channel width [24]. This cannot explain the observed difference in Hack's exponent between the two planets. Repeated simulations changing g on the synthetic ridges with 1 degree slopes (with simulated random noise of 10 cm magnitude) resulted in $h_{\text{average}} \sim 0.55$ on both Earth and Mars.

Discharge exponent: The parameter related to discharge in MARSSIM is the discharge exponent α , which relates to discharge Q and contributing area A as:

$$Q = kA^\alpha \quad (\text{eq. 2})$$

Therefore a higher discharge exponent will lead to greater runoff efficiency and more erosion, all else being equal [25]. This has a clear effect on the degree to which valleys incise the landscape (Fig. 1). The ef-

fect of changing α on Hack's exponent is less straightforward, however. Our initial results suggest that: (1) domains with higher α (more efficient runoff) appear to have less variability in h in different drainage basins across the model domain, and (2) the h_{average} appears to converge to typical terrestrial values (~ 0.55).

Future Numerical Experiments: Future numerical experiments will focus on using input files derived from the real Martian landscape. Source topographies will be based on those used in previous studies that have simulated Martian valley network formation with other landform evolution models [17, 25-28]. Regions of particular interest include Loire, Ma'adim, Naktong, Parana, Samara, and Warrego Valles, and valley networks surrounding large craters such as Dawes and Huygens. Existing valley features and young craters will be artificially removed using the median filter and blur tools in Photoshop as explained in [25, 27].

Another important question is whether Hack's exponent evolves with time, or if incision efficiency varies with valley maturity. Ultimately, the goal of this work is to develop a quantitative framework for understanding the differences in morphometry between Mars and Earth. Many factors may be relevant to this problem, including the discharge exponent, timescale and periodicity of formation, grain size and bed roughness, and the role of cratering.

References: [1] Masursky H. et al. (1977) *JGR*, 82, 4016-4038. [2] Kasting J. F. (1991) *Icarus*, 94, 1-13. [3]

Squyres S. W. and Kasting J. F. (1994) *Science*, 265, 744-749. [4] Malin M. C. and Carr M. H. (1999) *Nature*, 397, 589-591. [5] Williams R. M. E. and Phillips R. J. (2001) *JGR*, 106, 23737-23751. [6] Craddock R. A. and Howard A. D. (2002) *JGR*, 107, 5111. [7] Stepinski T. F. and Stepinski A. P. (2005) *JGR*, 110, E12S12. [8] Ansan V. et al. (2008) *JGR*, 113, E07006. [9] Fassett C. I. and Head J. W. (2008a) *Icarus*, 195, 61-89. [10] Carr M. H. and Head J. W. (2010) *Earth & Pl. Sci. Letters*, 294, 185-203. [11] Fassett C. I. and Head J. W. (2011) *Icarus*, 211, 1204-1214. [12] Irwin R. P. et al. (2011) *JGR*, 116, E02005. [13] Craddock R. A. et al. (2013) *LPSC XLIV*, Abstract #1984. [14] Penido J. C. et al. (2013) *Pl. & Space Sci.*, 75, 105-116. [15] Ansan V. and Mangold N. (2013) *JGR*, 118, 1873-1894. [16] Irwin R. P. et al. (2002) *LPSC XXXIII*, Abstract #1729. [17] Howard A. D. (2007) *Geomorphology*, 91, 332-363. [18] Howard A. D. (1994) *Water Resources Res.*, 30, 2261-2285. [19] Howard A. D. (2009) MARSSIM release 3.0 program files, <http://erode.evsc.virginia.edu>. [20] Geospatial Data Abstraction Library, <http://www.gdal.org>. [21] The Generic Mapping Tools, <http://gmt.soest.hawaii.edu>. [22] Tarboton D. Terrain Analysis Using Digital Elevation Models, <http://hydrology.usu.edu/taudem/taudem5/index.html>. [23] Wilson L. et al. (2004) *JGR*, 109, E09003. [24] Som S. M. et al. (2009) *JGR*, 114, E02005. [25] Barnhart C. J. et al. (2009) *JGR*, 114, E01003. [26] Forsberg-Taylor N. K. et al. (2004) *JGR*, 109, E05002. [27] Matsubara Y. et al. (2011) *JGR*, 116, E04001. [28] Matsubara Y. et al. (2013) *JGR*, 118, 1365-1387.

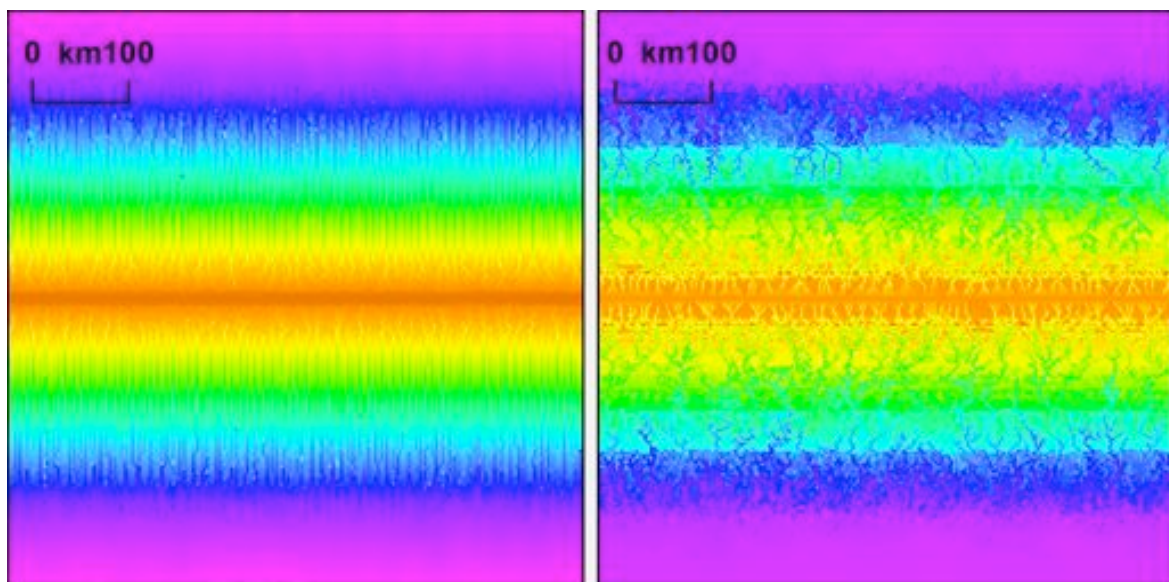


Figure 1. Output elevation on idealized “ridge” topography (0.5° initial slope), with $\alpha = 0.75$ (left) versus $\alpha = 0.9$ (right) (both run to 50 Kyr). The average Hack's exponent of the three longest drainages in the lower precipitation case ($\alpha = 0.75$) is 0.74, and in the higher precipitation case ($\alpha = 0.9$) is 0.68 ; the difference is likely due to the capture of some of the smaller drainages by the longest valleys as incision progressed in the “wetter” case.

How Can Wet Apatite be Found on a Dry Moon?

J.W. BOYCE¹ AND S.M. TOMLINSON¹

¹Department of Earth, Planetary, and Space Sciences, UCLA Box 951567, Los Angeles, CA 90095-1567.

The leading canonical giant impact models of moon formation have been supported by decades of volatile depleted lunar rock samples-but recent discoveries of terrestrial level water rich lunar apatite casts uncertainty and creates what has come to be known as: The Lunar Apatite Paradox-How can one H rich mineral be found in a rock that is otherwise depleted of volatile elements. Here we explain the paradox by showing how the H rich apatite found is a product of apatite-induced low magmatic fluorine. This model adds trace amounts of apatite of variable composition late into the fractionating assemblage forming hydrous apatite with in the volatile depleted host rocks - in support of both the lunar rock data and the various giant impact hypotheses.

GRAIN SIZE, 'SPOTTY' XRD RINGS, AND CHEMIN: TWO-DIMENSIONAL X-RAY DIFFRACTION AS A PROXY FOR GRAIN SIZE MEASUREMENT IN PLANETARY MATERIALS. M. S. Bramble¹, R. L. Flemming², P. J. A. McCausland², ¹Dept. of Physics and Astronomy, and the ²Dept. of Earth Sciences, The University of Western Ontario, London, ON, N6A 5B7, Canada (michaelbramble@gmail.com).

Grain Size from 2D XRD: Two-dimensional (2D) X-ray diffraction (XRD) data can provide textural information about the mineral assemblage of a sample in addition to mineral identification by structure [1-4]. In film and for more modern 2D XRD detectors, diffracted X-rays are recorded as Debye rings, with the radius of the ring representing the 2-theta angle of a particular diffraction condition for an irradiated crystal structure. Debye rings contain textural information about the sample, such as its degree of crystallinity and potentially structural distortion effects such as the degree of strain experienced by individual mineral grains [1,4]. In particular, a 'spotty' ring can be inversely correlated with the grain size of a material (e.g. [1,2]); with increasing grain size a progression is observed from classically smooth Debye diffraction rings (for <5 μm powders), to rings with many discrete spots, to fewer spots, and finally to diffraction spots representing a single crystal (Fig. 1). The observed 'spottiness' of the diffraction rings thus allows for inferences to be made about the mean grain size of the sample between $\sim \mu\text{m}$ crystals up to about the size of the incident X-ray beam. Here, we perform an experimental study of 2D XRD grain size estimation on mineral powders with known sieve fraction grain sizes, and then apply this empirical method to the interpretation of 2D XRD data from the Mars Science Laboratory.

Theory and Method: We have used the method of He [3] to estimate grain size by relating an integrated window on a 2D XRD detector to the volume of an irradiated material. The number of grains contributing to a particular diffraction ring is measured by integrating in the χ direction and then fitting a polynomial or average intensity trendline. Half the number of times this χ -profile crosses a trendline represents the number of irradiated grains contributing to the ring. The grain size is then measured by ratioing the beam divergence, multiplicity, and instrument angular window to the number of grains in the profile and cube-rooting the result. The X-ray source beam diameter and linear absorption coefficient for the target mineral are also taken into account, along with changed constants, for reflection-mode as opposed to transmission-mode XRD.

Application to well-characterized pyroxene: Using the Bruker D8 Discover micro-X-ray diffractometer (μXRD) at the University of Western Ontario [4], the grain size measurement method [3] was applied to a set of well-characterized ferroan enstatite pyroxene samples [5]. The μXRD operated with θ - θ geometry,

stationary optics, and no sample motion using a $\text{CoK}\alpha$ source ($\lambda = 1.7902 \text{ \AA}$) at 35 kV and 45 mA to produce incident X-rays in a 300 μm diameter beam. 2D data were collected on a HI-STAR area detector located 12 cm away from the sample and analyzed using General Area Detector Diffraction System (GADDS) software.

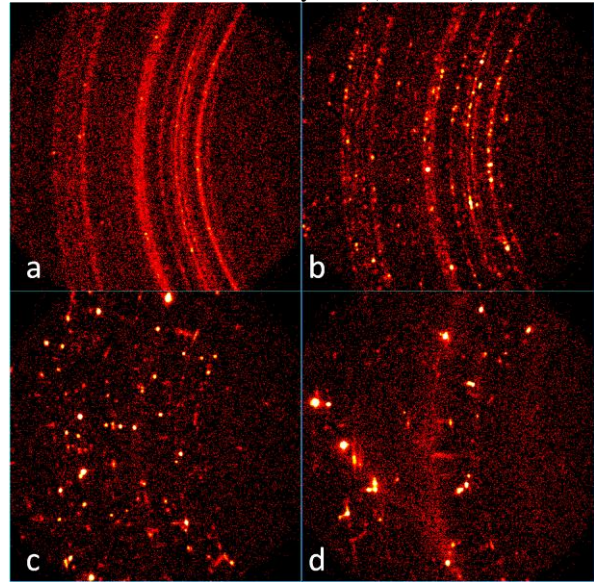


Figure 1. 2D XRD images of pyroxene samples of increasing grain size; (a) relatively continuous rings of a sample ground to <5 μm with a mortar and pestle; (b), (c), and (d), show the progression of 'spotty', closely spaced rings to more discontinuous rings as the grain size increases in sieve size from 10–15, 25–38, to 90–125 μm , respectively. The very fine grained polycrystalline material visible in (d) is mineral dust, as the specimen was not washed after crushing.

The calculated grain sizes by χ -profile analysis of diffraction rings (Fig. 2a-b) correlate well with the sieve size bins of the pyroxene samples. The measured grain sizes either fell within the sieve size bins, or just outside the bin by $\pm \sim 5 \mu\text{m}$. Discrepancies may result from equation parameters (such as using a given beam divergence [3]), or from the pyroxene physical properties and their effects on sieving. An independent assessment of the sieved samples by electron microscopy will help to quantify their mean grain size, allowing for firmer conclusions about the 2D XRD method. For grain sizes >100 μm the effectiveness of the method breaks down [3]. With the geometry used in this study, the close detector distance causes the equation to begin to significantly underestimate grain size ($\geq 14 \mu\text{m}$) as the sieve sizes increase above $\sim 50 \mu\text{m}$. This is likely the result of fewer diffraction spots reaching the detector area for a given Debye ring.

Effect of oscillation / granular convection: This method of grain size measurement relates the detector image with the irradiated sample volume, and therefore it is necessary for the sample to remain stationary during data collection. Samples analyzed by CheMin are vibrated [6] to increase the number of grains achieving diffraction condition, so the application of the above method may subsequently underestimate grain size. We therefore collected some oscillated sample data for three of the sieved pyroxene bins (ranging from 10 to 38 μm) with an oscillation in Y of 3.5 mm, to investigate the effects of sample motion on the diffraction rings. The 'spotty' rings became more uniform. The calculated grain size fell into the correct sieve bin for one sample and the other two samples underestimated the grain size by $\sim 5 \mu\text{m}$, suggesting that a similar calculation applied to CheMin data would similarly underestimate grain size.

Calculated MSL Rocknest grain size: The grain size measurement calculation was applied to CheMin 2D XRD images collected from the fifth scooped sample at the Rocknest site at Gale Crater [7]. The 2D XRD images were analyzed with a ten-step integration per degree χ . The transmission-mode calculation is independent of sample chemistry, but for multi-phase materials a volume fraction of the analyzed material must be known. We used the refined modal mineralogy from [7]. Transmission-mode does not require assumptions about the effective sampling volume and therefore should generate a more direct grain size calculation.

The first image analyzed was one generated from the 55 images uploaded from sol 94 to sol 119. The χ -profile analysis (Fig. 2c-d) calculated grain sizes for plagioclase, enstatite, and forsterite with resultant values of 4.8, 6.7, and 5.1 μm , respectively. With the above arguments, these values are likely underestimates of the actual mean grain size. *Curiosity's* hardware provides an upper grain size limit of 150 μm and these XRD calculations provide the lower limit.

According to the PDS labels for CheMin data products, it appears that a brief, yet unsuccessful, experiment was conducted in the aim of collecting a pattern without grain motion. The resultant 2D image displayed no diffraction spots, but the image (generated from frames uploaded on sol 148) was analyzed using the χ -profile method. If the degree of granular convection was reduced, there should be fewer diffraction spots contributing to the Debye ring and the grain size should be less underestimated and closer to the actual value. The calculation resulted in an increase of $<1 \mu\text{m}$ for the plagioclase and forsterite and a decrease in $<1 \mu\text{m}$ for the enstatite. The absence of a significant increase in calculated grain size suggests that granular

convection still occurred, but it should also be noted that due to the collection time and data resolution this calculation was possibly compromised by signal to noise factors.

If future 2D XRD data are successfully collected from *Curiosity* without any granular convection, then a more confident grain size calculation can be made. XRD is essential for mineral identification, and if future planetary spacecraft are equipped with an *in situ* μXRD as proposed in [8], precise grain size measurements could be calculated on a regular basis. This method, when paired with a stationary sample, should provide a quantitative, non-optical method for grain size measurement by planetary spacecraft.

Acknowledgments: We thank M.A. Craig and E.A. Cloutis for providing the pyroxene size fraction samples used in this study, and B.B. He for further discussions regarding the 2D XRD theory. CheMin data were obtained from the PDS. Funding to RLF and PJAM for this project is from the Natural Sciences and Engineering Research Council of Canada (NSERC).

References: [1] Hörz F. & Quaide W.L. (1973) *The Moon*, 6, 45–82. [2] Klug H.P. & Alexander L.E. (1974) Wiley (ISBN 0471493694). [3] He, B.B. (2009) Wiley (ISBN 9780470227220). [4] Flemming R.L. (2007) *Can. J. Earth Sci.*, 44, 1333–1346. [5] Craig, M.A. et al. (2008) LPS XXXIX, Abstract #2082. [6] Blake, D. et al. (2012) *Space Sci. Rev.* 170, 1–4, 341–399. [7] Bish D.L. et al. (2013) *Science*, 341, (6153), 1238932. [8] Flemming R.L. et al. (2009) LPS XXXX, Abstract #1888.

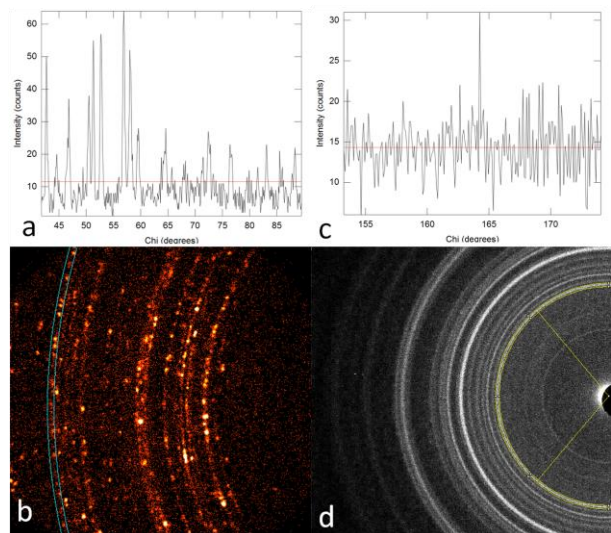


Figure 2. Pyroxene χ -profile (a), and corresponding 2D image showing the window of integration (in blue) (b). Pyroxene sieve size: 10–15 μm , wet sieved [5]. CheMin 2D XRD image generated from frames uploaded from sol 94 to sol 119. A χ -profile (c) segment is depicted along with the 2D image window of integration (d).

MODIFICATION-STAGE TECTONICS PRIOR TO MELT SHEET EMPLACEMENT: CONSTRAINTS FROM THE MANICOUAGAN IMPACT STRUCTURE. Jessie J. Brown, Lucy M. Thompson and John G. Spray, Planetary and Space Science Centre, University of New Brunswick, 2 Bailey Drive, Fredericton, New Brunswick E3B 5A3, Canada <jessie.brown@unb.ca>

Introduction: The Manicouagan impact structure, formed at 214 Ma, comprises a target dominated by Precambrian metamorphic rocks, including various gneisses and anorthosite assembled during the 1 Ga Grenville orogeny [1]. In addition, a veneer (<200 m thick) of Middle Ordovician carbonates and shales was present at the time of impact [2]. This sedimentary rock cover provides a valuable marker horizon with which to calibrate transient cavity evolution during the excavation- to modification-stage transition of the impact process. The cover sequence was regionally eroded and largely erased from the Canadian Shield following impact, leaving only down-dropped units preserved within the impact structure itself. The limestone-shale assembly now occurs as blocks (with multi-metre dimensions), and as smaller fragments (cm- to m-size) in three settings: (1) the main body of impact melt, especially at its base and periphery; (2) in basal suevites, which are located between melt sheet and underlying footwall, and (3) within the footwall assemblage as deep as at least 300 m beneath the melt sheet. The latter association is revealed through field studies and the logging of drill core. These deep occurrences of sedimentary rocks are of particular interest because they must have been transported to their buried positions prior to emplacement of the overlying impact melt sheet, which most probably took place within minutes of melt formation. Rapid tectonics are required to achieve this. We propose that the mechanism to achieve burial involves widening and shallowing processes associated with progressive rim failure and crater collapse.

Field context: Field operations around the west flank of the Manicouagan structure based at the edge of the main island (at a radial distance of approximately 27 km from the crater's centre) reveal a footwall section dominated by gneisses underlying impact melt. The gneisses are typically fractured. They are not incoherent, but rather shattered like 3D puzzle pieces. Faulting is also evident, most of which is high-angle, with sub-metre displacement. More massive gneiss zones also occur. Intercalated with the Precambrian gneisses are Ordovician limestone blocks. The presence of the limestone in the field area is clear evidence that the rocks observed must have been emplaced by the collapse of the rim of the transient crater, and cannot represent rocks of the original basement.

In most cases the contact between the gneiss and limestone units is defined by an intervening breccia comprising gneiss and limestone fragments combined, occasionally with an associated friction melt (pseudotachylyte). It is not clear whether the limestone is still related to its original underlying gneiss, or whether gneiss and limestone decoupled during collapse. Both may be possible. Either way, there appears to be some coherence to the sedimentary rock-gneiss relationship: the footwall is not a jumble of random blocks.

Drill core constraints: Multiple mineral exploration drill holes produced in the 1990s and 2000s generated ~18 km of core, 10 km of which is currently held by the Planetary and Space Science Centre at UNB. In the western section of the island, logs of core that complement field mapping, namely holes 0504, 0505, 0507 and 0607, reveal that limestone is interleaved with gneiss to depths of at least 300 m below the melt sheet. Apparent limestone thicknesses in these drill holes range from 18 to 128 m.

Borehole logs also provide more information on the nature of the sedimentary rock-gneiss relationship. In boreholes 0507 and 0607 limestone occurs twice, with gneiss between the two occurrences. The majority of contacts observed between gneiss and limestone are brecciated. This observed association is best explained by assuming the geology represents large, coherent blocks, which originated in the transient crater rim and reached their current location by falling, or sliding, from the oversteepened edge. With this model, it is possible to estimate a linear dimension for these coherent blocks by measuring the distance between the tops of the limestone occurrences in the holes in which they are repeated. From this simple estimation, we suggest that blocks falling from the rim may have been between 50 and 200 m in linear section.

Discussion: The interleaving of limestone with gneiss to depths of at least 300 m below the impact melt sheet indicates that the original surface sequence of limestone-on-gneiss has been (1) tectonically repeated via imbrication or folding of the surface stratigraphy as it collapsed into the widening transient cavity; (2) limestone became decoupled from its immediate footwall gneiss and was more randomly incorporated during collapse, or (3) the cavity margins behaved incoherently and collapsed randomly into the growing crater. The nature of the limestone-gneiss relations

does not support a rubble association, but rather an interleaving of more coherent, larger blocks, with movement between lithologies being accommodated by frictional melting, comminution and/or brecciation. However, our interpretation of these processes may be scale dependent, with our view being compromised by outcrop restrictions and the limited lateral information provided by drill core.

It is well established that the modification stage continues after impact melt emplacement [3], e.g., with crater-margin slumping into the melt sheet and associated terrace formation. This work shows that considerable cavity collapse can initiate very early in the cratering process prior to melt sheet emplacement. This must occur during the late excavation to initial modification stages. Moreover, the rocks in the oversteepened rim must begin to move almost immediately in order to attain the very high speeds necessary to emplace surface rocks at significant depths beneath the melt sheet before the highly-mobile, superheated liquid comes to rest.

References: [1] Spray, J. G. et al. (2010) *Planet. Space Sci.* 58, 538-551. [2] Nowlan, G.S. and Barnes, C. R. (1987) *Bull. Geol. Surv. Can.* 367, 47 p. [3] French, B. M. (1998) *Traces of Catastrophe*, LPI Contrib. 954, 120 p.

Focal Plane Actuation to Achieve Ultra-High Resolution on Suborbital Balloon Payloads

The purpose of this project is to develop a focal plane actuation system for balloon-borne telescopes in order to deliver diffraction limited imaging. Balloon-borne observatories provide a wide range of scientific purposes and can achieve resolution comparable to the Hubble Space Telescope for a fraction of the cost. The resolution of these balloon telescopes is limited by the presence of a low amplitude, high frequency jitter caused by thermal variations as well as the operation of instruments in the payload itself. The project aims to use an off the shelf hexapod device to actuate the focal plane and reduce the jitter induced movement to within $6.5\mu\text{m}$, containing motions within a single pixel on the CCD and reducing the pointing error of the telescope to within 0.1 arcseconds.

The CCD must be maintained at cryogenic temperatures in order to ensure proper functionality while the hexapod relies on piezoelectric devices that must be kept at room temperature to provide accurate movement. In order to have the hexapod and the CCD work in harmony, they must be thermally isolated from each other. Conductive heat transfer is eliminated using a layer of G10 fiberglass between the CCD and the hexapod. Convective heat transfer is eliminated by placing the entire system inside a dewar and introducing a vacuum environment (Fig. 1). Radiation shielding between the devices prevents heat transfer through radiation. An existing jitter signal from a past balloon mission is being used to drive a motorized target at the actual amplitude and

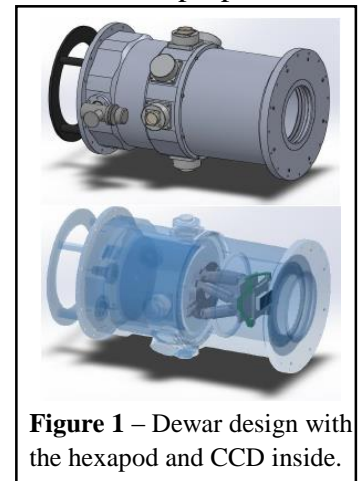


Figure 1 – Dewar design with the hexapod and CCD inside.

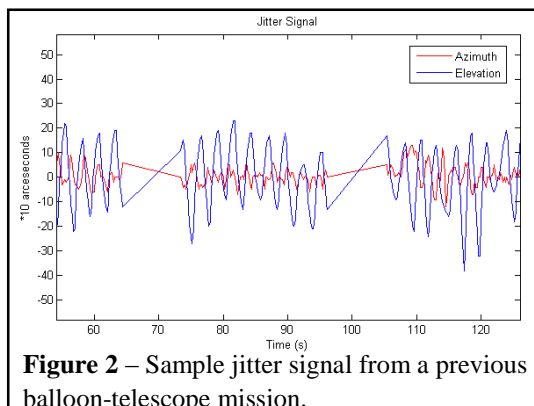


Figure 2 – Sample jitter signal from a previous balloon-telescope mission.

frequency that can be expected on a real mission (Fig. 2). To verify that the hexapod system works, the mounted CCD must be able to provide a clear image of the target. This system has many applications for planetary science. Not only are balloon missions far more cost effective than space-based observatories, but they are also able to offer long term observation windows that are impossible

to obtain on current space-based platforms. Balloon payloads are also often reusable, further reducing costs and allowing for more rapid deployment of successive missions. In addition to

providing diffraction limited imaging from balloon-borne telescopes, this system can be used as a portable focal plane actuation device and taken to a variety of ground-based observatories.

DISRUPTION EXPERIMENTS WITH AN ARTIFICIALLY HYDRATED ORDINARY CHONDRITE.

A.N. Clayton¹, M. M. Strait¹, G. J. Flynn², and D. D. Durda³ ¹Dept. Of Chemistry, Alma College, 614 W. Superior St., Alma MI 48801 (clayton1an@alma.edu), ²Dept. Of Physics, State University of New York-Plattsburgh, Plattsburgh NY 12901, ³Southwest Research Institute, 1050 Walnut Street Suite 3400, Boulder CO 80302

Introduction: Meteorites are valuable for use in determining rudimentary differences among extraterrestrial materials. Of particular interest is the difference in disruption patterns between ordinary and carbonaceous chondrites, as this may shed light on the creation of the smaller particles observed in the Solar System [1]. Hydrous meteorites are primarily present as carbonaceous chondrites. The availability of carbonaceous chondrites for disruption experiments is highly limited as they account for only 5% of chondritic falls [2].

Prior experiments have examined disruption pattern differences in terrestrial and extraterrestrial samples. The disruption of these meteorites took place at the NASA Ames Vertical Gun Range in Moffett Field, California. Foil detectors were set up inside the vacuum chamber. Penetrations in these foil detectors were measured and used along with the debris to create mass-frequency distribution diagrams. [3]. Particles in the cosmic dust as well as micrometeorite range were produced in the disruptions. The mass-frequency distributions of terrestrial and extraterrestrial samples have been shown to be significantly different [4]. However, these studies focused primarily on ordinary chondrites, and the carbonaceous chondrites studied were anhydrous [5]. Hydrous carbonaceous chondrites that have been disrupted produced dissimilar results when compared with anhydrous samples. It is necessary to disrupt additional hydrated chondrites in order to further understanding of the differences in mass-frequency distributions between hydrous and anhydrous chondrites. However, the valuable nature of the samples has led to investigation of a method of hydrating ordinary chondrites that may be used as analogues.

A method was developed to create analogues for carbonaceous chondrites using samples of NWA 869, a readily available ordinary chondrite. Samples of approximately 15 g were placed inside a pressure bomb in a solution of pH ~13 and kept in an oven at 150°C for up to two years. The samples were then cut in half to be evaluated with FTIR [6]. Preliminary scans of these hydrated samples found evidence of hydration in all samples [7].

Experimental: An alternate method was developed to create a hydrous meteorite using smaller samples of NWA 869 that may be bound together to create a carbonaceous chondrite. Fragments of NWA 869 were crushed to ensure that no particles were larger than 2 mm with the exception of sample 130708. The fragments were placed in a pressure bomb in a solution

of pH ~13 and placed in an oven at 150°C for up to four months. At various points during the hydration, random fragments were removed from the bomb, rinsed with deionized water, and crushed to form a powder. This powder was scanned with a Bruker ALPHA FTIR instrument to look for a peak at 3500 cm⁻¹, indicating the presence of hydration. Once hydration was complete, the fragments were removed from the bomb, rinsed with deionized water, and placed into a metal pipe lined with plastic wrap. A metal insert was placed on top of the sample inside the pipe. The apparatus was positioned under a hydraulic press and compressed to approximately 5 tons. The sample was left at this pressure for at least 7 days. The apparatus was then removed from the hydraulic press. The samples were fragile around the edges and crumbled easily but appeared solid in the center. Two samples were chosen and suspended in the vacuum chamber at the Ames Vertical Gun Range in California. Both samples were disrupted with 1/8 inch aluminum projectiles at a speed of ~5 km/sec. As with previous experiments [3], foil detectors were set up inside the vacuum chamber and penetrations in these detectors were measured using ImageJ and the data used to create mass-frequency distribution graphs.

Results: The mass-frequency distributions of samples 130707 and 130708 had similar size ranges, and a similar mass for the largest particle. Sample 130708 showed an S-shaped curve typical of a NWA 869 mass-frequency distribution (Figure 1), while sample 130707 was missing a distinct central plateau (Figure 2). This may have been caused by a difference in projectile speed for the samples. Although the target speed for each disruption was 5 km/sec, sample 130707 was disrupted at 5.54 km/sec, while sample 130708 was disrupted at 4.13 km/sec. The samples also had different weights. Sample 130707 weighed 28.41 g, while sample 130708 only had 18.43 g. An additional factor that may have caused this dissimilarity is the extent of the hydration in the sample. Sample 130708 was left in the oven for a longer period than sample 130707. However, sample 130707 had smaller particles that may not have required as much time for hydration.

Sample 130707 shows some similarities to the mass-frequency distribution of Murchison, a carbonaceous chondrite [9]. The distributions have similar size ranges. Murchison is also missing the central plateau characteristic of ordinary chondrites.

The samples created were flat disks approximately 10 mm thick and about 40 mm in diameter. This prob-

ably caused some of the discrepancies observed between these artificially hydrated samples and an actual rock. In order to better replicate a natural hydrous meteorite, future work will consist of creating samples with similar dimensions for length, height, and width. The composition of the material created will also be characterized.

Acknowledgements: I would like to acknowledge Sarah Jack for her assistance in preparing and scanning slides while I was abroad. This work was supported by NASA Planetary Geology and Geophysics Program Project Number NNX11AP22G. Support was also provided by the National Science Foundation via the PRISM grant to Alma College and the Alma College Chemistry Department.

References: [1] Flynn G. J. et al. (1997) *Planetary and Space Science*, 57, 119-126. [2] Minnick, M. A. et al. (2009) *Lunar and Planet. Sci. Conf. XXXX* #2224. [3] Lipman M. D. et al. (2010) *Lunar and Planet. Sci. Conf. XXXXI* # 2442. [4] Durda D. D. et al. (1997) *Workshop on Dust in Planetary Systems*, 77-80. [5] Lipman M. D. et al. (2011) *Lunar and Planet. Sci. Conf. XXXXII* #1303. [6] Clayton, A. N. et al. (2012) *Lunar and Planet. Sci. Conf. XXXXIII* #2764. [7] Strait, M. M. et al. (2012) *Met. And Planet. Sci.* 47, #5363. [8] Clayton, A. N. et al. (2012) *Lunar and Planet. Sci. Conf. XXXXIV* #2730. [9] Flynn, G.J. et al. (2009) *Planetary and Space Science.*, 57, 119-126.

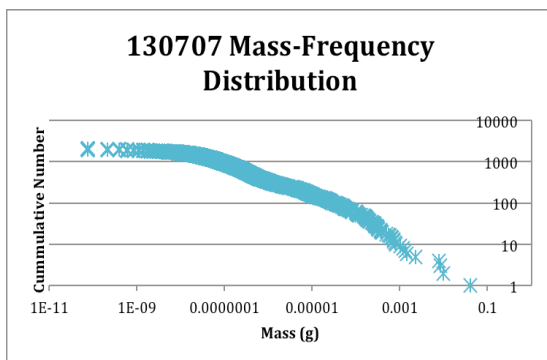


Figure 1. Mass-frequency distribution diagram for hydrated NWA 869. The crushed particles were hydrated for approximately 30 days and compressed for 7 days.

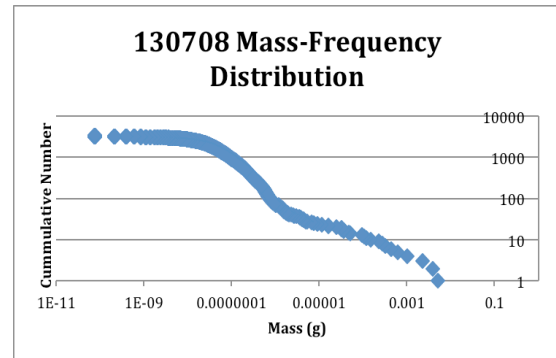


Figure 2. Mass-frequency distribution diagram for hydrated NWA 869. The crushed particles were hydrated for approximately 100 days and compressed for 7 days.

DETRITAL SHOCKED MUSCOVITE FROM THE SANTA FE IMPACT STRUCTURE (USA).D. Colón Lugo¹ and A. J. Cavosie^{1,2}Univ. Puerto Rico-Mayagüez (denyse.colon@upr.edu), ²Univ. of Wisconsin-Madison

Introduction: Micas with kink bands (KB) remain a relatively understudied shocked mineral due to the formation of KB in both high strain (impact) and low strain (tectonic) regimes [1]. The discovery of shatter cones and shocked quartz near Santa Fe, New Mexico, led to the discovery and confirmation of the Santa Fe impact structure [2]. In addition to quartz, KB in muscovite were mentioned but not well-documented in the original discovery report. Here we report the occurrence of muscovite with KB (hereafter ‘shocked muscovite’) in modern colluvium collected near shatter cone outcrops. We report the results of a transmitted light and scanning electron microscopy (SEM) study of the kink bands, as well as electron microprobe analyses (EMPA) of the composition of the shocked muscovite grains in order to better document the shocked muscovite grains and to provide a basis for comparisons with other occurrences of shocked muscovite.

Shock metamorphism: Kink bands in mica result from glide and rotation mechanisms, and have been reported in mica as a product of regional metamorphism, meteoric impact, nuclear explosion, and laboratory experiment [3]. For our purposes, a kink band is defined as a microscale lense-like zone in which a pair of sub-parallel to parallel planes with opposite dislocations delimit the edges of a crystal domain deformed by gliding planes [4,5]. In muscovite, KB are readily visible features due to the deflection of cleavage orientation within the KB.

Samples: Sample 11NM03 is mixed colluvium/alluvium in a north-south drainage ~50m north of Hwy 475 [6]. A second colluvium sample, 11NM05, is from a shatter cone outcrop approximately 1 km further east on Hwy 475. Two thin sections were made from each sample and were analyzed using transmitted light (TL) imaging. SEM images of shock microstructures and muscovite EMPA data were collected for the same grains in thin section from both samples.

TL and SEM result: KB microstructures cross the c-axis in multiple orientations, and up to 3 orientations were observed in single grains. KB were divided into categories based on geometry of the microstructure: planar KB (Fig. 1), curvilinear KB, and serrate (saw-tooth) KB. In addition, kink band size and length are variable; we observe grain-scale KB, micro KB (~10 μm long, sometimes in arrays), thin KB (<5 μm thick), and wide KB (>5 μm thick) variations.

EMPA results: Muscovite compositions in each sample are similar: 11NM03-94 yielded a formula of: $(K_{2.066}, Na_{0.086}) (Al_{4.426}, Fe_{0.564}, Mg_{0.200}, Ti_{0.133}) (Al_{1.497} Si_{6.503} O_{20}) (OH)_4$ and 11NM05-52 yielded a formula of $(K_{2.026}, Na_{0.090}) (Al_{4.404}, Fe_{0.589}, Mg_{0.232}, Ti_{0.112}) (Al_{1.439} Si_{6.561} O_{20}) (OH)_4$. The presence of Na, Fe, and Mg indicates minor celadonite and paragonite solid solution. In general, the muscovite compositions are not anomalous.

Discussion: Shock microstructures in Santa Fe micas bear similarities and differences with other occurrences. In general, a wider range of variations was observed in our study than previously reported. Further detailed investigation of KB microstructural variability may lead to identification of features that can be used to identify a high strain (impact) vs. low strain (tectonic) origin.

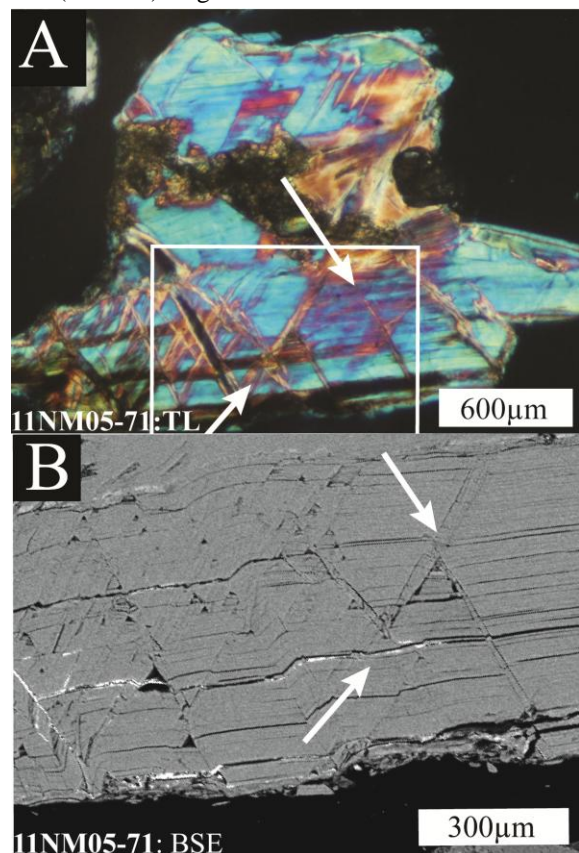


Figure 1. A) Transmitted light and B) BSE image of muscovite grain 11NM05-71 with two orientations of kind bands (arrows). Cleavage is roughly horizontal.

References: [1] French B. M. (1998) *LPI*. [2] Fackelman, S. P. et al. (2008) *EPSL*, 270, 290-299. [3] Hörtz (1970) *JGR*. [4] Misra S. and Burg J. (2012) *Tectonophys.* [5] Starkey J. (1968) *Contr. Mineral. Petrol.* [6] Lugo et al. (2012) *LPSC*, Abstract #2014.

THE GALE CRATER MOUND IN A REGIONAL GEOLOGIC SETTING: COMPARISON STUDY OF WIND EROSION IN GALE CRATER AND WITHIN A 1000 KM RADIUS. A. Dapremont¹, C. Allen², and C. Runyon¹, ¹Department of Geology and Environmental Geosciences, College of Charleston, Charleston, SC 29424 (amdapremont@gmail.com) (runyonc@cofc.edu) , ² Astromaterials Research and Exploration Science, NASA Johnson Space Center, Houston, TX 77058 (carlton.c.allen@nasa.gov).

Introduction: Gale is a Late Noachian/Early Hesperian impact crater located on the dichotomy boundary separating the southern highlands and the northern lowlands of Mars [1,2]. NASA's Curiosity Rover is currently exploring Gale, searching for evidence of habitability early in Mars history. With an approximate diameter of 155 km, and a ~ 5 km central mound informally titled Mt. Sharp, Gale represents a region of geologic interest due to the abundance of knowledge that can be derived, through its sedimentary deposits, pertaining to the environmental evolution of Mars [2][Fig. 1]. This study was undertaken to compare wind erosional features in Gale Crater and within sediments in a 1000 km radial area. The ultimate objective of this comparison was to determine if or how Gale relates to the surrounding region.

Large scale aeolian erosional features called yardangs are a proxy for prevailing wind direction over an extended period of time. Thomson et al. [1] mapped several yardang units in the Lower Mound (LM) and Upper Mound (UM) of Gale, and similar features have been noted in studies of the Medusae Fossae Formation (MFF) near the dichotomy boundary [3, 4]. The MFF is comprised of three members: upper, middle, and lower [5]. Only the latter two members are located within 1000 km of Gale [Fig. 2]. The MFF is thought to be Hesperian-Amazonian in age and formed from volcanic ash [4,6]. It contains the largest concentration of yardangs on Mars [7]. Yardangs are valuable tools for correlation studies of Gale and the surrounding regional geology.

Methodologies: Wind directions of yardangs inside and outside of Gale were mapped using the Mars Reconnaissance Orbiter (MRO) Context Camera (CTX) mosaic in Mars - Google Earth [Fig. 1]. Geologic map units of Thomson et al. [1] were used to define mound boundaries of the interior of Gale. Image overlays were created to correlate Thomson et al.'s units with mapped yardang units inside the crater.

Lower and middle members of the MFF were outlined in Mars - Google Earth. Formation extent was taken from U.S. Geological Survey map I-1802-B [8]. Images from the High Resolution Imaging Science Experiment (HiRISE) website were used, in several locations, to identify yardangs within the MFF and to determine yardang orientations on a finer scale.

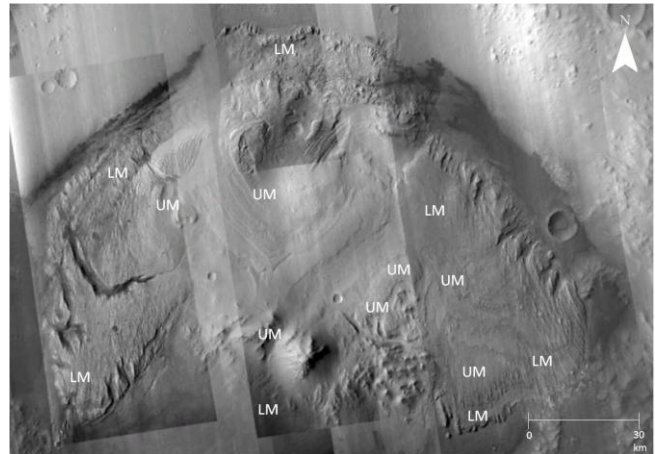


Fig.1. CTX mosaic of Gale crater with lower mound (LM) and upper mound (UM) unit labels.

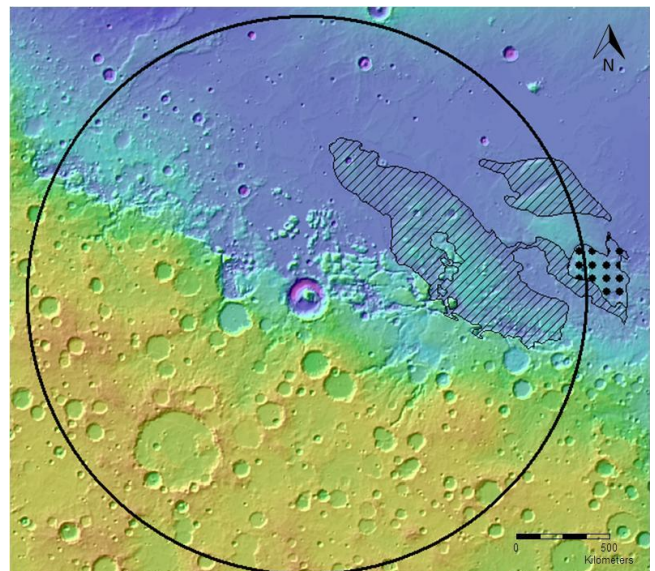


Fig.2. Image of Gale Crater from the Mars Orbiter Laser Altimeter (MOLA) dataset prepared by the U.S. Geological Survey with lower member (lines) and middle member (dots) MFF units outside of Gale. Black circle represents 1000 km radius.

Results: Yardangs are positioned parallel to the prevailing wind direction [9]. This information was used to determine feature orientation inside and outside of Gale.

Aeolian Erosion Inside Gale. The UM exhibited small scale yardangs with diverse orientations (N-S, NE-SW, and NW-SE) [Fig. 3]. In contrast, the larger yardangs of the LM exhibited a more consistent nearly N-S orientation, suggesting a N-S prevailing wind during their formation. [Fig. 3].

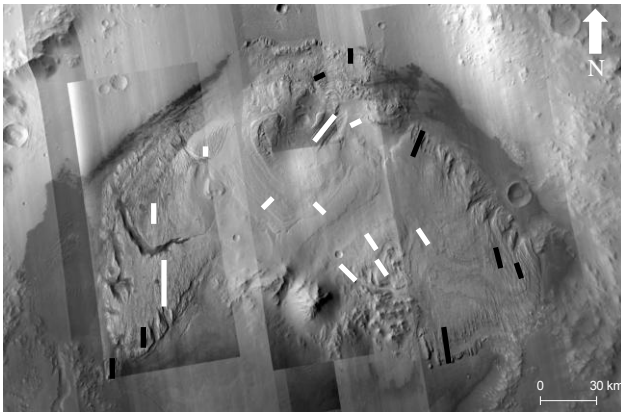


Fig.3. Wind directions (determined from yardang orientations) of LM (black) and UM (white) overlain on

Aeolian Erosion Outside Gale: Yardangs outside of Gale were predominantly located to the northeast, in the northern plains units, and along the dichotomy boundary. Yardang orientations included NW-SE, NE-SW, N-S, and E-W. The lower member of the MFF contained the majority of yardangs with a prevailing NW-SE orientation [Fig. 4]. The middle member of the MFF within 1000 km of Gale contained significantly fewer yardangs with a prevailing orientation of NW-SE. These observations suggest a predominant NW-SE eroding wind over the course of MFF erosion history.



Fig.4. NW-SE oriented yardangs located in the lower member of the MFF (HiRISE: ESP_028717_1795).

Discussion/Conclusion:

Differences in wind directions deduced from yardang orientations in the lower and upper mounds indicate changes in prevailing wind direction over the course of Gale's history. This suggests a significant gap in erosion of the lower and upper mounds. It is possible this shift is related to an overall global climatic change.

Given that the presence of an erosional unconformity separating the LM and UM is indicative of a break in Gale's depositional sequence, wind direction findings further support the idea of a two part history for the crater [1].

Yardangs within the MFF outside of Gale (lower and middle members) exhibit orientations most closely related to the UM of Gale and suggest a varied wind regime history dominated by NW-SE winds.

The age of UM sediments is unknown [1]. However, they may have been deposited at the same time as MFF material, possibly during the Amazonian [2]. Similar orientations of UM and MFF yardangs outside of Gale suggest a potential correlation in sediment erosion history.

Future investigations should focus on correlation of sediment origin through compositional analyses of yardangs inside and outside of Gale. Discoveries of the Curiosity Rover, currently en route to Mt. Sharp, will aid in a more comprehensive understanding of Gale's past.

References: [1] Thomson et al. (2011) *Icarus*, 214, 413-432. [2] Milliken et al. (2010) *GRL*, 37, L040201. [3] Kerber and Head (2010) *Icarus* 206, 669-684. [4] Irwin R.P., Watters, T.R., Howard, A.D., and Zimbleman J.R. (2004) *JGR*, 109, E09011. [5] Mandt K.E., de Silva, S.L., Zimbleman, J.R. (2008) *JGR*, 113, E12011. [6] Zimbleman J. R. and Scheidt S. P. (2012) *Science*, 336, 1683. [7] Bridges et al. (2007) *GRL*, 34, L23205. [8] Greeley R. and Guest J.E. (1985) *USGS I-1802-B*. [9] Greeley R. and Iversen J.D. (1985) Cambridge University Press, 333 p.

COMPARING VNIR AND TIR SPECTRA OF CLAY-BEARING ROCKS. A. C. Davis^{1,2}, J. L. Bishop^{1,3}, M. Veto⁴, S. Ruff⁴, T. Bristow³, W. Gates⁵, and D. Blake³, ¹SETI Institute (Mountain View, CA), ²MiraCosta College (Oceanside, CA, aprilcdavis@gmail.com), ³NASA-Ames Research Center (Moffett Field, CA), ⁴School of Earth and Space Exploration, Arizona State Univ. (Tempe, AZ), ⁵SmecTech Research Consulting (Moorabbin, Australia).

Introduction: Clays are an important indicator of aqueous processes and have been identified in numerous locations on Mars using OMEGA and CRISM data [e.g. 1,2]. Most studies base the detections of clays on lab spectra of pure minerals. Here we have measured spectra of clay-bearing rocks in order to compare these with Martian spectra. We have acquired both visible/near-infrared (VNIR) reflectance spectra and thermal region infrared (TIR) emissivity spectra in order to enable coordinated analyses of both datasets. Clays have not been observed above the detection limits in TES data using lab spectra [3], so this new data set may further TES analyses of Martian clays. XRD has also been measured in order to confirm the clay components and for comparison with CheMin data [4].

Samples: Several clay-bearing rocks were obtained for this study. The Nau-1 rock is a nontronite standard from the Clay Minerals Society and the beidellite rock is from Delamar Mine, ID (from W. Gates). A hisingerite-bearing rock came from Western Australia; remaining rocks were collected in Loma Mar and Coyote Hills, CA. Additional sample information is presented in Table 1.

Table 1

Sample ID	Sample Name	XRD Results	Sample Info
JB931	Beidellite	smectite, ~5-10% quartz	soft, white, waxy
JB1480	Hisingerite	hisingerite, siderite, quartz, feldspar, serpentine	med-hard, brown, shimmery, flaky
JB1486	Loma Mar-Lg	opal or glass, dolomite, quartz, smectites	hard, tan, grainy
JB1487	Loma Mar-Sm	smectite, opal, quartz, feldspar	hard, tan, grainy
JB1488	Coyote Hills 1	quartz	hard, brown w/trnsl veins
JB1489	Coyote Hills 2	quartz	hard, red-bwn w/trnsl veins
JB1490	Nontronite	smectite	med-hard, lime green, chalky

Methods: The rocks were processed for VNIR reflectance spectra using an ASD FieldSpecPro spectrometer that measured from 0.35-2.5 μm under ambient conditions. TIR emissivity spectra were measured using the Nicolet Nexus 670 at the Arizona State University (ASU) Thermal Infrared Mineral Spectroscopy Laboratory as in previous studies [5]. All samples were heated in an oven for ~12 hours prior to measurement and retained in a 0-2% humidity chamber

during measurement. XRD was run at NASA-Ames on crushed samples sieved to 45-150 μm .

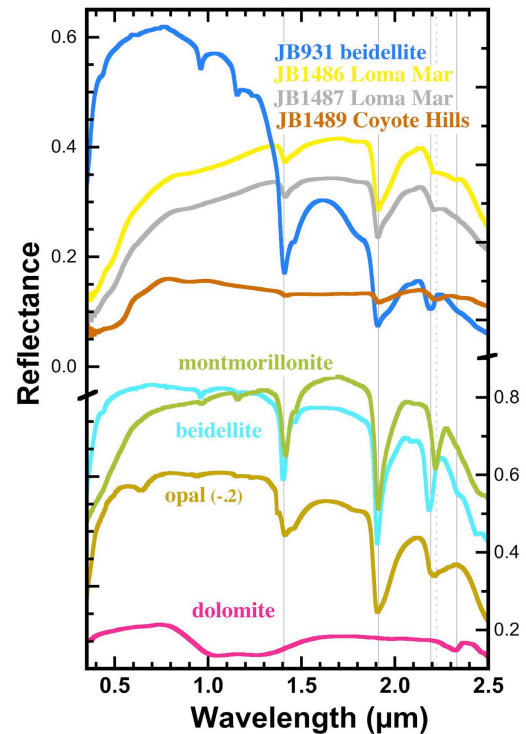


Figure 1. VNIR reflectance spectra of Al-rich clay-bearing rocks compared with spectra of minerals

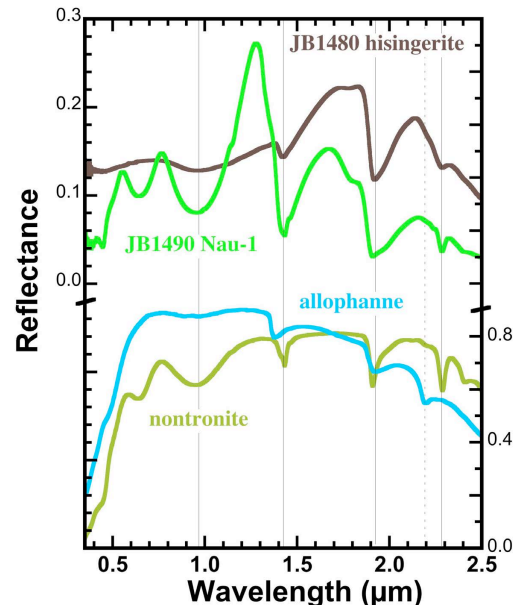


Figure 2. VNIR reflectance spectra of Fe-rich clay-bearing rocks: Nau-1 nontronite and hisingerite from Australia.

Results: VNIR spectra of phyllosilicates are best identified in remote sensing data by the OH combination bands near 2.1-2.4 μm [e.g. 6]. VNIR signatures indicative of clay minerals include stretching and bending overtone bands at 1.4 μm , an H_2O band near 1.9 μm , and stretching and bending combination bands near 2.20-2.21 μm for Al/Si, 2.29 μm for Fe^{3+} , and 2.30-2.31 μm for Mg.

Spectra of Al-clay rocks are shown in Figure 1; all of these samples exhibit bands near 1.4, 1.9 and 2.2 μm . The spectrum of the Delamar Mine beidellite-bearing rock is similar to the spectrum of the Al-smectite beidellite. XRD showed this rock to be primarily smectite with ~ 10 wt.% quartz, which does not exhibit features in the VNIR region. The two Loma Mar samples are similar including Al-smectite, opal, quartz and feldspar from XRD, but rock JB1486 also contains dolomite, which contributes a band near 2.32 μm to the spectrum. These spectra also have bands near 1.4, 1.9 and 2.2 μm but are observed close to the band centers expected for montmorillonite and opal.

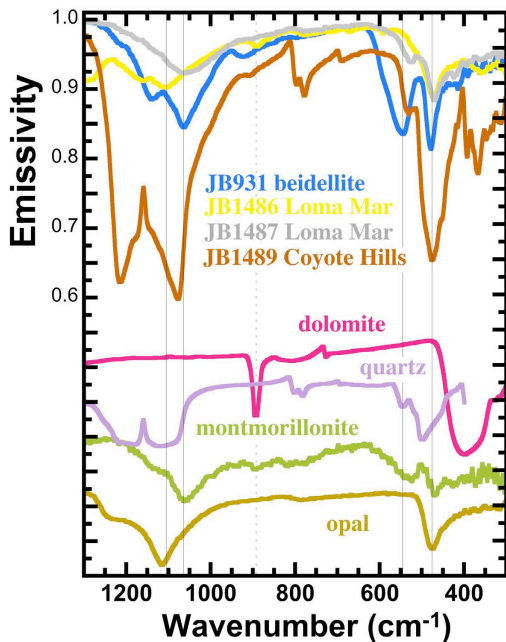


Figure 3. TIR emissivity spectra of Al-rich clay-bearing rocks. Relative emissivity spectra of pressed pellets of montmorillonite [7] and opal [8] spectra and inverse reflectance spectra of dolomite and quartz [9] are shown for comparison.

Spectra of Fe-rich rocks containing hisingerite and nontronite are shown in Figure 2. Hisingerite is an amorphous material similar to allophane but with a higher Fe content. As no spectrum is available for hisingerite, a spectrum of allophane is shown along with that of nontronite for comparison. Spectra of the Nau-1 and hisingerite rocks have bands at 1.42, ~ 1.9 and 2.29 μm . The H_2O band occurs near 1.91 μm for nontronite, similar to that of montmorillonite, but occurs at 1.92 μm for hisingerite and is broadened, similar to the feature observed for allophane.

TIR spectra of dioctahedral phyllosilicates exhibit a doublet near 450-600 cm^{-1} , while trioctahedral phyllosilicates have a single band near 475 cm^{-1} [e.g. 10]. The beidellite rock spectrum in Figure 3 is similar to the montmorillonite spectrum with an Si-O band near 1050 cm^{-1} and an Si-O bending doublet near 470 and 550 cm^{-1} . The Loma Mar samples contain both smectite and opal and have an asymmetric doublet for the bending vibration. The spectrum of Loma Mar rock JB1486 also has carbonate features consistent with dolomite. Although the spectrum of the Coyote Hills rock JB1489 looks very similar to that of quartz in this spectral range, it exhibits bands consistent with Al-clay or opal in the VNIR region. In Figure 4, the hisingerite and Nau-1 spectra exhibit Si-O vibrations consistent with Fe-clays. The Nau-1 rock spectrum is similar to the particulate nontronite spectrum, but has stronger features. The hisingerite rock spectrum has broader bands similar to its cousin allophane; however there is a single broad Si-O bending vibration rather than a doublet as observed in the spectra of nontronite and allophane. This single band is indicative of absorption band overlap seen in trioctahedral clays.

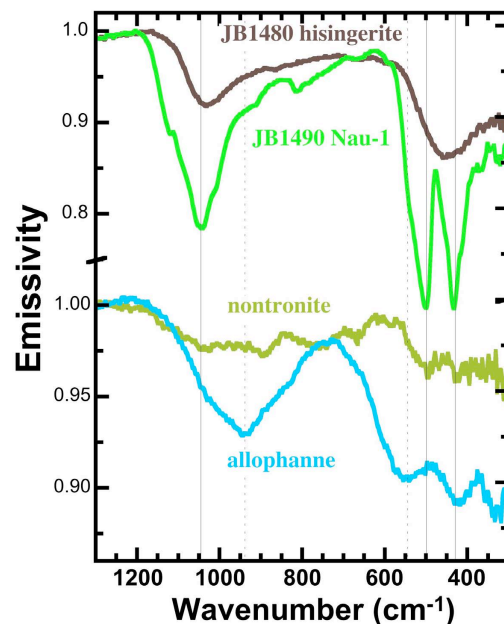


Figure 4. TIR emissivity spectra of Fe-rich clay-bearing rocks compared to nontronite [7] and allophane [11] spectra.

Acknowledgements: Support from the CAMPARE program is greatly appreciated.

References: [1] Murchie et al. (2009) JGR 114, doi:10.1029/2009JE003342. [2] Carter et al. (2010) Science 328, 1682. [3] Christiansen et al. (2001) JGR 106, 23823. [4] Blake et al. (2013) Science 341, doi:10.1126/science.1239505. [5] Christensen et al. (2000) JGR 105, 9735. [6] Bishop et al. (2008) Science 321, 830-833. [7] Bishop et al. (2008) Clay Miner. 43, 35-54. [8] Rampe et al. (2012) Geology, doi:10.1130/G33215.1 [9] Salisbury et al. (1991) Infrared Spectra of Minerals. [10] Michalski et al. (2005) Icarus. [11] Bishop et al. (2013) Clays Clay Miner. 61, 57-74.

SIMULATING MARTIAN CONDITIONS: METHANOGEN SURVIVABILITY DURING FREEZE-THAW CYCLES. S. Djordjevic^{1,2}, R. L. Mickol¹, T. A. Kral³, ¹Arkansas Center for Space and Planetary Sciences, University of Arkansas, Fayetteville, Arkansas, rmickol@uark.edu ²University of Illinois at Urbana-Champaign, Champaign, Illinois, djordje2@illinois.edu, ³Department of Biological Sciences, University of Arkansas, Fayetteville, Arkansas, tkral@uark.edu

Introduction: Methanogens are obligate anaerobes that use molecular hydrogen as an energy source and carbon dioxide as a carbon source to produce methane. They are classified as Archaea and are found in many extreme environments, including hydrothermal vents, volcanoes, and also the human microflora. The current Martian atmosphere is low in pressure, very dry (hyper-arid), and high in radiation, and thus the surface is not suitable for life. However, the subsurface contains permafrost, liquid water [1], and trace amounts of methane [2, 3]. Thus, it is proposed that these Archaea are able to persist in Martian conditions.

According to data obtained from NASA's Mars Science Laboratory between August 2012 and the present time, the maximum and minimum temperatures on Mars have ranged from +20°C to -100°C (Fig. 1) [4]. These conditions might be suitable for methanogenic growth. The goals of this experiment are to use freeze-thaw cycles and measure methanogen growth using gas chromatography in order to further understand temperature constraints on growth.

Methods: Four types of methanogen growth media were prepared according to Kendrick and Kral [5]. The strains used were *Methanothermobacter wolfeii*, *Methanosarcina barkeri*, *Methanobacterium formicicum*, and *Methanococcus maripaludis*. The media were autoclaved for sterilization, inoculated with 0.5 mL of each respective methanogen, and grown in their respective media and optimal temperature at ambient pressure: *M. wolfeii* at 55°C, *M. barkeri*/*M. formicicum* at 37°C, and *M. maripaludis* at room temperature (22°C). Growth was monitored in the form of methane production throughout the duration of the experiments via gas chromatography.

Experiment 1. Following seven days at their respective incubation temperatures, all four of the methanogen inoculums were exposed to 4°C for seven days and incubated for six days, respectively (Fig. 2).

Experiment 2. Each inoculum was placed in either five grams of sand or ten grams of sand. Following fifteen days at their respective incubation temperatures, all four of the methanogen inoculums were exposed to 4°C for eight days, -20°C for eleven days, -80°C for eight days, and then incubated for seven days, respectively (Fig. 3).

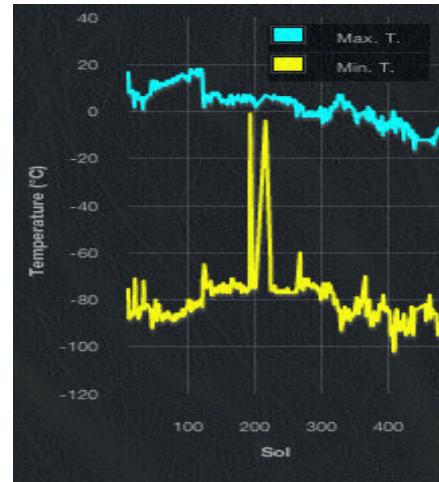


Figure 1. Ground temperature data from the Rover Environmental Monitoring System from early-August 2012 to the present time at Mars' Gale Crater [4].

Results: Only methane concentrations above 1% were considered.

Experiment 1. Following seven days of incubation at their respective temperatures, *M. wolfeii*, *M. maripaludis*, and *M. formicicum* showed appreciable growth after exposure to 4°C and incubation. *M. barkeri* did not show appreciable growth during the experiment and these data were not included (Fig. 2).

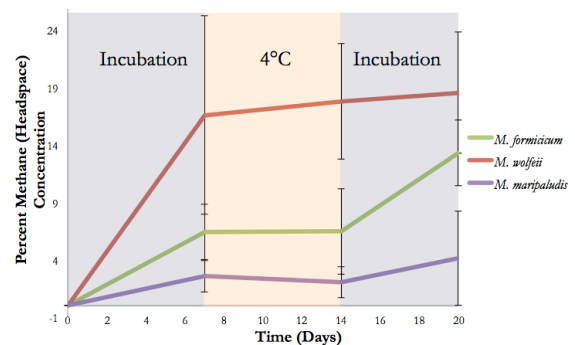


Figure 2. Percent methane (headspace) concentrations for each of three methanogen strains (*M. wolfeii*, *M. maripaludis*, *M. formicicum*) following a seven day incubation period, a 4°C freeze-thaw cycle, and subsequent incubation period.

Experiment 2. Following fifteen days of incubation at their respective temperatures, *M. formicicum* showed appreciable growth only with ten

grams of sand at -20°C . *M. wolfeii* showed increased methane production at -20°C and the ten gram inoculum produced marginally higher levels of methane. *M. maripaludis* did not show appreciable growth and these data were not included (Fig. 3).

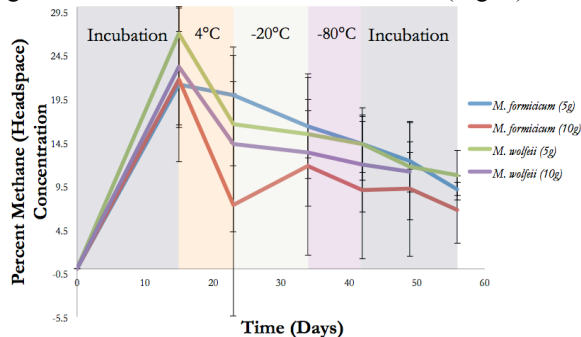


Figure 3. Percent methane (headspace) concentrations for each of two methanogen strains (*M. wolfeii* and *M. formicicum*) in five and ten gram inoculums following a seven day incubation period and various freeze-thaw cycles.

Discussion: *M. wolfeii* showed the largest increase in growth during the incubation period for Experiment 1 and Experiment 2. In Experiment 2, *M. wolfeii* did not show growth at any temperature (besides incubation). The decrease in growth at 4°C was not an expected result because this species showed growth at 4°C in Experiment 1. This result might be due to errors in the measurements of methane concentrations. Thus, the -20°C to -80°C temperature range might be a temperature constraint for this species.

M. formicicum showed an increase in growth during the incubation period for Experiment 1 but only an increase in growth during the -20°C in Experiment 2. Thus, *M. formicicum* might be able to survive lower temperatures more easily than *M. wolfeii*. In Experiment 2, *M. formicicum* grew slightly at -20°C but did not grow at -80°C . Thus, the -20°C to -80°C temperature range might be a temperature constraint for this species.

M. maripaludis showed only marginal changes in growth during Experiment 1. This result might be due to improper lab technique.

M. barkeri did not show appreciable growth during either experiment. This result might be due to improper lab technique and/or low survivability.

It is important to note that decreases in methane concentration were expected as samples were removed from the test tubes for testing. Increases in methane concentration were not expected at low temperature (indicating active growth) because methane is poorly soluble in water at low temperatures [5]. These two factors contribute to decreases in methane concentrations over time.

Conclusion: Four different species of methanogen were used to analyze the effect of low temperature freeze-thaw cycles on the growth of each of the respective species. These experiments provide preliminary data for the growth of *M. wolfeii*, *M. formicicum*, *M. barkeri*, and *M. maripaludis* in low-temperature freeze-thaw cycles. This study has shown that some, but not all, of the strains of methanogen used in this study can withstand prolonged low-temperature conditions, for at least one week at a time. Further studies will continue to analyze the temperature constraints for these Archaea in order to understand implications for life in Martian conditions. Long-term freeze/thaw cycle experiments using *M. wolfeii* and *M. formicicum* were also conducted (R.L. Mickol and T.A. Kral, LPSC XLV, this conference).

References: [1] S.W. Squyres et al. (2006) *Science* 306, 1709–1714. [2] V. Formisano et al. (2004) *Science* 306, 1758–1761. [3] V.A. Krasnopolsky et al. (2004) *Icarus* 172, 537–547. [5] Rover Environmental Monitoring Station (REMS) aboard the Mars Science Laboratory (2013), courtesy of NASA/JPL-Caltech/CSIC-INTA. [4] Kendrick, M.G. and Kral, T.A. (2006) *Astrobiology*, 6, 546–551. [5] Duan, Z. and Mao, S. (2006) *Geochimica et Cosmochimica Acta* 70, 3369–3386.

Acknowledgements: Special thanks to Dr. Julia Kennefick and NSF Grant #1157002.

COMPARING GEOLOGIC DATA SETS COLLECTED BY PLANETARY ANALOG TRAVERSES AND BY STANDARD GEOLOGIC FIELD MAPPING: DESERT RATS DATA ANALYSIS

Wanda Feng¹, Cynthia Evans², John Gruener², and Dean Eppler², ¹Departments of Geology and Astronomy, Smith College, Northampton, MA (wfeng@smith.edu), ²NASA, Johnson Space Center, Houston, TX 77058 (cindy.evans-1@nasa.gov, john.e.gruener@nasa.gov, dean.b.eppler@nasa.gov).

Introduction: Geologic mapping involves interpreting relationships between identifiable units and landforms to understand the formative history of a region. Traditional field techniques are used to accomplish this on Earth. Mapping proves more challenging for other planets, which are studied primarily by orbital remote sensing and, less frequently, by robotic and human surface exploration. Systematic comparative assessments of geologic maps created by traditional mapping versus photogeology together with data from planned traverses are limited [1]. The objective of this project is to produce a geologic map from data collected on the Desert Research and Technology Studies (RATS) 2010 analog mission using Apollo-style traverses in conjunction with remote sensing data. This map is compared with a geologic map produced using standard field techniques [see Bleacher et al.; Skinner et al.; Eppler et al.; this session].

Background: The Apollo missions (1961-1972) yielded data that revolutionized our understanding of lunar geology. No subsequent planetary human exploration has been conducted; consequently, there has been no opportunity to field check Apollo results with more detailed field investigations. The Desert RATS missions (1997-present) have been conducted in northern Arizona to exercise science operations, test multi-mission space exploration vehicles (MMSEVs) and extravehicular activity (EVA) protocol to prepare for future human exploration [2]. Since 2009, these analog tests have used “Apollo-style” traverse planning and EVAs to understand regional geology and sample conjectured geologic units [3-4], but the strengths and weaknesses of this style of planetary exploration have yet to be examined.

The most extensive RATS mission was completed in 2010 in the San Francisco Volcanic Field north of Flagstaff, AZ. Over the course of 14 days, a 580 km² area was explored by 2 prototype pressurized rovers with crews of astronauts and geologists [4]. 448 samples were collected from 69 EVA stations [5]. This study took a 15 km² field area adjacent to SP mountain in order to evaluate in further detail using RATS data and data derived from standard geologic mapping techniques. Although this area has been studied at a reconnaissance scale [6-7], detailed geologic mapping has not been carried out on this volcanic center.

Methods: Much like the Apollo Missions, RATS yielded samples, photographs, and crew videos for

further study with remote sensing data. In our study area, 19 EVA stations from 5 days contributed to 122 samples. Sample locations were georeferenced using crew videos, field photos, and GPS data from the EVA backpacks using Google Earth and Picasa. These locations, as well as crew and rover traverses, were mapped for each station in ArcMap (Fig. 1). Sample contexts and compositional characteristics (from hand sample examination) allowed for the differentiation between different sedimentary and volcanic units. The age relationships of the units were finally determined by geomorphologic relationships and relative weathering of the samples.

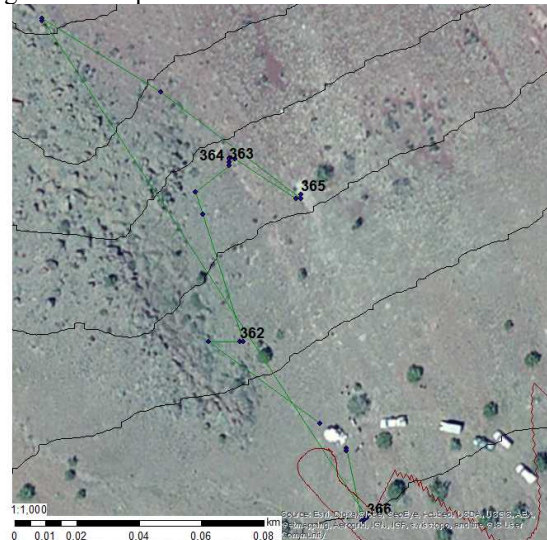


Figure 1: 1:1500 image of site 25B with sample numbers, EVA track (green), rover track (red). The basemap is ESRI world imagery, including an aerial view of the MMSEV.

Results: The 1:24,000 scale product map (Fig. 2) was created in ArcMap 10.1. The photogeologic pre-mission units [3] were re-evaluated using RATS 2010 data.

The field area included a basement sedimentary unit, several volcanic flows, and cinder cones. The sedimentary basement units, originally mapped as two distinct units [3], were determined to be one unit of limestone (ls). Distinguishing between the different volcanic flows and cones proved more difficult. The oldest identifiable basalt flow (b1) was interpreted by photo-interpretation; however, due to the lack of samples and distinguishing topography, the number of flows is indeterminate. The b1 flow was inferred to be older than the other basalt flows by superposition.

The central volcano complex was mapped as two cones. On the basis of RATS 2010 samples, the northern cone (p1) includes massive lava flows with olivine and pyroxene phenocrysts, while the southern cone (p2) is composed of pyroxene- and plagioclase-phenocryst dominated agglutinates. The topography and sample compositions suggest that p1 is related to and constructed on top of the adjacent flow (b2).

The southeastern corner of the study area was interpreted as an older, weathered flow (b4) of a plagioclase-rich agglutinate basalt. The west side of the study area comprises another basalt flow (b3) composed of massive, vesicular basalt rich in olivine and pyroxene phenocrysts. The morphology of the b3 flow suggests that it is younger than b4. The clear lobate features of both the b3 and b4 flows supports that the flows are relatively younger than the adjacent central cone complex. SP flow (b5) and SP mountain (p3) are the most recent volcanic features in the study area. Both units are composed of massive and vesicular basalt rich in olivine and plagioclase. The map boundaries for these units remain unaltered from the pre-mission map.

The interpreted boundaries and types of the surficial units (originally referred to as surficial plains) were difficult to validate based on the RATS data. The limited data and photo-interpretation results suggest that the units include alluvium (al) and colluvium (cl) possibly eolian deposits and ashfall.

Discussion: The RATS 2010 data is spatially limited, as manifested on the map (Fig. 2). Mapping the study area has therefore involved interpolation of rock mineralogies and unit boundaries through photo interpretation. However, our detailed analysis of the RATS data indicate the high quality and efficacy of the pre-mission mapping and traverse planning [3-4]. The compositional study of the limestone basement and differentiation between lava flows and cinder cones reflects that the pre-mission process of identifying traverse and sampling locations was successful. At the same time, there are regions that were not sampled or visited by the RATS 2010 traverses that might have improved our maps and understanding of the geology of the area. These limitations to the Desert RATS data set create discrepancies between our map and the map constructed by the field team.

References: [1] Tanaka K. et al. (2009) *Planetary & Space Sci.*, 57, 510-532. [2] Ross A. et al. (2013) *Acta Astronautica*, 90, 182-202. [3] Skinner J. A. and Fortezzo C. M. (2013) *Acta Astronautica*, 90, 242-253. [4] Hörz F. et al. (2013) *Acta Astronautica*, 90, 254-267. [5] Gruener J. et al. (2013) *Acta Astronautica*, 90, 406-415. [6] Billingsley G. H. et al. (2007) *USGS*. [7] Bloomfield A. L. and Arculus R. J. (1989) *Contributions to Mineralogy & Petrology*, 102, 429-453.

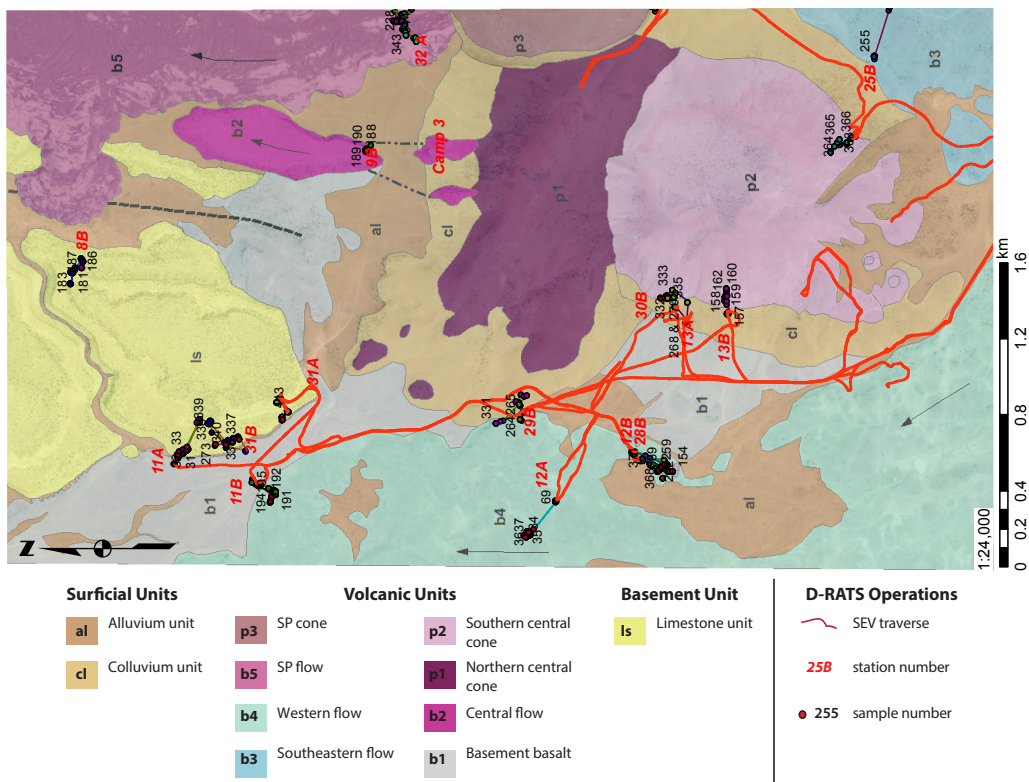


Figure 2. A 1:24,000 map of the study area with units, sample numbers, EVA and rover tracks.

ALTERATION OF LUNAR ROCK SURFACES THROUGH INTERACTION WITH THE SPACE ENVIRONMENT. A. M. Frushour¹, S. K. Noble², R. Christoffersen³, and L. P. Keller⁴. ¹Department of Geology, Appalachian State University, ASU Box 32067, Boone, NC 28608 (frushouram@appstate.edu), ²NASA GSFC, Mail Code 691, Greenbelt, MD 20771 (sarah.k.noble@nasa.gov), ³Jacobs, NASA Johnson Space Center, MC JE23, 2101 NASA Pkwy, Houston, TX 77058, USA, roy.christoffersen-1@nasa.gov, ⁴NASA Johnson Space Center, Mail Code KR, 2101 NASA Pkwy, Houston, TX 77058, USA, lindsay.p.keller@nasa.gov

Introduction: Space weathering occurs on all exposed surfaces of lunar rocks, as well as on the surfaces of smaller grains in the lunar regolith. Space weathering alters these exposed surfaces primarily through the action of solar wind ions and micrometeorite impact processes. On lunar rocks specifically, the alteration products produced by space weathering form surface coatings known as *patina* [1]. Patinas can have spectral reflectance properties different than the underlying rock. An understanding of patina composition and thickness is therefore important for interpreting remotely sensed data from airless solar system bodies. The purpose of this study is to try to understand the physical and chemical properties of patina by expanding the number of patinas known and characterized in the lunar rock sample collection.

Methods: We searched the Lunar Sample Compendium (2013) [2] to find rock samples which have been reported to have patina coatings. The search criteria included any mention of patina, micrometeorite craters, or “zap pits” in the Compendium sample descriptions. Available thin sections of these rock samples in the JSC Sample Curatorial Center were then studied with a petrographic microscope to survey samples for patina. Once patina candidates were identified, the sections were imaged using a JEOL 7600F field-emission analytical scanning electron microscope (FE-SEM). The thickness, lateral extent, microstructure and chemical composition of the patinas were measured using the FE-SEM capabilities.

Results: Relative to previous studies [1,3,4,5] we increased by six (6) the number of lunar rock samples with characterized patinas. The studied patinas were in thin sections 15485,6; 12017,23; 14301,85; 10045,39 and 60025,163.

Thin section 15485,6 is a vitrophyric pigeonite basalt that has a discontinuous patina that is about 7 mm long and varies in thickness from about 10 μm to 350 μm (Fig. 1a,b). This patina is composed of multiple layers, each on the order of 1 to 10 μm thick. Each layer is generally defined by rounded grains of glass <1 to 10 μm in diameter with a sub-layer of glass <1 to 5 μm thick separating each layer. In some areas the glass layers are more fragmental and in others more massive; layer boundaries become indistinguishable where this occurs. The individual layers are not flat, but rather

undulatory. There are areas where the patina thickness is composed of just one layer and other areas that have tens of layers. The glass grains and mineral fragments commonly fill in depressions in the outer surface of the rock. One localized region containing spherules of nanophase metallic Fe was identified. Based on energy-dispersive (EDS) compositional spectrum imaging, and spot analyses, the 15485,6 patina is fairly uniform in composition with only subtle variations in Al and Mg (Fig. 1b).

12017,23 is a pigeonite basalt that has a continuous layer of glassy patina that extends about 4.5 mm and varies from ~35 μm to ~600 μm thick. The patina consists mostly of silicate glass with entrained vesicles, mineral fragments, and spherules of nanophase Fe (Fig. 1c). The patina contains vesicles on the scale of about 10 to 100 μm . There are two areas of nanophase Fe. One area consists of a chain-like linear arrays of spherules <1 to 3 μm in size. The other area is in the form of multiple thin layers 1 to 5 μm thick. There are also partially melted rock fragments near the surface of the rock. The composition of the 12017,23 patina glass is overall fairly homogeneous, with the exception of local regions of partially or wholly melted minerals, such as ilmenite.

14301,85 is a regolith breccia that has a layer of patina approximately 2 mm long which ranges from 5 to 50 μm in thickness. The patina has distinct sub layers, one composed predominantly of mineral grain and lithic fragments, the other containing partially melted mineral grains and nanophase Fe. The inner layer may or may not be patina, because it has a microstructural resemblance to types of clasts in the rock interior.

10045,39 is an ilmenite low K basalt which has a continuous patina that is about 400 μm long and varies from 1 μm to 130 μm thick. The patina is made mostly of a mix of highly vesicular glass and lithic fragments (Fig 1d). The glass is spread out along about half of the patina and contains schlieren-like layers with a high concentration of nanophase Fe. The thickest part of the patina contains lithic fragments that are angular to sub-rounded with various degrees of melting. The patina has an area ~100 μm long composed predominantly of unconsolidated mineral fragments.

60025,163 is a ferroan anorthosite which has a continuous patina about 1 mm long that varies from 5 μm

to 50 μm thick. The patina is composed of a single layer of silicate glass that is essentially identical in composition to the anorthositic host rock such that the boundary between the patina and rock surface is compositionally indistinguishable. The glass does, however, contain some large nanophase Fe^0 blebs in localized regions.

Discussion: Wentworth et al. [1] originally proposed a classification scheme for lunar rock patinas with three main categories. “Fragmental” patinas are composed predominantly of aggregated rounded to sub-rounded particles, well sorted in the 1-5 μm size range and held together by various degrees of melt welding. “Glazed” patinas are composed of continuous glass layers in which it is generally difficult to distinguish different small glassy constituents, i.e. the glass is microstructurally homogeneous. “Classical” patinas are also dominantly glassy, but have complex microstructures containing multiple identifiable glass units, typically referred to as “splats” or “pancakes”.

We find that some, but not all, the patinas characterized in the current study fit well with the Wentworth et al. [1] classification. 15485,6 has attributes fairly close to the fragmental type, particularly because the glassy spherules defining the layers are well sorted with respect to size. 60025,163 falls well into the “glazed” category given that it dominantly consists of

continuous, homogeneous glass. 12017,23 fits somewhat into the glazed patina type, but it also contains regions with mineral fragments, making it a composite type not well covered by the Wentworth [1] scheme. Although 14301,85 clearly consists of fragmental material, the fragments are angular and poorly sorted, not consistent with Wentworth’s fragmental designation. 14301,85 is an example of a patina type we would call heterogeneous fragmental, as an addition to the Wentworth scheme. 10045,39 is another example of a very heterogeneous patina, with complex glassy regions, and mineral fragments, that does not fit existing types and should define a new “heterogeneous” type.

Conclusions: We were successful in finding more patinas, and our results considerably expand upon the known microstructural and morphological diversity of lunar rock patinas. The variety of patinas found illustrate that they do not easily fall into the previous categories defined by Wentworth et al. [1].

References: [1] Wentworth S. et al. (1999) *Meteoritics & Planet. Sci.*, 34, 593-603. [2] Meyer C. (2012) Lunar Sample Compendium. Retrieved June 2013. From: <http://curator.jsc.nasa.gov/lunar/lsc/index.cfm> Lunar Sample Compendium (2013). [3] Noble et al. (2007) LPSC38 Ab#1359. [4] Noble et al. (2012) LPSC43 Ab#1239 [5] Noble et al. (2013) LPSC Ab#1298.

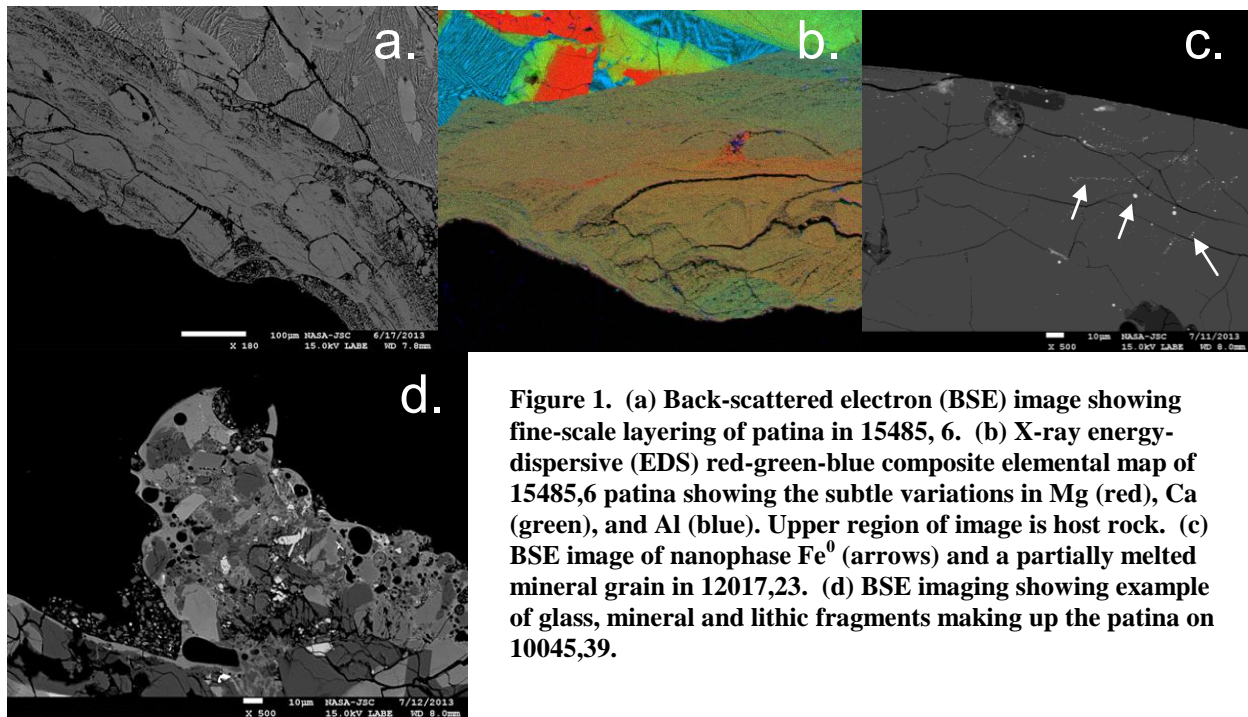


Figure 1. (a) Back-scattered electron (BSE) image showing fine-scale layering of patina in 15485, 6. (b) X-ray energy-dispersive (EDS) red-green-blue composite elemental map of 15485,6 patina showing the subtle variations in Mg (red), Ca (green), and Al (blue). Upper region of image is host rock. (c) BSE image of nanophase Fe^0 (arrows) and a partially melted mineral grain in 12017,23. (d) BSE imaging showing example of glass, mineral and lithic fragments making up the patina on 10045,39.

DETERMINING THE DUNE-CONSTRUCTING WIND REGIME IN EASTERN OLYMPIA UNDAE, MARS. G. C. Garcia¹ and L. K. Fenton², ¹The University of Texas-Pan American 1201 W. University Dr., Edinburg, TX 78539 (ggarcia@broncs.utpa.edu), ²SETI Institute, 189 Bernardo Ave, Mountain View, CA 94043, USA.

Introduction: Ewing et al. [1] looked in one area of Olympia Undae on Mars and found the dunes were influenced by two main winds: an older wind from the ENE that is responsible for creating large dune crests and a second younger wind from the NE that has begun to reorient the older crests and has produced secondary longitudinal dunes. This wind originated at Olympia Cavi, a scarp that has formed at the edge of Planum Boreum. The goal of this work is to determine the wind regime in eastern Olympia Undae. This study focuses farther east in Olympia Undae, where a similar pattern is evident in images, but where winds from Olympia Cavi are not likely to strongly influence bedform morphology. This is of interest beyond just aeolian morphology: the eastern portion of the sand sea is higher in gypsum abundance relative to the rest of Olympia Undae [2], and determining the wind regime there may help identify the origin of gypsum sand.

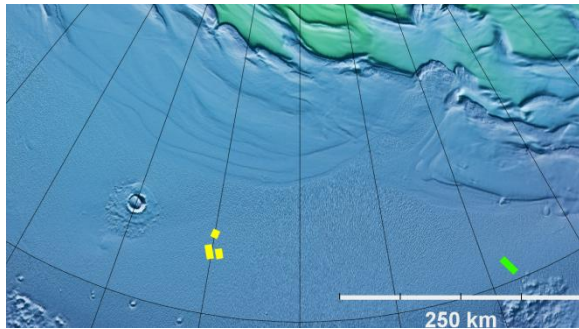


Figure 1. Eastern Olympia Undae in the north polar region of Mars. The green box represents the image analyzed in this work, and the yellow box indicates work previously conducted by [1].

Methods: In order to get a mean crestline orientation, we mapped crestlines of dunes and ripples in our study area through the use of geographic imaging system (GIS) software, JMARS [3]. Focusing on High Resolution Imaging Science Experiment (HiRISE) image ESP_027803_2605 (see Fig. 1, 2), we compiled four sets of bedform crestline data. Each set was classified based on morphology type, including primary and secondary dunes, coarse-grained ripples, and ~2 m wavelength sand ripples (see Fig. 2). Figure 3 shows resulting rose diagrams of the mapped crestlines binned by 10° intervals. These results were then used to estimate the incident bedform-constructing winds. The concept of maximum gross bedform-normal transport dictates that the orientation of a bedform crestline is

determined by all incident sand transporting winds [4]. If all winds of saltation strength are known, the resulting bedform trend can be predicted. In the case of planetary geomorphology, where wind measurements are lacking, it is necessary to invert the problem to solve for the wind regime. Using this technique bedform morphology and inferred wind directions can be used to estimate bedform constructing wind regimes [5].

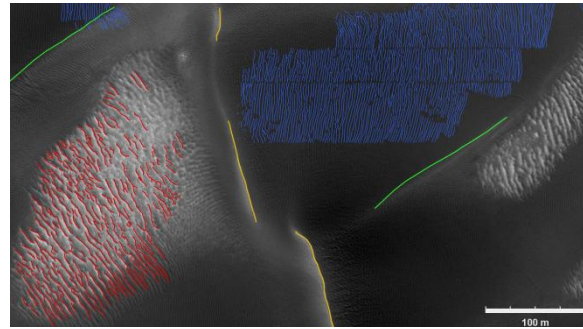


Figure 2. A portion of HiRISE image ESP_027803_2605. Each line color represents a different set of bedforms. The orange crestlines are primary dunes, green crestlines are secondary dunes, red lines are coarse-grained ripples, and the blue lines are sand ripples.

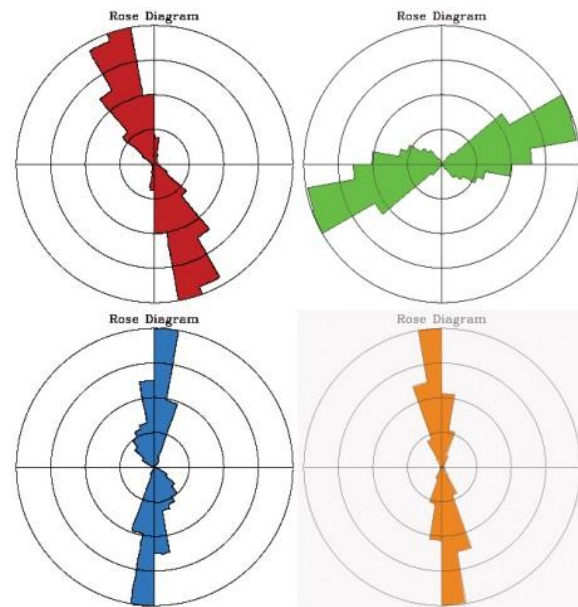


Figure 3. Rose diagrams showing crestline orientations for each set of lines mapped in GIS software, JMARS. The colors reflect the color set for each dune type: Orange is for primary dunes, green for secondary dunes, red for coarse-grained ripples, and blue for sand ripples.

Results: Starting with the oldest feature, the *primary dune* crestline orientation likely reflects a transverse dune formation made by the predominant easterly winds that have been prevalent throughout the Olympia Undae region for many years [1]. Maintaining a general north to south orientation, slipfaces are visible on the western side of most, if not all, of the peaks. The *secondary dunes* are less simple to interpret. As dunes grow large enough, it is possible for winds to become channeled between the structures and in turn begin to transform the morphology. Following the interpretation of [1], the secondary dunes appear to reflect a longitudinal pattern. This inference is based on the orientation of the *coarse-grained ripples* that appear within the troughs of the primary dunes. Since the coarse-grained ripples are relatively small features (~30 m wavelength), they may or may not reflect recent winds, as the grains are larger, and require either more force, or more time for formation. This is also assuming that the coarse ripples are transverse elements like the *sand ripples*. As of now, there is no evidence to prove that ripples are anything but transverse, but it is not wise to rule out the possibility of alternate methods of formation. Sand ripples, comprising the smallest accumulation of sediments in the area, indicate the most recent sand-transporting winds.

Discussion: From the rose diagrams, and inferences about the sand ripples, we can conclude a first wind vector from 95° (red line in Figure 3). At this

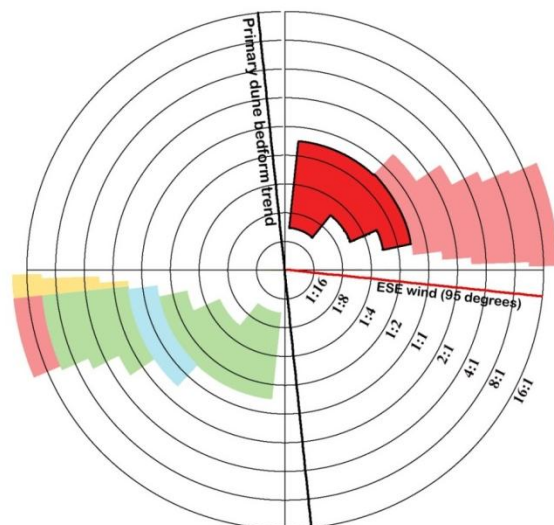


Figure 4 IMGBNT for primary crestlines. The ESE wind was inferred from sand ripples; here it combines with a second wind depicted as a colored region. Red indicates a transverse regime, green is an oblique regime, blue indicates a longitudinal regime, and yellow is reversing. The bold region is the most likely set of possible second winds that could combine with the inferred ESE wind to create the observed primary dune crestlines.

point, we know the primary dune bedform trend (black line in Figure 3), have inferred one wind vector, and now, using the method of IMGBNT, have come up with possible solutions for the second wind vector (shaded regions in Figure 3). The graph is expressed as transport ratio versus orientation. The middle radius circle represents a transport ratio of 1, meaning that both wind vectors have the same magnitude. Any larger radius represents a ratio where the unknown second wind is stronger than the ESE wind, and any smaller radius represents a ratio where the unknown wind is weaker than the ESE wind. From observation of the morphology, there is no indication of a wind coming from the SW direction, so every possible wind vector listed in the third quadrant of the histogram has been eliminated. Likewise, since the ESE wind appears to be the dominant wind vector, each possibility outside of the 1:1 radius has been eliminated. This leaves only the likelihood of a second wind from a NE direction that, at max, transports half the sand as the ESE wind, creating a transverse wind regime responsible for the formation of the primary dune crestlines in the area.

Conclusion: From comparison with other work within the Olympia Undae dune field, our results appear to differ significantly for the coarse-grained and sand ripples. The theory behind this suggests that a strong NE wind coming from Olympia Cavi is helping to significantly alter the dune morphology [1]. Since the study area that has been analyzed here is east of this erosional feature, we do not observe the influence of this strong wind. However, the secondary dunes that appear in both areas have a similar orientation. This leads to the idea that the secondary dunes are being created from another source. There could still be reason to believe that a NE wind is combining with the dominant easterly wind to create a longitudinal secondary dune, where the Olympia Cavi winds only aid in speeding up the process. Future work to be conducted is to get an IMGBNT histogram for the secondary dunes and compare it with the primary dune graph and see if there is evidence to support this theory.

References: [1] Ewing, R. C., et al. (2010). *J. Geophysical Res.*, 115, E08005. doi:10.1029/2009JE003526. [2] Langevin et al. (2005). *Science*, 307, doi:10.1126/science.1109091. [3] Gorelick, N. S. (2003) LPSC XXXIV, Abst. #2057. [4] Rubin, D. M. & Hunter, R. E. (1987). *Science*, 237(4812), 276–8. doi:10.1126/science.237.4812.276. [5] Fenton, L. K. et al. (2013). *Icarus*, doi:10.1016/j.icarus.2013.04.001

REVISITING SHATTER CONES AT SUDBURY. K. T. Hansen¹ and G. R. Osinski¹, ¹Canadian Lunar Research Network/Centre for Planetary Science and Exploration, University of Western Ontario (khansen6@uwo.ca).

Introduction: After their initial discovery in Sudbury, Ontario by R.S. Dietz in the 1960's [1], shatter cones, or striated, conical-fractured shock features in rocks believed to be the result of high-pressure induced shock waves [2], were used as evidence confirming an impact origin of this highly deformed area [1, 3]. Although shatter cones have subsequently been recognized as the sole macroscopic shock features used to distinguish high-velocity impacts [4], there remains uncertainty and debate surrounding specific aspects of their formation and distribution [5-8].

The Sudbury area has been the subject of intense research as it is a geologically complex area with plentiful mining and academic interests. However, although there has been extensive study of the Sudbury impact crater itself, the same can not be said for shatter cones in the area. There have only been a few shatter cone maps produced, such as the original Bray [9] map of 1966 and subsequent updates [10] as well as the relatively recent (2008) Ames et al. [11] maps.

In Summer of 2013, Osinski et al. [12] presented the preliminary results of a long-term, comprehensive study of Sudbury shatter cones launched in 2010 which will seek to provide a more detailed understanding of both their distribution and physical characteristics as well as the original geomorphology of the crater itself. These data were primarily collected during the Autumn 2012 "Impact Cratering Short Course and Field Training Program", and although there were a few similar findings with past studies [13, 14] there were mostly inconsistencies and new observations [12, 15], many of which will prove both interesting and beneficial under further investigation.

Continuing study of this Sudbury initiative will be prudent and will increase analyzable data. Aside from the preliminary data from Osinski et al. [12] and field work in Autumn 2013, there will also be a comprehensive shatter cone mapping and analysis field project undertaken in Summer 2014. This project will supplement the main study while maintaining the objectives of 1) determining the spatial distribution and radial extent of shatter cones around the Sudbury structure; 2) determining the orientation and systemic variation of shatter cones; 3) and investigating the morphology, morphometry, and microscopic shock effects of shatter cones within and around the Sudbury Basin.

Methodology: The Summer 2014 field project as well as subsequent future endeavours and short courses will continue to implement the methodology and techniques as described in Osinski et al. [12]. There will be extensive use of Global Positioning System (GPS)

units in order to accurately record the location of each shatter cone-bearing outcrop, paired with geotagged photographs. There will also be recorded descriptions of each shatter cone outcrop's lithology, size, orientation of apices, cone development level, as well as the trend and plunge of the shatter cone striations and strike and dip of the bedding. Field sample collection of shatter cones and related specimens will prove useful in optical petrography and other laboratory analysis.

Future Work: Although the Summer 2014 field project remains forthcoming, data and observations retrieved from this effort will be synthesized with the preliminary Osinski et al. results [12] as well as data from Autumn 2013. Earlier maps [9-11] will be used as a guide, however this study's complete re-mapping of Sudbury shatter cones will use meticulous methodology and provide additional qualitative and quantitative descriptions. These efforts will further the development of a highly detailed and structured GIS shatter cone database of the Sudbury impact structure.

References: [1] Dietz R. S. (1964) *J. of Geol.*, 72, 412-434. [2] Dietz R. S. (1959) *J. of Geol.*, 67, 496-505. [3] Dietz R. S. and Butler L. W. (1964) *Nature*, 204, 280-281. [4] French B. M. and Koeberl C. (2010) *Earth Sci. Rev.*, 98, 123-170. [5] Johnson G. P. and Talbot R. J. (1964) Air Force Institute of Technology, Dayton, Ohio. [6] Sagy A. et al. (2002) *Nature*, 418, 310-313. [7] Baratoux D. and Melosh H. J. (2003) *EPSL*, 216, 43-54. [8] Gash P. J. S. (1971) *Nature Phys. Sci.*, 230, 32-35. [9] Bray J. G. (1966) *J. Geol.*, 74, 243-245. [10] Dressler B. O. (1984) *The Geology and Ore Deposits of the Sudbury Structure*, 99-136. [11] Ames D. E. et al. (2008) *Econ. Geol.*, 103, 1057-1077. [12] Osinski G. R. et al. (2013) *LMI V*, Abstract #3061. [13] Osinski G. R. and Spray J. G. (2006) *ESA Sp. Pub. SP-612 (CD-ROM)*. [14] Weiland F. et al. (2006) *MAPS*, 41, 1737-1759. [15] Hurwitz D. et al. (2013) *LMI V*, Abstract #3111.

COMPLEX CRATER COLLAPSE: A COMPARISON OF THE BLOCK AND MELOSH MODELS OF ACOUSTIC FLUIDIZATION. H. C. F. C. Hay¹, G. S. Collins² and T. M. Davison², ¹Dept. Earth Science and Engineering, Imperial College London, SW7 2AZ, UK (hamish.hay10@imperial.ac.uk); ²Impacts and Astromaterials Research Centre, Dept. Earth Science and Engineering, Imperial College London, SW7 2AZ, UK.

Introduction: During the collapse of large impact craters the target rock temporarily undergoes an extraordinary drop in yield strength relative to static rock strength measurements, which leads to the formation of a collapsed rim and a central peak/peak ring in complex craters [e.g., 1]. While current numerical models of crater collapse reproduce the broad-scale morphology of complex craters, most models fail to accurately replicate the discrete, localized deformation inherent in the formation of these features [1].

Several physical explanations for the inferred dynamic weakening in impacts have been proposed [1], including acoustic fluidization [2]. Developed by Jay Melosh in 1979, this model proposes dynamic weakening of rock by the action of acoustic vibrations. These vibrations cause pressure fluctuations above and below the ambient overburden pressure. When the pressure is reduced, a temporary weakening occurs. Averaging the effect of pressure fluctuations over time and space, these vibrations cause the rock material to behave as a viscous fluid [2], with an effective viscosity that decreases with increasing vibrational energy.

Collins and Melosh [3] applied the Melosh model of acoustic fluidization in numerical simulations of large rock avalanches. Despite the success of their model, there has been little attempt to implement the full Melosh model into crater collapse simulations.

The block oscillation model [4] is a well-known variation of the Melosh model, with a similar physical premise. It is widely used in impact simulations [e.g. 5]. The block model and the Melosh model predict similar rheological behavior for acoustically fluidized debris [7]. Here we present a comparison between the block and Melosh models for a suite of hydrocode simulations of crater formation at different scales.

Acoustic Fluidization: In the Melosh model, the evolution and generation of acoustic energy (per unit volume), E , is described via a non-linear, ordinary differential equation:

$$\frac{dE}{dt} = \frac{\xi}{4} \nabla^2 E - \frac{c_p}{\lambda Q} E + e \tau_{ij} \dot{\epsilon}_{ij}. \quad (1)$$

The derivative on the left-hand side is the Lagrangian derivative. The first term on the right-hand side is the scattering term, where ξ is the scattering diffusivity with units of a length times a velocity [6]. It contains the Laplacian operator and thus acts to diffuse acoustic energy. The second term on the right-hand side de-

scribes the dissipation of acoustic energy into heat, and is governed by the wavelength of acoustic vibrations, λ , the quality factor, Q , and the compressional wave speed of the rock mass, c_p . The product λQ is especially important in determining the rate at which acoustic energy is dissipated and converted to heat. Generation of acoustic energy is governed by the last term on the right-hand side. The regeneration efficiency parameter, e , which holds a value between unity and zero, dictates how much distortional energy per unit time ($\tau_{ij} \dot{\epsilon}_{ij}$) in the shearing rock mass is converted into new acoustic energy. It is this (re)generation term that converts shockwave energy into acoustic energy and that may facilitate localized dynamic weakening in the latter stages of crater formation.

The block model (as implemented in iSALE) effectively solves the acoustic energy evolution equation (1) with $\xi = 0$ and $e = 0$, and so does not permit regeneration of acoustic energy (localized or otherwise). In this case, the initial acoustic energy field is calculated from the peak particle velocity in the shock wave and its subsequent evolution is dictated entirely by the dissipation term in Eq. 1.

Method: The Melosh model was successfully implemented into the iSALE hydrocode [8,9] by incorporating Eq. (1) into the time loop and by adding an additional strength model, as described in [2], [3] and [6].

To compare the block and Melosh models of acoustic fluidization, a suite of impact scenarios were performed with different impactor sizes (144 m; 1.44 km and 14.4 km), but with the same impactor and target material (granite), impact velocity (12 km/s) and target gravity (9.81 m/s²). An ANEOS-derived equation of state table and standard rock strength parameters for granite [8] were used in all simulations. The block model simulations used typical parameters from recent work [e.g., 5]. In the Melosh model the vibrational wavelength λ was assumed to be a constant fraction of the impactor radius, a , which varied between $0.2a$ and $0.05a$. This assumption is also used in the iSALE implementation of the block model as block size is assumed to be proportional to impactor size. A small value of λ (or block size) leads to both a lower viscosity of fluidized debris and a larger dissipation term, and thus acoustic energy is dissipated more quickly for a small impactor. Q was varied from 10 – 400, in accordance with the values suggested by [3] and [7]. The regeneration efficiency parameter e was

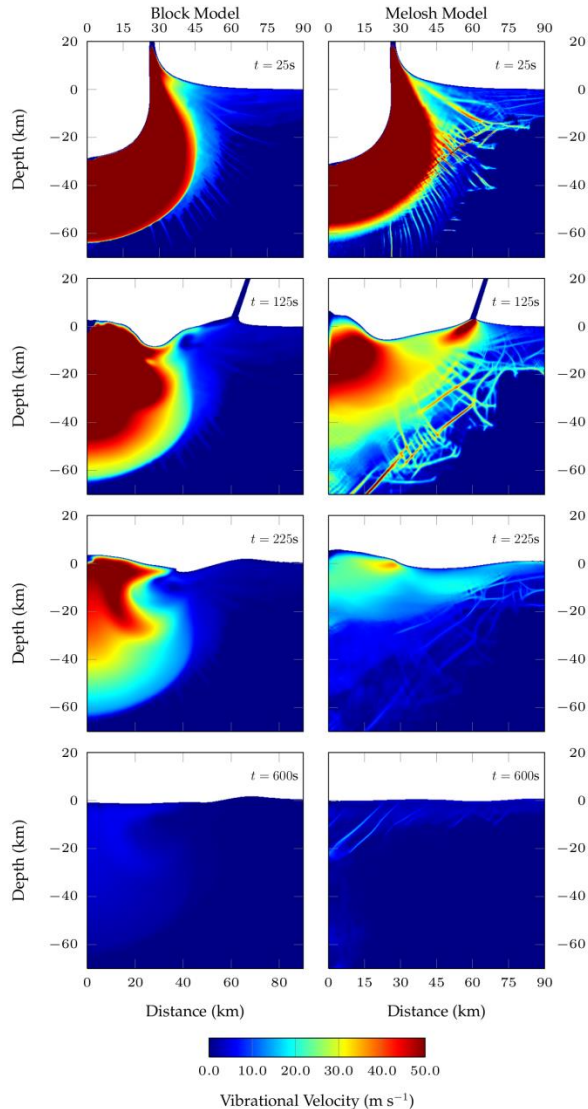


Figure 1 Comparison of vibrational velocity for the Melosh [2] and block [4] models for a 14.4km diameter projectile. $\lambda = 1400\text{m}$ and $Q = 10$ for the Melosh model. Regeneration and localization of acoustic vibrations is evident in the Melosh model, while the longevity of vibrations is greater in the block model to produce qualitatively the same crater morphology.

maintained at 0.1, while the scattering diffusivity, ξ , was kept constant at $10^3 \text{ m}^2/\text{s}$, based on values used in the study of large rock avalanches [3].

Model Comparison: Figure 1 shows the evolution of the vibrational velocity field, v_{vib} (the square-root of the specific acoustic energy), in the largest impact scenario ($\sim 14 \text{ km}$ impactor) for the block model (left) and the Melosh model for an example set of model parameters that results in a similar crater morphology (right).

The first time slice is during the excavation stage of crater formation. The broad, spatial characteristics of the acoustic vibration field between the two models at

this point are relatively similar. Both show a deep zone of intense vibrations ($v_{vib} > 50 \text{ m/s}$). The striking difference, however, is the regions of highly localized vibrations exhibited by the Melosh model.

The second and third time slices show two stages of crater modification. During this time there are important differences between the two models. In the block model, as the vibrations decay, the zone of intense vibrations shrinks in size, particularly in the lateral direction. Complete collapse of the crater requires long-lived vibrations, which are only present in the crater centre. No localization of vibrational energy is observed. In this model, peak-ring formation results as the outwardly collapsing central uplift over-thrusts onto the top of the collapsed crater rim.

In contrast, the Melosh model parameters in the simulation depicted in Fig. 1 result in more rapid dissipation of the initial acoustic energy. In this case, complete collapse of the crater is facilitated by the regeneration of acoustic energy, which prolongs collapse at shallow depths and is more pronounced in both the crater centre and the rim area, as well as along localized zones. Hence, deformation of the target rocks in the Melosh model tends to be more localized and confined to shallower depths than that predicted by the block model. In the Melosh model, peak-ring formation results from the collision of the inwardly collapsing rim and the outwardly collapsing central uplift.

After 600s, the final (peak-ring) crater is formed, and almost all vibrations have ceased in both models.

Conclusions: We have successfully implemented the Melosh model of acoustic fluidization [2] in the iSALE hydrocode and compared its predictions with those of the widely-used block model [4]. For impact simulations that result in qualitatively the same final crater morphology the Melosh model predicts shallower, more localized deformation and a subtly different mode of peak-ring formation.

Acknowledgements: We gratefully acknowledge the developers of iSALE (www.isale-code.de). GSC acknowledges funding from STFC grant: ST/J001260/1.

References: [1] Kenkmann T, Collins GS, Wünnemann K. (2012) In: *Impact cratering: processes and products*. Ozinski GR, Pierazzo E (Eds.), Wiley-Blackwell. [2] Melosh HJ (1979) *J. Geophys. Res.* 84, 7513–7520. [3] Collins GS, Melosh HJ (2003) *J. Geophys. Res.* 108, 2473. [4] Ivanov BA, Kostuchenko VN (1997) *LPS XXVIII*, Abstract #631. [5] Wünnemann K, Ivanov BA (2006) *Solar System Research* 51, 831–845; [6] Melosh HJ, (1996) *Nature*. 379, 601–606. [7] Melosh HJ, Ivanov BA (1999) *Annual Review of Earth and Planetary Sciences*. 27, 385–415. [8] Collins GS, Melosh HJ, Ivanov BA (2004) *Meteoritics Planet. Sci.* 39: 217–231; [9] Wünnemann K, Collins GS, Melosh HJ (2006) *Icarus* 180 (2), 514–527.

GULLIES ON MARS: FLUVIAL GEOLOGIC PROCESSES AS EVIDENCE FOR LIQUID WATER ON MARS. D.J. Hernandez^{1,2}, V. C. Gulick^{1,3} and C. A. Narlesky^{1,4}, ¹NASA-Ames Research Center, MS 239-20, Moffett Field, CA 94035, USA. ²Department of Geologic Sciences, California State Polytechnic University, Pomona, CA 91768, USA, djhernandez@csupomona.edu. ³SETI Institute, Mountain View, CA 94043, USA, virginia.c.gulick@nasa.gov. ⁴MBK Engineers, Sacramento, CA 95815, USA, narlesky@mbkengineers.com.

Introduction: The Mars Reconnaissance Orbiter HiRISE camera has provided unprecedented high-resolution (up to ~25m/px) views of the surface of Mars. These images provide additional insight into the the more recent geologic activities of Mars.

In this study, we used a HiRISE DTM (PSP_006261_1410) to analyze gully morphology and morphometry in Corozal Crater. Gullies are located on X and Y facing slopes, and exhibit morphologic characteristics similar to those of terrestrial gullies formed by fluvial processes including x,y, and z. Using longitudinal and cross-sectional profiles of 12 gullies within Corozal crater, we determined the eroded gully volumes, slopes, and several morphometric indices such as channel concavity, and sinuosity of individual gullies. Our preliminary finding suggest that sediment from crater walls are transported into gully aprons due to fluvial activity on the subsurface of Mars.

Morphology: Gullies are defined as deep channels that cut through the bed rock and normally eroded by water. These geologic formations serve as drainage ways for water as well as a transport method for sediment. Gullies eroded into underlying bed rock exhibit fluvial bedform characteristics as seen in terrestrial gully systems [1].

Steep hills such as valley walls, central peaks and pits, dune fields, and crater walls provide a terrain in which the development of gullies can be studied. Alcoves are formed with a 20°-25° angled slope, channels are formed with a 10°-20° slope, and the debris fans normally exhibit an angle of less than 10° slope [4]. Although gullies are more common in the Southern Hemisphere, they are located in both Hemispheres of Mars. The vast majority of gullies are located between 30° and 50° latitudes in both hemispheres [5]. The gullies are generally located on pole facing slopes, although gullies are also present on some equatorward, western and eastern facing slopes and are rare in equatorial regions.

Methodology: Many gullies exhibit similar trends in terrestrial examples such as discharge volume, stream concavity index numbers, as well as sinuosity values. Therefore, many different craters on Mars will be studied using similar methodologies and calculations of alcove, apron, and stream volumes. Gullies located on different geologic formations, varying locations within the southern and northern hemispheres, as well as research on specific locations throughout dif-

ferent time frames will be studied to find evidence for water as the main source of sediment transport and surface erosion.

Longitudinal profiles through the center stream lines of 12 individual gullies in Corozal Crater were determined using HiRISE stereo images. The center stream line data was then transferred to the the HiRISE DTM using the software package ENVI [6] to accurately extract the elevation and profile of the eroded gully on the crater wall. Perpendicular transect lines (cross-sections) were then created from the starting position at the terminus of the gully from right to left, working up along the channel, ending at the head of the alcove [4].

Computer scripts were developed to determine the eroded volume of the gully drainages. Transect lines spaced twenty meters apart were used to determine the cross-sectional areas that were integrated along the longitudinal profile to determine the volume. Comparing the volumes of the gully alcove, and channel with the volume of the debris apron can yield an estimate on the likely water volume that may have been required to form the gully [3]. As the concavity along the stream profile can also be seen a direct correlation for water erosion; the more concave, the more erosion the stream has experienced.

As an additional parameter, sinuosity was calculated. Sinuosity of different gullies helps compare the meandering tendencies and their depositional volumes of sediment. Sinuosity, or the ratio of the valley stream length over the channel length valley can show the trends of erosion along the channel walls [1]. We can then relate the higher sinuosity index value to the volume that is deposited at the curving banks as sediment deposit, versus the amount of sediment accumulated at the debris fan.

Results: While gathering the data for the slope in comparison to its location (clockwise from the Northern position of Corozal Crater) no significant difference was seen in the slope of individual gullies. The average slope of the twelve gullies studied was 19°, with a minimum slope of 14°, and a maximum slope of 21° (Figure 2). These slopes fall within the range where fluvial processes would likely be more important than purely dry gravitational flows alone [6].

Initial analysis of the resulting graphs seemed to show no overlying trend between the different gullies concerning their volume discharge or their stream con-

cavity index (SCI) individually (Figure 3). However, there was a common trend as noted by a sort of sinusoidal wave of the volume versus the location on the crater and the SCI versus location. This shows a direct correlation between the volume discharge versus and how it is ultimately impacted by its stream concavity index.

Future Work: Further data gathering such as sediment deposits in the debris aprons is needed to calculate sediment transport volumes. This will showcase a mathematical approach by calculating the amount of sediment eroded from the gully itself, and the amount of sediment that has been deposited in the form of a debris fan at the end of its respective gully. Other future data analysis would compare the stream concavity index and the gully's relative age. Through the geologic law of superposition, we can examine the different gullies and their debris flows in accordance to one another to relatively age the gullies by the overlapping apron fans. The age information can then be compared to the SCI and analysis can be made whether older gullies indeed have a higher SCI as compared to the relatively younger gullies.

These principles of methodology will also be applied to future analysis of crater with varying parameters. Gullies located on different geologic features i.e. dunes, or valley walls, as well as the gully locations can use the same parameters for future planetary fluvial processes. Future analysis may also include studying the same locations through different Mars Reconnaissance Orbiter, HiRISE mission fly bys to examine the creation of new gullies, study the history of past gullies, and overall look at the geology in and around the area that can help us prove that water has indeed been the principle form of transportation for this sediment.

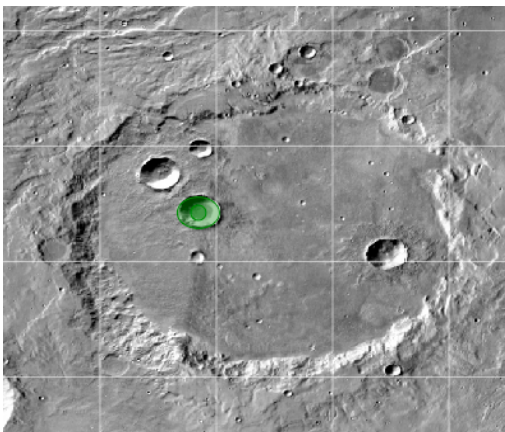
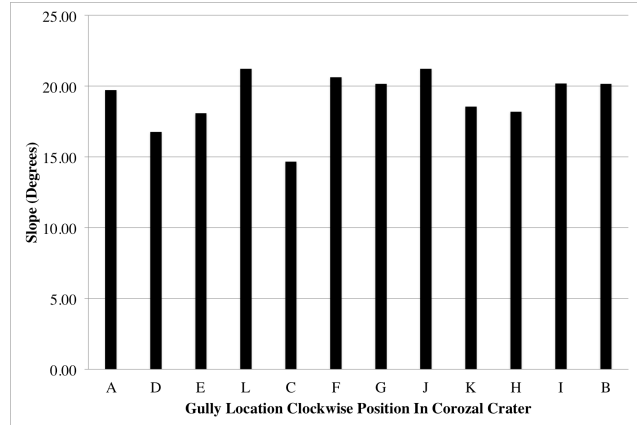


Figure 1 Corozal Crater Longitude: 159.4°, Latitude: -38.7°, Left Observation: PSP_006261_1410 Right Observation: ESP_014093_1410, North Azimuth: 270°, Diameter: 8.33 km

References:

[1] Kirkby, M. J., and L. J. Bracken. (2009) *Earth Surface Processes and Landforms* 34.14: 1841-851. [2] Mangold, N., A. et al. (2010) *JGR-Planets* 115.E11 [3] Gulick, Virginia C., and Victor R. Baker. (1990) *JGR-Planets*, 14th. 95.B9: 325-44 [4] Shepherd, R. G. (1985) *The Journal of Geology* 93.3: 377-84. [5] Ritter, Dale F. *Process Geomorphology*. Dubuque, IA: W.C. Brown, 1978. [6] *ENVI*. Boulder, CO: Research Systems, Inc., 2005. Computer software.



be a control factor for the tested parameters.

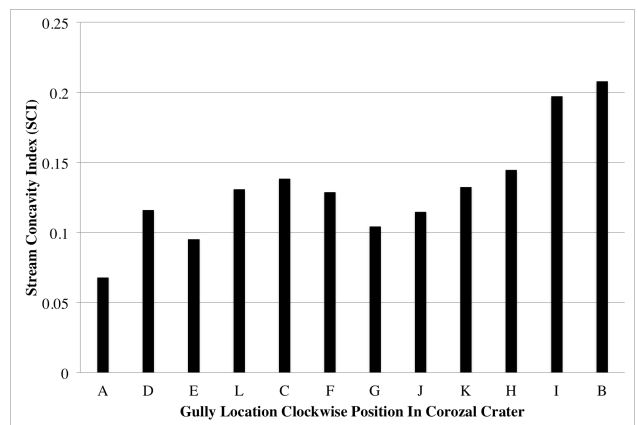
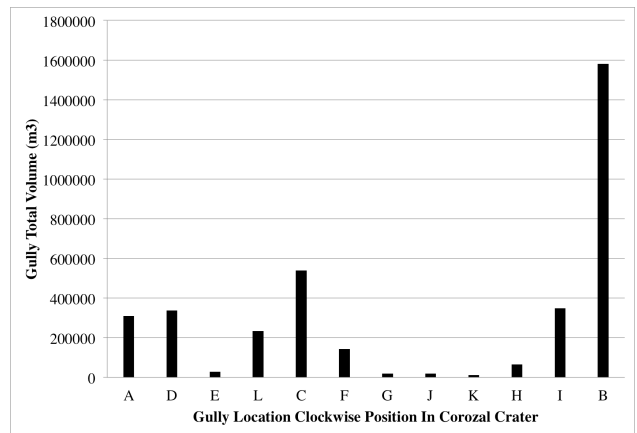


Figure 3 and 4 Volume discharge of the gullies versus location and SCI versus location in the crater gullies. Data is based off perpendicular transect lines of the longitudinal profile of each gully. Both graphs represent a clear relationship between eroded volume and SCI.

GEOMORPHOLOGICAL FEATURES INDICATIVE OF UPWELLING GROUNDWATER ON MARS.

J. A. Hernandez¹. ¹Chairman ERA Foundation (geo.jorge.hernandez@gmail.com)

Abstract: One of the most important aspects in exploring the surface of Mars, mainly for astrobiology, is to determine the current presence of liquid water on the planet.

Extreme weather conditions prevailing, such as an atmospheric pressure lower than 1% of that prevailing at sea level on Earth, and a temperature below 0 ° C, reaching extremes of -140 ° C in the polar caps, are well known by planetary scientists. Given these conditions, are widely discussed the possibilities that liquid water exists in the Martian surface.

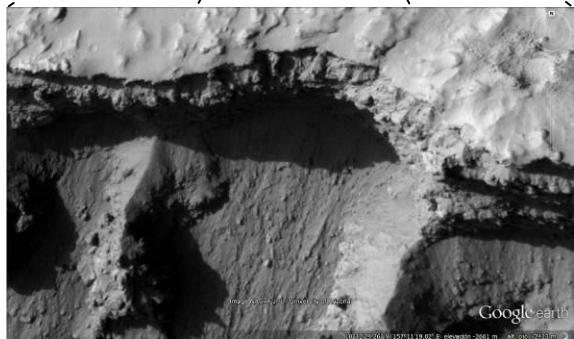
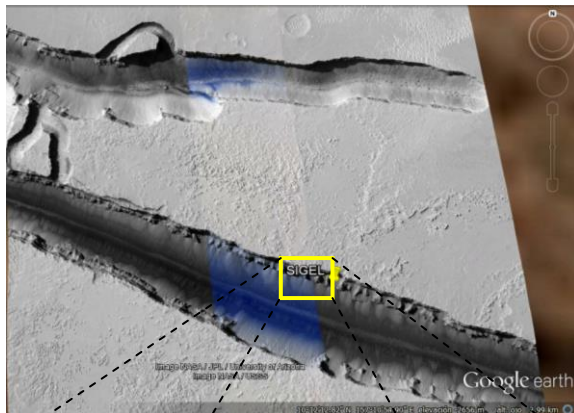
Nevertheless, there is evidence of typical geomorphological features that indicates surface water flows on slopes, observed in different parts of the Mars surface, which increases its length during the warm seasons. Different authors have described these features in the equatorial latitudes of Mars, in places such as Valles Marineris.

In this research, strong geomorphological evidences of groundwater outcrops on the Martian surface, seen in various photographs of the High Resolution Imaging Science Experiment - HiRISE (University of Arizona), are reported in the middle section of Cerberus Fossae, and the top Athabasca Valles.

They are semi parallel and dendritic grooves with a width ranging from a few inches to ten feet wide, elaborated by liquid water in the Martian soil, and originated at the base of downward sloping sedimentary slopes, clearly showing the emanation of groundwater from aquifers. These features do not have widespread occurrence in Cerberus Fossae and are mainly seen in the slopes of the canyon, which have an orientation to the south of the planet and are not repeated in the opposite walls of the fossae, where conical colluvial deposits are found.

This evidence, coincide with the site of generation of aqueous flows reported in Cerberus Fossae, by Devon M. Burr and Alfred S. McEwen of the University of Tucson, Arizona.

References: [1] Burr D. M., McEwen A. S. and Sakimoto S.E.H. (2002) *Geophysical Research Letters*, vol. 29, N° 1. [2] Edgett K. S. and J.R. Rice Jr., (1995). Very young volcanic, lacustrine and fluvial features of the Cerberus and Elysium Basin Region, Mars: Where to send the 1999 Mars Surveyor Lander. *Abstract Lunar Planet. Sci. Conf.*, 26th. [3] Mouginis-Mark P. J., (1990) Recent water release in the Tharsis region of Mars, *Icarus* 84, 362–372. [4] Stack, K. M., Grotzinger, J. P., Milliken, R. E. Bed thickness distributions on Mars: An orbital perspective. *Journal of Geophysical Research (Planets)* 118 2013JGRE..118.1323S 2013. [5] Dundas, C. M., Diniega, S., Hansen, C. J., Byrne, S., McEwen, A. S. Seasonal activity and morphological changes in martian gullies, *Icarus* 220 2012 Icar..220..124D 2012. [6] McEwen A. S et al. Recurring Slope Lineae in Equatorial Regions of Mars. *Nature Geoscience* 7, 53–58 (2014)



SPECTRAL AND MORPHOLOGIC MAPPING OF THE ELORZA CRATER, MARS. R. Hopkins^{1,2}, L. L. Tornabene¹, G. R. Osinski¹ and A. S. McEwen³ ¹Dept. of Earth Sciences & Centre for Planetary Science and Exploration, University of Western Ontario, London, ON, N6A 5B7, Canada (hopkinrt@mcmaster.ca), ²McMaster University, Hamilton, ON, L8S 4L8, Canada, ³Lunar and Planetary Laboratory, University of Arizona, Tucson, AZ 85721, USA.

Introduction: Impact craters uplift and expose rocks from depth, especially within the central uplift of complex craters, providing insights into the stratigraphy of planetary crusts. Moreover, the energy released during the cratering event, particularly into volatile-rich targets, such as the Martian crust, facilitates the formation of a hydrothermal system and may have provided a habitable zone on early Mars [1]. The rocks of a central uplift may thus undergo alteration due to the presence of these hydrothermal systems. However, if alteration products are present in a central uplift, determining the origin of this alteration is a difficult task [1-2].

By using a data synthesis approach, such as merging high spatial and spectral resolution visible images and spectral data, some constraints can be made regarding the origin of rocks found in central uplifts. Here we examine the central uplift of Elorza Crater, a ~40 km diameter crater located at 304.8°E, 8.76°N just north of Valles Marineris and ~300 km north of Coprates Chasma.

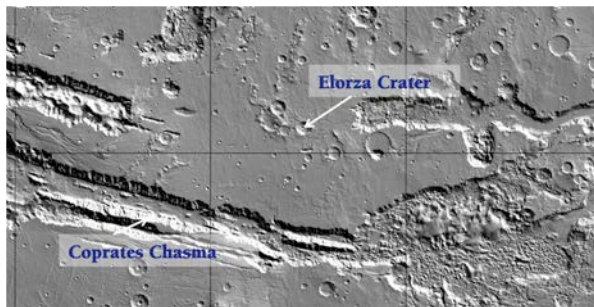


Figure 1: Regional context map of the Elorza Crater with respect to Valles-Marineris. Elorza is a 40.8km diameter crater located approximately 300km north of Coprates Chasma (MOLA, NASA).

Background: Flauhaut et al. [3] constructed a stratigraphic section for the Martian crust based on their observations and interpretations of CRISM data situated on the valley walls of Coprates Chasma. The valley walls of Coprates Chasma consist of light toned-

fractured bedrock rich in low-calcium pyroxene (LCP), at a depth of ~2000 m. Thin, olivine-bearing layers may overlay some of the light-toned bedrock. From ~2000 to 400 m, boulders and talus slope containing

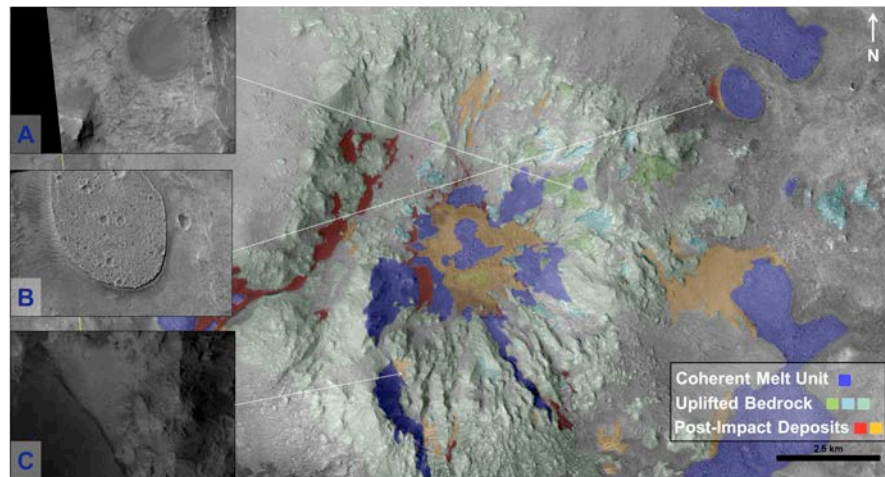


Figure 2: Morphologic map of the central uplift (a peak-pit) of Elorza Crater. A; HiRISE image of uplifted bedrock (light grey) containing Fe/Mg smectites. B; coherent unit outside of the central uplift, interpreted to be melt rock. C; unit containing opaline silica (light grey) adjacent to coherent dark-toned unit.

phyllosilicates are present. Overlaying these layers are Hesperian and Noachian lava flows. Comparing this stratigraphy with the spectral units observed in Elorza, we can further understand which rocks in the central uplift have been excavated from depth, and which have been altered due to hydrothermal systems. Previous studies by Quantin et al. [4] have confirmed the existence of low-calcium pyroxene (LCP), Fe/Mg smectites, and opaline silica in the central uplift of Elorza. Their study placed emphasis on a regional inventory of central uplifts surrounding Valles Marineris and did not provide much detail on the relationship of Elorza's spectral units with its morphologic units. Here we provide a more thorough analysis of the relationship between the occurrence of spectral units, their high-resolution morphology and stratigraphic relationships within the crater setting.

Data: The Compact Reconnaissance Imaging Spectrometer for Mars (CRISM), capable of collecting 18-36 m/pixel images of 544 bands in the 0.4-3.9 μm range [5], and is used here to identify spectral units associated with Elorza's central uplift. The High Resolution Imaging Science Experiment (HiRISE), a ~30-cm/pixel visible camera [6], is used to morphologically map these special units in meter- to decameter scale detail.

Methods: Calibrated Targeted Reduced Data Record (TRDR) v3 CRISM images were processed and analyzed using the CRISM Analysis Tools (CAT) in (ENVI) [7-8]. Spectral parameter maps were generated for common absorptions features attributed to general mineral phases [9].

Regions of interest (ROIs) were chosen using a variety of techniques, such as defining band thresholds on parameter maps, and intersecting these ROIs with ROIs outlining individual morphologic units. Averaged spectra were extracted using both these ROIs and multi-pixel average windows. Spectra were ratioed with respect to a spectrally bland area to accentuate distinguishing spectral features [9]. Ratioed spectra were compared with spectral libraries (USGS, CRISM) to determine the possible mineralogical phases present within the central uplift. Spectral units were then precisely overlain and compared with HiRISE images and Digital Terrain Models (DTMs) to determine the morphological and stratigraphic relationships of spectral units [10]. A morphologic map (Figure 2) was created in JMARS (Java Mission-planning and Analysis for Remote Sensing) using HiRISE and other relevant data sets.

Results: Opaline silica is observed in multiple locations on the southwestern side of the uplift, consistent with previous studies [4]. The unit appears to be overlain by coherent impact melt rock (Figure 2c) that looks to be eroding away, exposing the underlying bedrock. This is most consistent a pre-impact origin for the opaline silica bearing rock (Figure 3c), which is supported by the extensive surface exposure of these materials around Valles Marineris [11].

A mixture of low-calcium pyroxene (LCP) and high-calcium pyroxene (HCP) is observed in several units throughout the central uplift. Although indications of HCP are not found in the local stratigraphy [3], it's presence could be the result of a heterogeneity within the local target rocks (Figure 3b). Fe/Mg smectites are found throughout the central uplift, in agreement with previous work [4]. The smectites are found in several lightly fractured, uplifted bedrock units, found mostly on the eastern portion of the central uplift (Figure 3a).

Future work: Further analysis is necessary to be able to confidently determine which rocks existed pre-impact, were altered during the impact process, or were deposited after impact. In many cases, rocks may originate within a crater in more than one way, making this task all the more difficult.

In order to develop a better understanding of the impact processes, additional craters should be analyzed in a similar manner. Once general trends are observed in a variety of craters, distinguishing the origin of their altered material should be a much easier task.

Understanding how rocks originate in a central uplift is a vital research topic. Altered rocks on Mars provide a glimpse into Martian water history, and impact hydrothermal systems may have provided habitable zones during Mars' early history.

References: [1] Osinski et al. (2012), *Icarus*; [2] Tornabene et al. (2013), *J Geophys Res*; [3] Flahaut et al. (2012), *Icarus*; [4] Quantin et al. (2012), *Icarus*; [5] Murchie et al. (2007), *J Geophys Res*; [6] McEwen et al. (2007), *J Geophys Res*; [7] McGuire et al. (2009), *Planet Space Sci*; [8] Parente (2008), *P Lunar Planet Sci*; [9] Murchie et al. (2009), *J Geophys Res*; [10] Delamere et al. (2010), *Icarus*; [11] Milliken et al. (2008), *Geology*.

Acknowledgements: The lead author acknowledges funding from NSERC, CSA, and MDA through the Industrial Research Chair in Planetary Geology, Dr. Gordon R. Osinski.

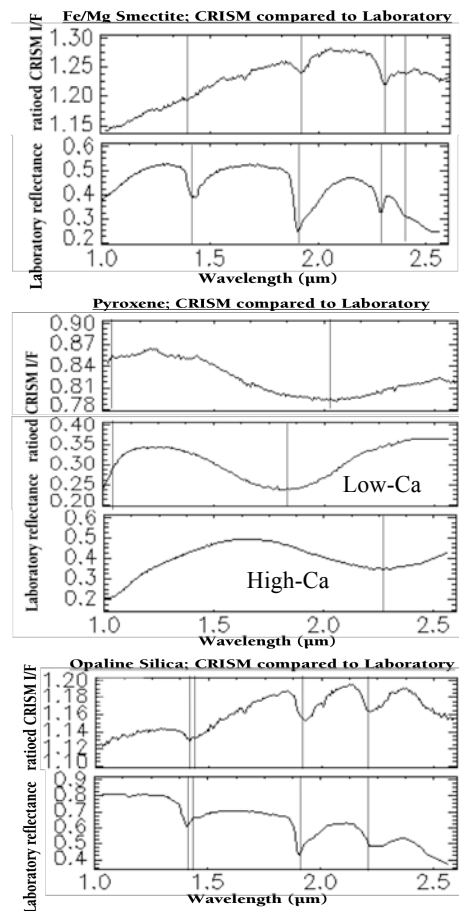


Figure 3: Comparison of several CRISM spectra with lab spectra. A; Fe/Mg Smectite from 2A (top), Nontron2 (bottom). Absorptions at 1.39, 1.92, 2.29, 2.39µm. B; Mixture of high-calcium and low-calcium pyroxene (CRISM, top), hypersthene (middle) a low-calcium pyroxene, and augite (bottom) a high-calcium pyroxene. In the CRISM spectra, shifted absorption band caused by a mix of different pyroxenes. 1.0µm absorption only partially shown. C; opaline silicate from 2C (top), Opal TM8895- hyalite (bottom). Absorptions at 1.39, 1.41, 1.92, 2.21µm. All lab spectra from the USGS mineral library in ENVI.

USING POROUS MATERIAL TO SIMULATE ASTEROID DISRUPTION. S. J. Jack¹, M. M. Strait¹, G. J. Flynn², and D. D. Durda³ ¹Dept. Of Chemistry, Alma College, 614 W. Superior St., Alma MI 48801 (jack1sj@alma.edu), ²Dept. Of Physics, State University of New York-Plattsburgh, Plattsburgh NY 12901, ³Southwest Research Institute, 1050 Walnut Street Suite 3400, Boulder CO 80302.

Introduction: In space, asteroids are constantly colliding and disrupting, forming meteorites. Some of these are on a route to Earth. A way to change this route is needed in order to reduce the damage done to the Earth. By studying the disruption of meteorites, an idea of how to deflect them, either by disrupting them more or redirecting the route, can be established [1].

We have been studying materials of different compositions to investigate differences in disruption patterns at the NASA Ames Vertical Gun Range for a number of years. We have found that different materials disrupt in different ways [2].

Meteorites are made of many different materials and it is difficult to replicate these compositions and disrupting actual meteorites is not always an option due to their rarity. We have been using terrestrial analogs to study physical properties of rocks and in this study the characteristic being investigated is the porosity of the rock [3]. One physical characteristic of asteroids seems to be a high porosity, so we are investigating the disruption characteristics of a high porosity material. A good terrestrial test rock for porosity is pumice—it is inexpensive and easy to acquire. The pumice is disrupted and the distribution of particles is analyzed to help further the understanding of meteorite impacts [4, 5].

Experimental Details: Disruption of the samples takes place at the NASA Ames Vertical Gun Range in California. In the gun chamber, foils of various thicknesses are placed around the rock suspended in the center (Figure 1). The rock is impacted with an eighth- or quarter-inch aluminum sphere with speeds of about 5 km/sec—the speed of material in space. This disrupts the rock and causes particles to fly and pierce the surrounding foils. A sheet also covers the floor so all of the particles can be collected for analysis.

In the lab, the foils are mounted onto slides and scanned into a computer using a Prime Film 7250 Pro³ scanner and Cyber View X. The image is then analyzed in ImageJ where all the holes are counted and measured. The particles from the floor are put through an eight-level sieve to sort them by size. All the particles in the > 4.00 mm range and > 2.00 mm range are massed, ten to twenty particles are massed in the >1.00 mm range and > 0.5 mm range. In the last four levels all the particles of the same size range are massed together. Both sets of data are imported into an Excel[®] spreadsheet and a graph is produced.

Results: There are two distinct types of graph produced. One has a smooth “S” shaped curve—high on the left, flat in the middle and, low on the right. This is customary of a typical meteorite disruption (Figure 2). The second graph has the same “S” shape but with a gap in the flat area (Figure 3). This means there were no particles of that size formed in the disruption.

In previous shots of low porosity material, the rock completely shattered resulting in a continuous particle distribution between 7.1×10^{-14} g and 0.03 g. In the pumice shots, the rock would either break into several large pieces or form a crater with no disruption. This resulted in particles between 0.0001 g and 100 g and then dust, as small as 1×10^{-11} g, with a gap between 0.0001 g and 1.0×10^{-9} g. There were a total of twenty shots done on pumice with various masses impacted with various projectile mass and speed. The majority of the graphs produce a gap. This suggests that if an asteroid is made of highly porous material, disrupting it more could cause it to break into large pieces or to crater, not really fixing the problem of asteroids and meteorites crashing into the earth and causing damage.

Future Work: With all of the shot data is analyzed, the velocity of the projectile, mass of the projectile, and mass of the rock will be looked at to see if there is any correlation between them and whether the rock disrupted or cratered. Also the gap size will be looked at and compared to the correlation determined earlier.

Acknowledgements: This work was supported by NASA Planetary Geology and Geophysics Program Project Number NNX11AP22G. Support was also provided by the National Science Foundation via the PRISM grant to Alma College. Additional support is provided by Alma College.

References: [1] Flynn G. J. et al. (2014) *LPS XLV*, Abstract. [2] Flynn G. J. et al. (2009) *Planetary and Space Science*, 57, 119-126. [3] Durda D. D. and Flynn G. J. (1999) *Icarus*, 142, 46-55. [4] Flynn G. J. et al. (1999) *Icarus*, 142, 97-105. [5] Durda D. D. et al. (2005) *Workshop on Dust in Planetary Systems*, 77-80.



Figure 1: The set up inside the gun chamber at the AGVR. The foil detectors are in the upper right. The rock sample is hanging in the lower left. The drapery is the sheet covering the surfaces used to collect the particles.

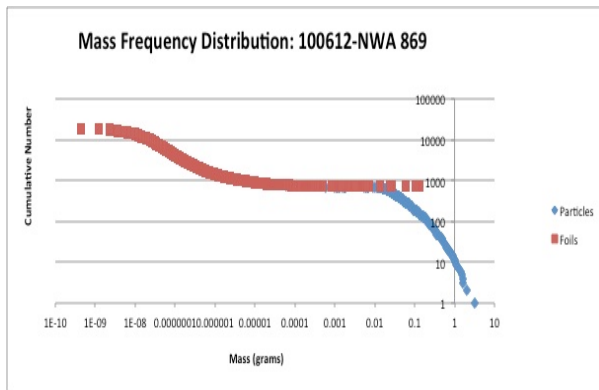


Figure 2: A typical meteorite graph with a smooth curve.

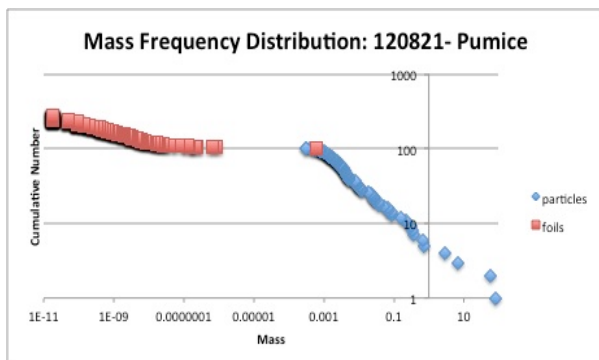


Figure 3: A pumice disruption graph with a gap in the middle. This is characteristic of the pumice disruptions.

OBSERVATIONS ABOUT BOULDERS ON THE SOUTH POLAR TERRAIN OF ENCELADUS. Brent C. Landry¹, Lily C. Munsill¹, Geoffrey C. Collins¹, and Karl L. Mitchell², ¹Wheaton College, 26 E. Main St., Norton, MA 02766, gcollins@wheatoncollege.edu, ²Jet Propulsion Laboratory, California Institute of Technology, Pasadena, CA 91109.

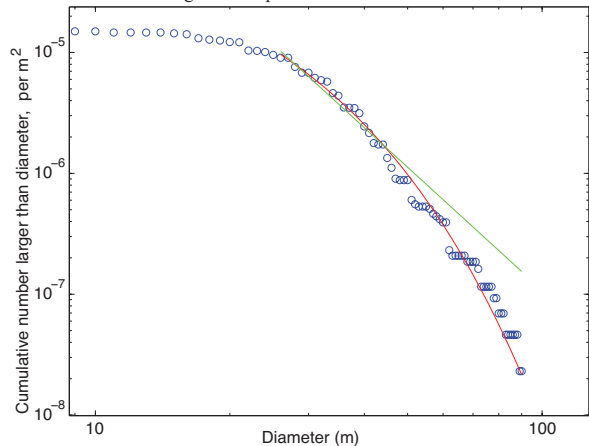
Introduction: The first high resolution images returned from the south polar region of Enceladus showed icy blocks littering the surface [1], and subsequent high resolution imaging has found similar abundances of blocks (“boulders”) within the south polar terrain, but much fewer outside it. Here we examine the size and spatial distribution of distinct, isolated positive relief features that we interpret to be boulders in the south polar terrain. The nature and distribution of boulders has implications for their formation mechanism, for microwave scattering by the regolith, and for landed mission on Enceladus in the future.

Data: Cassini ISS NAC data of Enceladus obtained between 2005 to 2011 was processed using ISIS 3, and navigated for pointing correction with respect to the basemap by Roatsch et al. [2]. High resolution south polar data was selected from the larger data set, and assembled into a reconfigurable mosaic in ArcGIS for terrain mapping. A smaller subset of 19 images listed in Table 1 was used for measuring the properties of the boulders.

Size distribution: The images listed in Table 1 were selected because they clearly displayed fields of positive relief features that we interpret to be boulders. The diameter and position of each boulder within these images was measured using qview in ISIS 3.

#	Image	Res. m/px	Boulders counted	Largest boulder
1	N1500063766	4	189	125 m
2	N1597182401	11.4	974	79 m
3	N1597182434	14.9	740	124 m
4	N1597182467	18.4	839	143 m
5	N1597182500	21.8	487	166 m
6	N1597182533	25.3	651	180 m
7	N1597182568	28.9	257	235 m
8	N1604166937	8.7	656	92 m
9	N1604166970	12.1	882	121 m
10	N1604167003	15.6	680	174 m
11	N1604167036	38.1	89	144 m
12	N1604167059	21.4	545	144 m
13	N1604167092	24.9	180	155 m
14	N1604167125	28.4	96	107 m
15	N1604167158	31.9	812	130 m
16	N1604167191	35.6	1101	133 m
17	N1604167225	39.1	603	152 m
18	N1604167409	58.6	271	182 m
19	N1660432914	19.9	996	79 m

Figure 1: Cumulative size distribution of boulders in image 8 (open circles). Best fit power-law (green line) and exponential function (red line) shown at diameters larger than 3 pixels.



The six images shown in white on Table 1 each contained significant numbers of boulders (>100) viewed at more than 3 pixels across. The boulders more than 3 pixels across in these six images were used to examine size distribution statistics with respect to a power-law distribution $N(D) = K D^c$ and an exponential distribution $N(D) = K e^{(c D)}$ where $N(D)$ is the number of boulders larger than a certain diameter per square meter of surface, D is the diameter, K is a best-fit multiplicative constant and c is a best-fit coefficient in the exponent. Figure 1 shows a plot of the cumulative size distribution of boulders in image 8, compared to best fit equations. Table 2 lists the best fit coefficients c and the correlation r for power-law and exponential distributions in the six target images highlighted in Table 1. Unlike boulders on Eros, which follow a steep -5 power law distribution [3], the best fit power law to Enceladus boulders generally has a slope between -3 and -4. Better statistical fits to the boulder distributions in all images are obtained using an exponential curve, as has been found for boulder fields on Mars and Earth [e.g. 4].

Table 2: Best fits to size distributions, listing best fit coefficients in exponent and correlation coefficient. Only data from diameters > 3 pixels used for fits.

Image	Power law fit		Exponential fit	
	coefficient	r	coefficient	r
1	-1.3	0.936	-0.044	0.985
2	-3.5	0.990	-0.13	0.994
3	-3.6	0.977	-0.090	0.986
8	-3.2	0.990	-0.093	0.996
9	-3.6	0.993	-0.082	0.997
10	-4.0	0.983	-0.076	0.990

Spatial distribution: The images in table 1, along with 13 additional images with resolutions better than 100 m/pixel, were examined in the ArcGIS mosaic. The terrain was classified into rough (high density of ridges), smooth (plateau areas), and another “sulcus” category along the edges of the prominent “tiger stripe” fractures. Within each of these terrain types, example areas were found in the Table 1 images that contained boulders and also areas that did not contain boulders. The morphology of the boulder-containing terrain types were then mapped out into the surrounding images viewed at lower resolution. Figure 2 shows a map of the terrain classified in this high resolution image set, separating areas with observed boulders (or likely to contain boulders by linkage to adjacent high resolution images) from areas with no observed boulders (or unlikely to contain them based on adjacent images). No obvious pattern is found in boulder sizes or areal density with respect to proximity to other prominent terrain features, such as the tiger stripes, but additional tests need to be performed.

Formation hypotheses: Since there are no craters observed in the south polar terrain of Enceladus [1], it is unlikely that boulders are the result of impact cratering processes, a common emplacement mechanism on the Moon or asteroids. Ballistic ejection of the boulders from tiger stripe geysers [5] is on the edge of possibility given certain volcanic conditions, but is unlikely to explain the observed boulder population, as there is no clear preferred distribution of boulders with

respect to the locations of the geysers.

Two hypothetical mechanisms could be tested. In one, the boulder-choked surfaces form as a lag deposit during sublimation or collapse of loose regolith. The south polar terrain has an unusually high heat flow [6], and small particles deposited from the geysers are likely to be poor thermal conductors. The underside of solid ice blocks with exposed tops may thus stay cooler than the surrounding regolith thus preferentially resist sublimation. In an alternative hypothesis, the blocks initially form in the near subsurface by tectonic detachment along intersecting, tidally-worked faults. After detachment, the Brazil nut effect could bring these blocks to the top of a loose regolith layer as the surface of Enceladus is disturbed by seismicity and tides.

Link to microwave observations: Unusually high RADAR backscatter from Cassini has been reported from tectonized areas in the South Polar Terrain of Enceladus [5]. One possible explanation for this behavior is the presence of cm-scale voids within the regolith or quasi-spherical pebble piles on the surface [7], possibly implying that the boulder size distribution extends well below that observed by ISS in the uppermost surfaces of these tectonized terrains. Extrapolation from the best-fit distributions to the boulder observations down to the centimeter scale can help to resolve this issue. Experience with extrapolation of rock populations on Mars has successfully linked orbital observations of large boulders with ground truth about small rocks from landing sites [8].

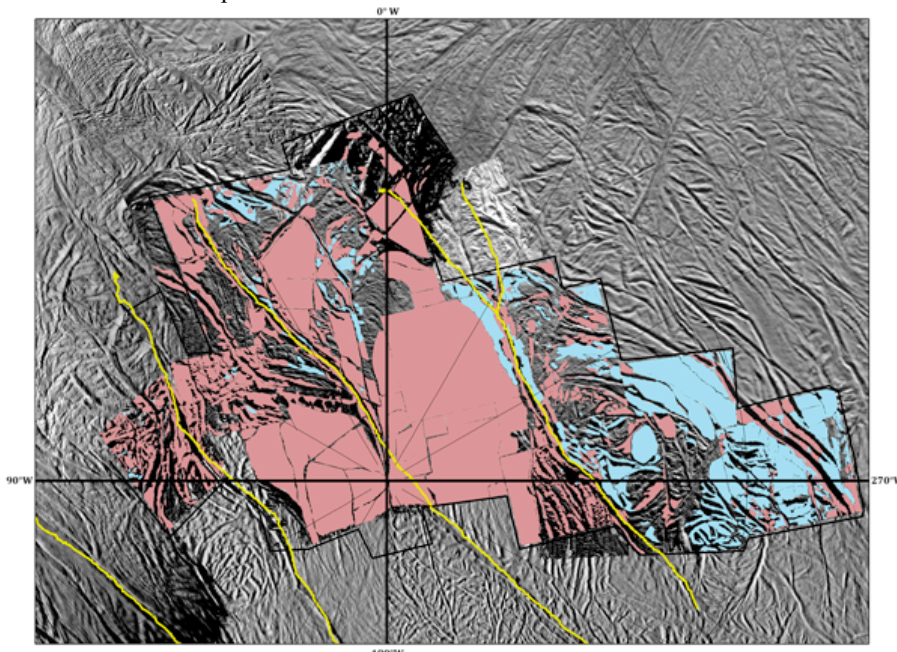


Figure 2: High resolution images near the south pole of Enceladus, classified as either displaying boulders on the surface (pink) or displaying a smooth surface without fields of boulders (blue). Gaps in classification coverage are due to shadows or steep slopes in the highest resolution images. “Tiger stripe” fractures shown in yellow for reference.

- References:** [1] Porco C. et al. (2006) *Science*, 311, 1393-1401. [2] Roatsch Th. et al. (2013) *Planet. Space Sci.*, 77, 118-125. [3] Chapman C. et al. (2002) *Icarus*, 155, 104-118. [4] Golombek M. and Rapp D. (1997) *JGR*, 102, 4117-4129. [5] Mitchell K. et al. (2013) *LPS XLIV*, Abstract #2902. [6] Howett C. et al. (2011) *JGR*, 116, E03003. [7] Khankhoje U. et al. (2013) *LPS XLIV*, Abstract #2531. [8] Golombek M. et al. (2008) *JGR*, 113, E00A09.

Acknowledgements: KLM's contribution was carried out at the California Institute of Technology Jet Propulsion Laboratory under a contract with NASA.

Titanium isotopic compositions in lunar and terrestrial samples: Implications for lunar origin

R. Leverone¹ National High Magnetic Field Laboratory & Dept. of Earth,
Ocean & Atmospheric Science, Florida State University, Tallahassee, FL 32310, USA (rnl12@my.fsu.edu).

Introduction: Recent studies emphasize the similarity in O-, Ti-, and W- isotopic composition between the Moon and Earth [1-3]. This, in turn, has been taken to imply that the Moon must predominantly consist of proto-Earth mantle derived material ejected by a giant impact [2]. Such an assumption contradicts physical evidences, i.e. the angular momentum of both bodies [4]. Most giant impact models found that the proto-Earth derived material can constitute only 50% or less of the subsequently formed moon [5-6]. To accommodate both the angular momentum constraints and the Ti isotopes new models involving evicton resonance or excessive mixing of the proto lunar disc arose, but alone they do not provide a likely solution [7-8]. Various chondrites have revealed different levels of Ti isotopic anomalies. Here, especially carbonaceous chondrites reveal anomalies up to +3.5 ϵu and achondrites down to -1 ϵu [2]. In this study we intend to measure Ti isotope abundances of multiple lunar and terrestrial samples with precisions in the sub- ϵ -level to address the similarity and differences of varied materials. Furthermore, we propose to explore both those lunar outliers in greater depth and additional explanations of Ti isotopic similarities between the Earth and Moon.

Analytical Methodology:

We will provide new titanium isotope data for terrestrial and lunar samples. Preliminary testing of BHVO-2 and SPEX Titanium standards show a working procedure as described below which will be used for sample measurement in the future.

Powdered samples were digested using a heated HF: HNO₃ mixture for 3 days. Then, they are dried and transferred to a 0.5M HCl 0.5M HF solution for cation column separation of the sample matrix, such as Ca, using BioRad™ AG50W-X8 resin, followed by separation of Cr, V, Mo, Zr, which form interferences, with BioRad™ AG1-X8 anion resin. Titanium was eluted on the anion column with 3.6 M HAc+2% H₂O₂+trace HNO₃ following [9]. A 97% recovery of Ti was achieved with no appreciable remainder of possible mass interfering elements (Cr, V, Mo and Zr) using this procedure.

Titanium isotopic compositions were measured on a Neptune™ MC-ICP-MS (at the National High Magnetic Field Laboratory in Tallahassee) in a 1% HCl with trace HF matrix solution. A nitric acid matrix was avoided due to interferences on masses 46 and 47 by

NO₂ and HNO₂, respectively. This modification allowed ⁴⁷Ti to be measured without concern of significant interferences, in low resolution mode. Jet sampler and Ni-X skimmer cones were used for measurement along with a desolvating nebulizer (Apex IR™) at an uptake rate of approximately 125 $\mu\text{l}/\text{min}$. Titanium isotope ratios are reported after mass dependent fractionation correction using an exponential law (⁴⁹Ti/⁴⁷Ti=0.7497 [10]) using ϵ -notation (deviation from the reference in 10,000):

$$\epsilon = \left(\frac{\text{measured } ^{50}\text{Ti}/^{47}\text{Ti}}{\text{reference } ^{50}\text{Ti}/^{47}\text{Ti}} - 1 \right) \times 10,000$$

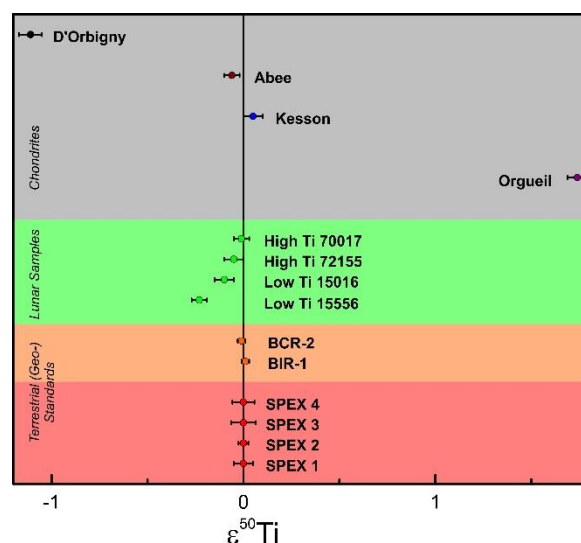


Figure 1: Titanium isotopic compositions of terrestrial geostandards, Lunar basalts, and chondrites. Spex values are daily averages collected over the course of 3 months. Terrestrial geostandard, Lunar basalt, and chondrite values showing nucleosynthetic anomalies are taken from [2]. All errors, are 2SE.

Results and Future Plans:

Measurements of the SPEX Titanium standard provided an external reproducibility for $\epsilon(^{50}\text{Ti}/^{47}\text{Ti})$ of less than 0.05 ϵu (n=14). BHVO-2, BIR-1 and BCR-2 will be used as references for a terrestrial ⁵⁰Ti/⁴⁷Ti value. Three isotope masses, ⁵¹V, ⁵²Cr, and ⁵³Cr are simultaneously measured with the 5 Ti isotopes for monitoring the possible isobaric interferences of Cr and V on the mass 50 and used to correct if necessary. Other probable interferences, Ca, Mo²⁺, Zr²⁺ etc., are checked prior to measurement using an Element-2™ ICP-MS. During the preliminary measurements of the terrestrial reference mate-

rial these (isobaric) interferences were low and negligible. Lunar samples including low-Ti mare basalts, high-Ti mare basalts, highlands breccias, and lunar meteorites will be analyzed for their Ti isotope composition. Lunar samples will likely have cosmic ray damage that may affect Ti isotope abundances. We will recalculate the samples Ti isotopic composition following methods of [2] as needed to account for possible secondary neutron capture.

References:

- [1] Wiechert, U. et al. (2001). *Science* 294, 345_348. [2] Zhang J. et al. (2012), *Nature Geoscience*, 251_255. [3] Touboul M. et al. (2012). *Science*, 335, 1065. [4] Canup, R. M. (2004) *Icarus* 168, 433_456. [5] Reufer, A. et al. (2011) 42nd LPSC. abstr. 1136. [6] Pahlevan, K. & Stevenson D. J. (2007) *EPSL*, 262, 438_449. [7] Cuk M., Stewart S.T (2012) *Sci. Express*. 10.1126/science.1225542 (2012). [8] Dahl, T.W. and Stevenson, D.J. (2010). *EPSL*, 295 (1-2). pp. 177-186. [9] Muenker, C. et al. (2001) *GGG*, 2, 10. 1029/2001GC000183. [10] Niederer F.R. et al. *GCA*, Volume 49, Issue 3, March 1985, 835-85.

SIMPLISTIC MASS-RADIUS RELATIONSHIPS OF EXOPLANETS. A. Lorenzo¹, S. J. Desch¹ and S.-H. Shim¹, ¹School of Earth and Space Exploration, Arizona State University, Tempe, AZ 85287. (Alejandro.Lorenzo@asu.edu).

Background:

The field of exoplanetary studies has been a widening area in the past few decades. It all began with the discovery of 51 Pegasi b in 1995, a Hot Jupiter orbiting a main sequence star. This first example has stirred the scientific community's curiosity since. Not only was it the singular extra-solar planet known to man, it challenged our understanding of planetary dynamics as we knew it. At that point, our understanding of how our own solar system came to be the way it is now was incomplete. The discovery of this massive planet with an orbital period of just $4.23 \pm 5e - 05$ days and a mass of $0.468 \pm 0.007M_J$ [1] had challenged everything we knew about our system.

Today, the archive of confirmed exoplanets has grown from a few massive gaseous planets to over a thousand both gas giants, and rocky planets. There are an estimated 1.6 planets to every star in the milky way alone. Though more difficult to discover, rocky planets have appeared to me more prominent in other systems than gas giant types. With a vast increase in the quality of technology for finding these bodies, there has been a large flux of possible planet candidates. Coming from both ground based operations including the new Gemini planet imager, and Kepler Space telescope observations. With the expected 2017 launch of the Transiting Exoplanet Survey Satellite (TESS), the influx of planet candidates could reach overwhelming proportions.

TESS will be searching for dips in the light curves of nearby G and K type stars. These stars have temperatures and compositions similar to that of the sun. Therefore the habitability zones of these systems should have radii resembling the solar system. Between the 500,000 stars and 1,000 red dwarfs this mission plans to observe, there will be an expected 6,000 new planet candidates over the next two years. Additionally, the famed Kepler space telescope appears to be making a second round of planet hunting following a nearly year long hiatus. These instruments can bring approximate radii measurements while followup observations can use the radial velocity technique or another to discover the mass of this planet. What we have found is radius measurements are less accurate than measurements of mass. This is because when a dip in a light curve of a star is noticed, it accounts for not only the light

blockage of the solid body, but the atmosphere as well. This can, of course, be more evident when a planet has a substantial atmosphere.

Calculating the actual radii of these planets is therefore necessary. Many components need be accounted for in these calculations. This includes, the approximate mass fraction of the planets inner core, outer core, mantle, as well as what materials are found in those sections. It is possible to narrow down the likely elements that that may be found in this part of a system by observing both the host star and the star formation region. Once the base elements have been approximated, one can start to make theoretical models of planets with the chosen composition and observed mass. The plausible mass fraction of each section of a planet and materials may be further condensed due to compressional effects. Dense polymorphs can greatly decrease the calculated radius, especially with particularly massive bodies. These calculations can be tiring and superfluous if the desired outcome is not readily attained.

We have developed a program which performs these calculations and allows for the input of all plausible combinations mentioned. With the simplicity of such a program, confirmed planet candidates can be quickly and easily identified for what they really are inside. This will greatly speed up the process of mapping out our neighbor systems. **The purpose of this abstract is to explain how this program works and what other benefits can come of this in the future as we continue to develop exoplanetary studies.**

Calculation:

Modeling the interior of an extrasolar planet properly demands a series of variables and choosing the right equations of state for each variable. We start by varying the mass fraction of the internal components of a planet: a core and a mantle. The core may be parsed into two parts, the inner core and the outer core. This will account for likely differentiation in bulk composition. There are essentially an infinite amount of combinations that can go into this. Of course, some insight of what elements may have been most likely present in the protoplanetary disk will help to narrow down the potential mass fraction of each section. In addition to this, taking note of the orbital position may be helpful as well.

This can also be deceiving due to gravitational interactions in both the protoplanetary disc and the system over time. Only when considering younger system could this be potentially useful.

Each boundary is given a composition with a zero pressure density ρ_0 that can be used in combination with the mass to derive a volume within the boundaries. The volume is used to calculate a radius that is initially evenly distributed throughout the planet. These radii produce concentric shells with a volume and a static mass. Once compression is accounted for, the mass will remain constant, thus the volume will vary to achieve the desired mass. To calculate compression we first integrate the equation of hydrostatic equilibrium to calculate for the pressure at each shell.

For the density calculation, we have mostly used a third order Birch-Murnaghan equation of state with inputs of pressure at shell boundaries, isothermal bulk modulus $K_{T,0}$, and the pressure derivative of bulk modulus dK_T/dP_0 at zero pressure. We also account for the possibility of alloying elements in the core. In Earths core, these impurities amount to: 6 wt% Si, 3 wt% O, 1 wt% S, and only trace amounts of C and H [7]. In the program, we have allowed of the input of such impurities. For other materials, we draw fits from the literature, notably: ϵ (hcp) Fe [8], B2 phase of FeSi [9], the orthrhombic B8 phase of $\text{Fe}_{0.95}\text{O}$, FeS VII [9]; for the rocky mantle we use the equation of state for MgSiO_3 of [4].

Once the density is found, it is possible to again calculate for the radius of each shell. To completely account for compression this process must iterate several times to convergence. The radius R_p found can now be used in $M - R$ plots to compare with observed exoplanets of similar mass.

For reasonable pressures, we find that the aforementioned fits provide a good approximation for the compressional effects within solid planets. Some extrapolation is required as none of the chosen materials have been observed at pressures achievable in

massive planets however for planets $M_p < 20M_{\oplus}$, the extrapolations operate within a acceptable margin of error.

Applying these calculations in an easy to use program has its advantages. The wide range of planet composition and models allows for varying outputs that all need to be considered. Having the ability to simply choose these parameter will greatly reduce the workload and allow for further precision in the future. In addition to this, we have chosen to develop this program in Java. Java has the advantage of portability to most machines. We intend to make this program widely available to allow for its usability to be maximized.

Conclusions: The tools astronomers have allow them to make astonishing discoveries that would be impossible or at least slow going with the standard approach of pencil and paper or a small telescope on a swivel stand. Discovering extrasolar planets is a demanding task in itself. Sifting through data for a small deviation in the light curve of a star can daunting and time-costly. This is why we intend to make the cataloging of such planets as simple as ever. Using this widely accessible tool that we have developed, matching a confirmed planet with a mass M_p to its proper radius and composition will be a simply task. We have also found that by practicing with the possibilities of planet models and composition, we can discover the extremities of planet radii at a given mass. We hope that in the future programs similar to this one will have the capability to accurately map the systems we discover.

References: [1] E. Simpson et al. 2010, 2010MNRAS.408.1666S. [2] H. Bruntt et al. 2010, A&A 519, A51. [3] N. Batalha et al. 2011, ApJ 729, 27. [4] S. Seager et al. 2007, ApJ 669, 1279. [5] Z. Li & D. Sasselov 2013, PASP 125, 227. [6] R. Marcus et al. 2010, ApJ 712, L73. [7] K. Hirose et al. 2013, AREPS 41, 657. [8] L.S. Dubrovinsky et al. 2000, PRL 84, 1720. [9] N. Sata et al. 2010, JGR 115:B09204.

FIRST REPORT OF SHOCKED ZIRCON AT THE SANTA FE IMPACT STRUCTURE (USA).C. M. Lugo Centeno¹ (cristina.lugo@upr.edu), A.J. Cavosie^{1,2} (aaron.cavosie@upr.edu)¹University of Puerto Rico at Mayagüez, ²University of Wisconsin-Madison

Introduction: The documentation of shocked minerals provides a diagnostic criteria for the identification and confirmation of an impact structure. Studies of detrital shocked minerals in South Africa (Vredefort Dome), and Canada (Sudbury) have demonstrated that they can survive post-impact metamorphism, erosion, and distal sedimentary transport [1-3]. The presence of shatter cones and shocked quartz were used to confirm the Santa Fe impact structure near Santa Fe, New Mexico as having an impact origin [4]. Here we report the first occurrence of shocked zircon at the Santa Fe Impact structure, which were found as detrital grains, rather than in bedrock.

Santa Fe impact structure: The age of impact is poorly constrained, but is believed to have occurred between ~1200 and ~350 Ma [4]. The structure is highly tectonized and deeply eroded; based on shatter cone distribution, the estimated original diameter is from ~6 to 13 km [4].

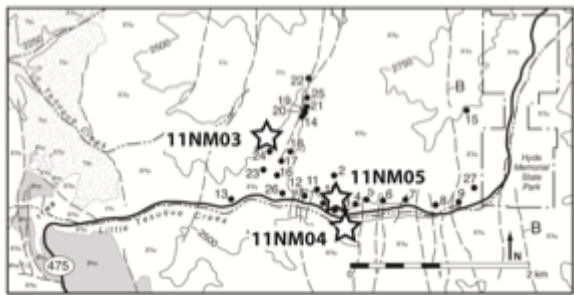


Figure 1. Location of Santa Fe impact structure, after [4]. Stars are locations of sediment samples. Black dots show the location of shatter cones outcrops identified previously [4].

Samples/methods: Three ~ 1.5 kg sediment samples were collected near the Santa Fe impact structure (Fig. 1). Sample 11NM03 is mixed colluvium/alluvium; 11NM04 is modern alluvium from Little Tesuque Creek; 11NM05 is colluvium. Detrital zircons from each sample were hand-picked and imaged with a scanning electron microscope (SEM).

SEM results: Backscattered electron imaging (BSE) was used to search for shock microstructures. A total of 400 detrital zircon grains were examined from sample 11NM05; planar microstructures were identified in two grains (2/400, or 0.5%). Planar fracture [5] sets consisting of open, parallel fractures with 1-10 μm spacing are visible on both exterior and interior surfaces (Fig. 2).

Discussion: These results are the first report of shocked zircons at the Santa Fe impact structure, and represent the third impact structure where detrital shocked zircons have been documented [1-3,5]. The detrital shocked zircons documented here contain planar fractures, which record shock pressures of ~20 GPa [6]; this pressure record is substantially higher than previous reports of ~10 GPa based on PDFs in quartz from bedrock [4]. The host rocks of the detrital shocked zircons have not been identified, but are probably nearby granite or supracrustal rocks [4].

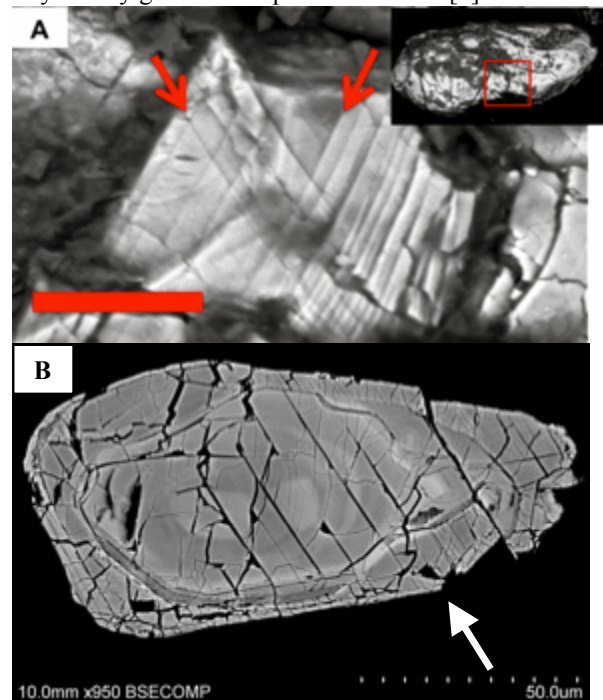


Figure 2. BSE images showing planar fractures (PFs) in detrital zircons from the Santa Fe impact structure. (A) BSE image showing two PF orientations on the exterior surface of grain 11NM05-13. (B) BSE image showing one PF orientation in the polished interior of grain 11NM05-16. Scale bar in (A) is 10 μm . Arrows indicate the orientation of planar fractures.

References: [1] Cavosie A. J. et al. (2010) *GSA Bull.*, 122, 1968-1980. [2] Erickson T. M. et al. (2013) *GCA*, 107, 170-188. [3] Thompson O. A. et al. (2014) *GSA Bull.*, in press. [4] Fackelman, S. P. et al. (2008) *EPSL*, 270, 290-299. [5] Erickson, T. M. et al. (2013) *Am Min*, 98, 53-65. [6] Leroux H. et al. (1999) *EPSL*, 169, 291-301.

New Geological Map of the Lunar Orientale Basin D. J. P. Martin, School of Earth, Atmospheric and Environmental Sciences, University of Manchester, Oxford Road, Manchester, United Kingdom, M13 9PL; dayl.martin@student.manchester.ac.uk

Introduction: Orientale is the youngest and best preserved multi-ring impact basin on the Moon [1]. Situated on the extreme western edge of the near side, observation of the basin from Earth is limited and only possible at a highly oblique angle. Therefore studying the basin effectively has been restricted to the analysis of spacecraft images and compositional maps. Recent missions such as the Lunar Reconnaissance Orbiter have provided much higher resolution images of the surface than previous missions, allowing detailed study of the surface of the moon and its features.

The most recent geological map of the Orientale Basin was made in 1978 using data from the Lunar Orbiter and Zond 8 missions [2]. The aim of this project was to create a new geological map of the Orientale Impact Basin using images and topographic data from the Lunar Reconnaissance Orbiter Camera (LROC) and LOLA topographic maps. Data from the Moon Mineralogy Mapper (M^3) and Clementine FeO and TiO_2 maps were used to determine the extent of differentiation of the impact melt sheet (if any) [3]. The updated map shows a more accurate representation of the distribution of units both inside and outside of the basin and provides a clearer insight into the distribution of the melt sheet, the geological context of impact melt inside the basin and nature of the basin-forming impact.

Methods: A WAC image mosaic of the western hemisphere of the moon (formed from images taken by the LROC) was centered on Orientale and used as a base-map in ArcGIS 10.0. Mapping data were taken from the WAC images and the GLD100 global topographic map derived from LOLA and WAC stereo images [4]. Clementine FeO and TiO_2 images [5] were used to aid in the identification and mapping of various units (for example finding areas of mare material with high FeO content in the texturally similar Maunder Plains). Separate units were defined by position within the basin, surface texture, composition, structure and stratigraphic (overlap) position. The unit names of the Orientale Group [5] and colors similar to those used on the map of Scott et al. [2] were used here in the updated map for maximum continuity with existing lunar maps; some of the formations were subdivided into a number of constituent members based on one or more of their characteristics varying throughout the formation.

Following the creation of the geological map, we conducted an analysis of the composition of the basin

impact melt sheet (the Maunder Fm. [3]). Using ArcGIS, the FeO and TiO_2 contents of the different formations could be analyzed by overlaying the different formations onto the Clementine maps and performing a statistical analysis of the element concentrations and distributions within the areas of the separate formations. Using this technique, the compositions of the ejecta blankets of over 300 craters within the Maunder Formation were analyzed to examine the lateral variations in melt sheet composition. To test for variation with depth, we analyzed crater size as a function of FeO content (based on the idea that larger craters excavate deeper material) [1, 3, 6].

Results: The basin interior displays a number of small melt ponds previously unmapped (recognized from comparison with the Clementine FeO map [4]). The Maunder Formation has been subdivided into two units – a smooth (plains) and a fissured member. Maunder fissured deposits have a relatively large range of surface topography. Maunder smooth member is flat and, in some areas, fractured by normal faults and graben.

The Montes Rook Formation has been split into three members – knobby, plains-like, and massifs. The knobby member contains large knobs or hummocks of material giving these areas a blocky and uneven appearance. However, flow lobes have been found in this unit adjacent to massifs or against some areas of the Cordillera Ring. The smooth member is concentrated in the southwestern quadrant of the basin interior. The final member of the M. Rook Fm. includes basin massifs of the Inner and Outer Montes Rook basin rings. These rings consist of blocky, equant massifs arranged in a circular pattern, unlike the scarp-like morphology of the inner most (shelf) and outer (Cordillera) rings.

The Hevelius Formation (basin exterior ejecta) has been split into four members: smooth, highland plains similar to the Imbrium basin Cayley Fm., radially textured ejecta (deposits lineated radial to the basin center), transverse ejecta (textured material oriented parallel or concentric with the basin rim), and a secondary crater facies. The radial ejecta is mostly situated to the north and south of the basin rim with the transverse ejecta facies being found mostly to the east and west. The radial facies seem to have greater average extent than the transverse facies, extending roughly 540 km and 350 km from the basin rim crest respectively. Smooth plains are in small, localized areas within the ejecta blanket and are more widespread outside of it. Secondary craters are abundant to the northwest,

southeast and southwest; relatively few are found to the east and northeast.

Analysis: The Mauser Fm. fissured member are thinner areas of the melt sheet that have been draped over lower-lying areas of massif material. Mauser smooth plains member are flat due to the melt sheet ponding and being locally thicker. Topographic analysis of the Inner Rook ring can be used to estimate a thickness of the melt sheet (as there are areas where the ring is completely covered by melt). The largest range is 6.2 km suggesting the melt sheet is ~6 km or less thick [3].

The Montes Rook Formation may contain some fraction of the impact melt due to the presence of flow lobes near to Cordillera Ring and extensive areas of the plains in certain locations. The origin of the knobby surface morphology remains an unsolved but important lunar problem [8].

The “bilateral symmetry” of ejecta distribution of the Hevelius Formation appears similar in some ways to the “butterfly pattern” of ejecta formed from low-angle impacts [e.g., 1]. The concentration of plains in certain areas, the distribution of secondary craters, and the distribution of ejecta facies all support the idea that the Orientale basin formed by an oblique impact from the east-northeast [1].

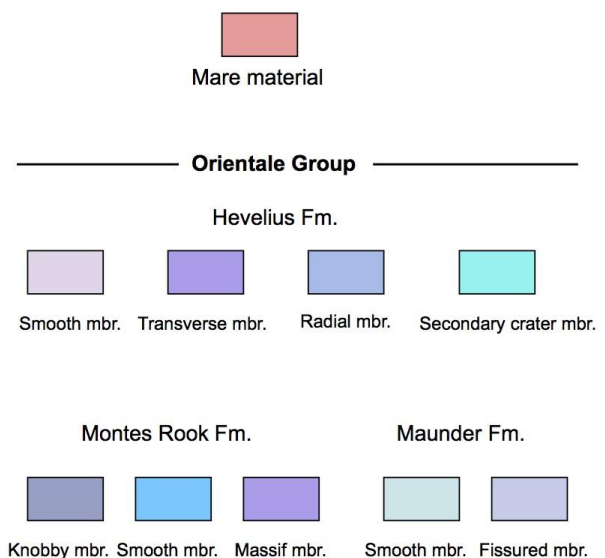
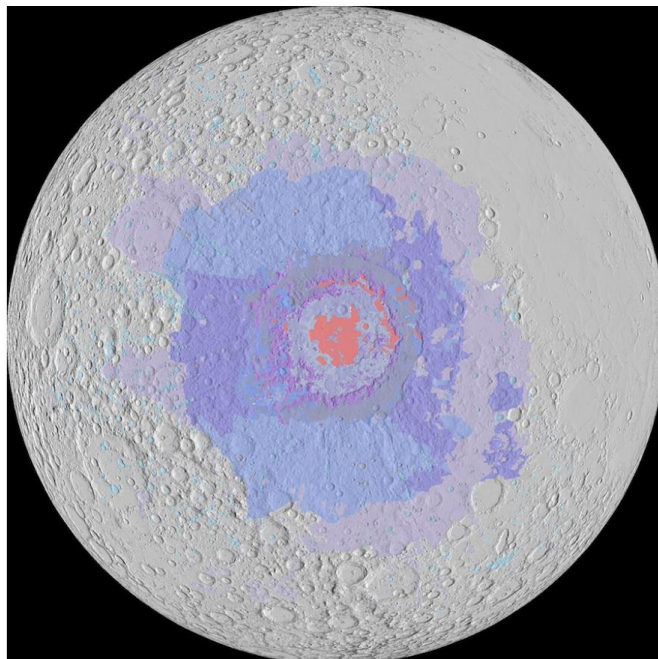
The composition of Orientale basin deposits are discussed in detail in a companion abstract [9]. Previous work based on partial coverage of the basin suggested a relatively uniform, anorthositic norite composition for all deposits [10]. This relation is still essentially correct, although some significant variations have been noted [9]. We specifically examined the compo-

sition of the Mauser Fm. of the basin to assess the possibility of differentiation of the basin impact melt sheet [3, 9]. So far, we have found no evidence for such differentiation. Numerous massifs that make up the Inner Rook Mts. are composed of pure anorthosite [10, 11], suggesting that this rock type occurs as a major regional unit at shallow depths.

Conclusions: An updated map of the Orientale basin and its surrounding ejecta shows the relations of basin units. The distribution of ejecta suggest that the basin formed by an oblique, low angle impact coming from east to west. The impact melt sheet (Mauser Fm.) has a maximum thickness of a few km at most. Orientale basin ejecta is very feldspathic, including outcrops of pure anorthosite within its rings.

References: [1] Wilhelms D.E. (1987) *USGS Prof. Paper 1348*. [2] Scott D.H. et al. (1978) USGS Map I-1034. [3] Spudis P.D. et al. (2013) *JGR* 118, doi:10.1002/2013JE004521 [4] Lucey P.G. et al. (2000) *JGR* 105, 20297. [5] Scholten F. et al. (2012) *JGR* 117, E00H17. [6] McCauley J.F. (1977) *PEPI* 15, 220. [7] Spudis P.D. (1993) *Geology of Multi-Ring Impact Basins* Cambridge Univ. Press. [8] Spudis P.D. et al. (2011) *JGR* 116, E00H03, doi:10.1029/2011JE003903 [9] Spudis P.D and Martin D.J. P., this vol. [10] Spudis P.D. et al. (1984) *JGR* 89, C197. [11] Cheek L. et al. (2013) *JGR* 118, 1805–1820

Fig. 1 – An updated geological map of the Orientale impact basin. Hemisphere centered on -19°, -95°.



The Effect of Grain Size and Abundance on the Deconvolution of Mixtures Using the Shkuratov Model. A.A. Martone¹ and T.D. Glotch¹, ¹Stony Brook University (255 Earth and Space Sciences, Stony Brook University, Stony Brook, NY 11794-2100)

Introduction: In this work we use the Shkuratov radiative transfer model to obtain mineral optical constants, and test the model's ability to deconvolve reflectance spectra of mineral mixtures and determine mineral grain sizes and abundances. The tests of the model focus on the effects of grain size and end member concentrations on the accuracy of the model.

The Shkuratov model approximates scattering through parallel plates, eliminating a dependence on incidence angle. It relies on a priori estimates of the real index of refraction (n), volume fraction filled by particles (q), and optical path length, or particle size (S), to determine the imaginary index of refraction (k) from reflectance spectra [1]. Values of k derived from this model are dependent on S , even though the value is an intrinsic mineral property and should be the same for a mineral at all grain sizes (figure 1). Poulet and Erard [2] discuss this and found that k values are substantially more accurate when calculated from mineral spectra of several sizes. In this study, we report the effect of singular particle size k values on the results of the deconvolution of mixtures.

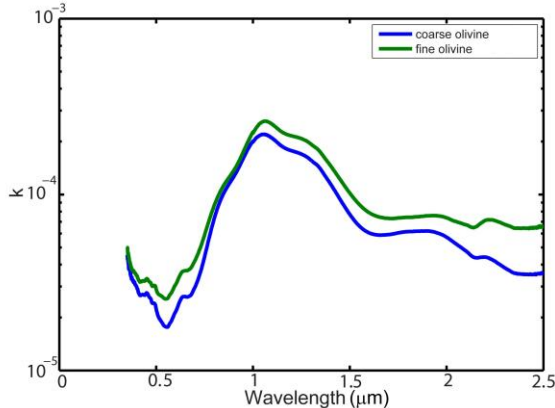


Figure 1: comparison of k values for the coarse (125-250 μm) and fine (63-90 μm) olivine

Our Matlab deconvolution code uses an optimization function that finds the minimum for a nonlinear multivariable function within set constraints. We employ the MultiStart algorithm which allows us to run the optimization from multiple points to increase the certainty that a global minimum has been found; it becomes increasingly difficult to find a global minimum when there is a large number of unknowns (ie: for a mixture with many end members).

Two Component Mixtures: We use two and three component mixtures consisting of olivine (OLV; 2 size

fractions), labradorite (PLG), augite (CPX), and enstatite (OPX). The potential accuracy of the model is demonstrated with the OPX/CPX mixture (2:1 mass fraction ratio). The abundances were determined with errors of 3% and 6%, respectively, with reasonable grain sizes (both have particle size ranges from 90-125 μm). The fit of the spectrum is shown in figure 2. OPX and CPX are kept in this 2:1 ratio for the 3 component mixtures.

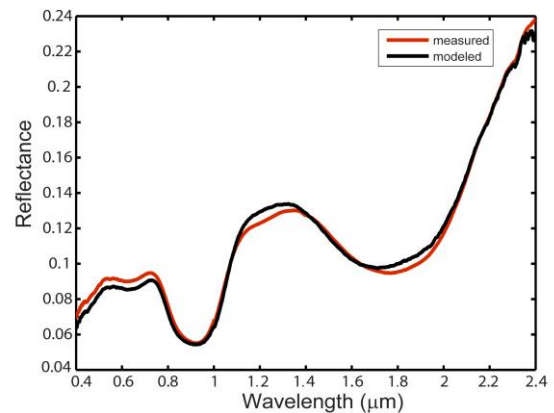


Figure 2: measured and modeled spectrum of OPX/CPX mixture

CPX and OLV were mixed using fine (63-90 μm) and coarse (125-250 μm) size fraction of OLV in 1:2, 1:1, and 2:1 mass ratios. The mixtures with coarse olivine provided more accurate model results for all three ratios compared to the finer olivine; the finer olivine mixture had a errors of 57% and 61% for the 1:1 mixture, 27% and 53% for the 2:1 mixture, and 29% and 15% for the 1:2 ratio, while the coarser olivine mixtures had errors of 22% and 22% for the 1:1 mixture, 15% and 36% for the 2:1 mixture, and 44% and 23% for the 1:2 mixture. All these results also produced particle sizes with reasonable agreement to the actual sizes. Mixtures in a 1:2 ratio were also made using a coarser CPX size fraction with a particle size range of 180-250 μm . For the coarser olivine mixture this produced errors of 14% and 8% (with a modeled CPX grain size of 500 μm), and the fine olivine 76% and 40%.

The effect of the size-dependent k value was observed by using the fine olivine k for the mixtures with coarse olivine, and vice versa. These effects are unpredictable, in some instances improving accuracy and in others decreasing it. The effect, however, is

small; the difference is $\leq 2\%$ for 14 of the 16 mixtures, the other two have a 5% and 7% difference.

Mixtures of CPX and PLG (125-250 μm) were made in 1:1, 1:2, and 2:1 ratios. These consistently overestimated the PLG by 15-20%, while the CPX errors ranged from 21%-45% with the 2:1 mixture producing the smallest error and the 1:2 mixture producing the largest. The grain sizes were within reason for all mixtures except the 2:1 ratio which produced a CPX size about three times larger than the actual size.

Three Component Mixtures: The three component mixtures consisted of OPX and CPX (kept in a 2:1 ratio), and either coarse OLV or PLG as an additional end member. Three mixtures were made for each in a (CPX+OPX):end member ratio of 1:1, 1:2, and 2:1. For the PLG-bearing mixtures, labradorite abundance was overestimated by the same percentage as it was in the two component mixture, OPX was always underestimated, and CPX was always overestimated. The PLG and OPX grain sizes were reasonable, but the CPX grain size was considerably larger than the actual size fraction. Despite these errors, a fitted spectrum is produced with a RMS value of .0947% (Figure 3). For the OLV-bearing mixtures, the OPX was again underestimated for all three ratios, CPX was overestimated for the 1:1 and 2:1 ratios and underestimated in the 1:2 ratio, olivine was overestimated for the 1:2 and 2:1 ratios and underestimated for the 1:1 ratio. As with the labradorite end member mixtures, the CPX grain size was drastically larger than the actual size fraction.

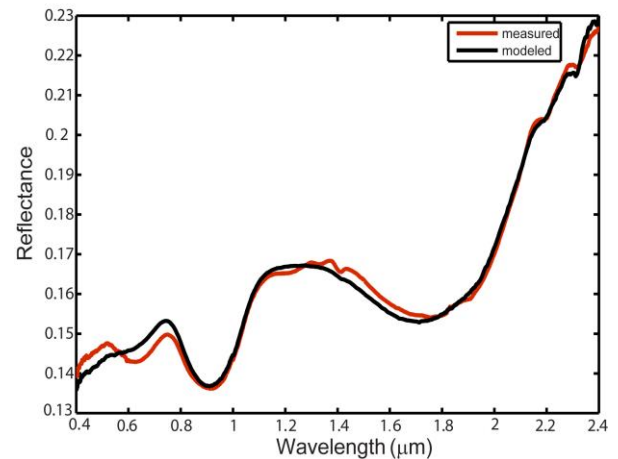


Figure 3: OPX+CPX/PLG measured and modeled spectrum

Discussion and Conclusions: The frequent modeling of a larger than actual grain size for CPX is likely due to the fact that CPX band contrast in the VNIR spectral range is poorly correlated with grain size [2]. The similarities between the CPX and OPX bands may make it difficult to distinguish between the two when another end member is introduced to the mixture. The OLV-bearing two component mixtures were modeled more accurately when the coarse OLV was an end member. In future work we will expand these tests by incorporating a different CPX end member and using additional size fractions of each end member.

References: [1] Yuriy Shkuratov et al. (1999) *Icarus* 137, 235-236 [2] F. Poulet and S. Erard (2004) *JGR*, Vol.109 [3] L. Moroz and G. Arnold (1999) *JGR*, Vol. 104

Table 1: percent errors of abundances for mixtures

	1:1	1:2	2:1
OPX:CPX	-	-	3%/6%
CPX:OLV(c)	22%/22%	23%/44%	36%/18%
CPX(c):OLV(c)	-	14%/18%	-
CPX:OLV(f)	61%/57%	15%/29%	53%/27%
CPX(c):OLV(f)	-	76%/40%	-
CPX:PLG	33%/40%	45%/27%	21%/52%
(OPX+CPX):PLG	38%/36%/22%	52%/5%/19%	65%/260%/13%
(OPX+CPX):OLV	54%/160%/8%	39%/71%/27%	61%/32%/66%

EXAMINING EFFECTS OF ORBITAL FORCING ON TITAN'S DUNE ORIENTATIONS.

G.D. McDonald¹, A.G. Hayes¹, R.C. Ewing², T. Tokano³, A. Lucas⁴, and G. Chen⁵. ¹Department of Astronomy, Cornell University, Ithaca NY; ²Department of Geology and Geophysics, Texas A&M University, College Station TX; ³Institut für Geophysik und Meteorologie, Universität zu Köln, Köln Germany; ⁴AIM Laboratory, Paris Diderot University, Paris France ⁵Department of Earth and Atmospheric Sciences, Cornell University, Ithaca NY.

Executive Summary: We explore the possibility that the orientations of Titan's equatorial dunes reflect integrative winds over orbital timescales of tens of thousands of years.

Dunes are the dominant geomorphology in Titan's equatorial terrain, covering an estimated 20% of the surface [1]. Numerous studies on the morphologic expression of these dunes and their interactions with topographic obstacles have been used to infer the wind regime responsible for their formation. Most studies have inferred west-to-east dune-forming winds [2,1,3] which cannot be consistently produced by most Global Climate Models (GCMs) and require invoking intermittent phenomena in the vicinity of autumnal and vernal equinox (e.g. [4]). These previous studies have focused primarily on examining the ability of rare westerly winds cycling over tidal or seasonal timescales to produce the currently observed dune orientations [4].

In this study, we examine the possibility that Titan's dunes are responding to cyclic variations in the wind regime over significantly longer (e.g., Milankovich) timescales. On Earth, large linear dunes similar in size to Titan's can take up to 100 thousand years to reorient their patterns in response to changes in the local wind regime [5]. On Titan, conservative estimates of the expected reorientation timescale have indicated values between 10^3 to 10^5 Titan years [6], suggesting that the dunes could be responding to bimodal winds with a longterm duty cycle on the order of Titan's proposed ~45 kyr Milankovich cycles [7]. Reoriented portions of linear dunes provide observational evidence that the dunes are being affected by changes in the wind regime (Fig. 1).

Titan's Milankovich cycles are primarily a result of changes in the eccentricities and planetocentric longitude of perihelion (L_{sp}) of Saturn's orbit around the sun [7]. The dominant ~45 thousand year cycle results in Titan's L_{sp} coinciding with different seasons (Fig. 2). From a climatic perspective, the four extrema in this orbital cycle occur when L_{sp} (and consequently peak solar flux) coincide with southern summer solstice (~2 kyrs ago, closest to the modern day configuration), autumnal equinox (18 kyr ago), northern summer solstice (33 kyr ago), and autumnal equinox (40 kyr ago). The possible implications of these orbital cycles

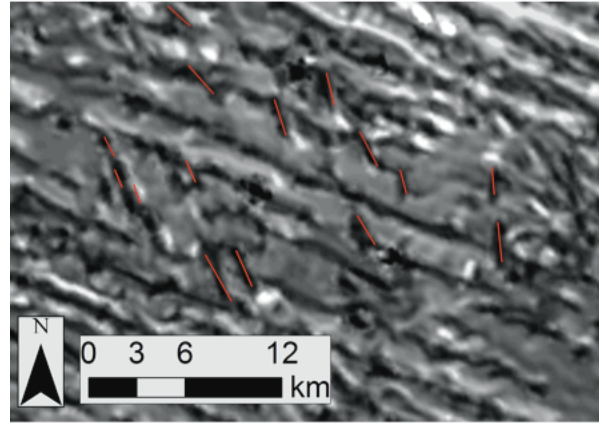


Figure 1: Reoriented dune crestlines (marked in red) in Titan's Belet dune field (170° E, 3.5° N). The image is a Cassini SAR image processed through a de-noising algorithm [8]. Reoriented crestlines are also visible in raw SAR images.

for the observed asymmetry in the distribution of Titan's polar lakes has already been established [7], making it natural to consider the effects of the cycle on Titan's other geomorphological features.

In order to examine the effects of changes in Titan's orbital configuration on dune orientations, we must first understand effects on the wind regime. This is accomplished by running a 3-dimensional GCM, incorporating topography [4] for one Titan year corresponding to the four aforementioned orbital extrema. The zonal and meridional surface wind outputs from the GCM are provided in locations corresponding to well developed portions of Titan's five largest dune fields (Fensal, Astlan, Belet, Shangri La, and Senkyo) 24 times per Titan day.

These surface wind outputs can be used to directly infer ideal dune orientations. It has been established through experiment and observational field work that dunes orient themselves so as to maximize gross bedform-normal transport—defined as the total amount of sediment transported (i.e. in either direction) perpendicular to dune crests [9]. The GCM produced annual surface wind distributions for a given dune field and orbital configuration are used to determine a gross bedform-normal transport maximizing dune orientation. This process is repeated for the wind distributions of each of the four orbital extrema, with an additional run combining the wind distributions of all four orbital extrema, in each of the five dune fields.

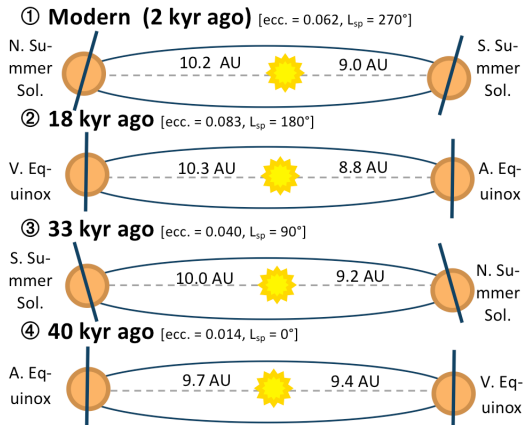


Figure 2: Titan's four orbital extrema during the past 45 thousand years. Titan's relative motion to Saturn is ignored.

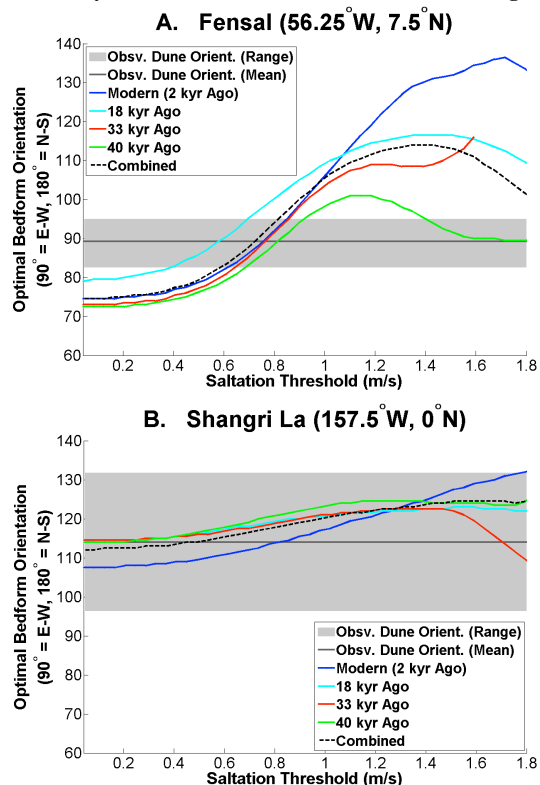


Figure 3: GCM predicted gross-bedform normal transport maximizing dune orientations for wind conditions corresponding to each of Titan's four orbital extrema and a combined wind regime, as well as the range of orientations observed by Cassini. Plots are for Fensal and Shangri La, two of the five studied dune fields. Orientation refers to the direction of the dune crestline, and is measured clockwise from north.

Our study compares the gross bedform-normal transport predicted dune orientations with the currently observed range of dune orientations. The observed dune orientations are determined through mappings of well-organized dunes, separated from topographic obstacles, observed in Cassini Synthetic Aperture Radar

(SAR) images. The predicted dune orientations are plotted as a function of saltation threshold, which is unknown for Titan. Lorenz et al. 2012 estimated a saltation threshold of ~ 1 m/s by scaling the derivation presented in Iversen et al. 1976, however the interparticle forces that dominate interactions between silicate grains (e.g., Van der Waals) may not be appropriate for hydrocarbon grains. Preliminary results demonstrate that in all five dune fields, the orbital configuration has an effect on the predicted dune orientation, with the significance of that effect varying by region (Fig. 3). Furthermore, the results indicate a close correspondence between predicted and observed dune orientations for three of the five dune fields. In Fensal, for saltation thresholds greater than ~ 1 m/s, ideal dune orientations for the different orbital extrema diverge significantly compared to the range of observed dune orientations (Fig. 3A). The predicted dune orientations for past orbital configurations, notably that of 40 kyr ago, are in greater agreement with the currently observed orientations than those predicted by modern wind conditions. This may be indicative of direct observation of the effects of orbital forcing on dune orientations. We are in the process of using other Titan GCMs, including TitanWRF [12] and the GCM described in Schneider et al. 2012 to verify these effects.

Our preliminary results confirm that Titan's orbital configuration has an effect on predicted dune orientations and suggest that these effects may be observed today in Fensal. The potential significance of orbital forcing on modern dune orientations reinforces the necessity of considering the effects of climatic variations over long timescales in studies of geomorphology. Additionally, these results emphasize that dunes are an invaluable record of Titan's climate, and that their study can further our understanding of Titan's historical climatic conditions.

References: [1] Radebaugh J. et al. (2008) *Icarus*, 194, 690-703. [2] Lorenz R.D. et al. (2006) *Science*, 312, 724-727. [3] Radebaugh J. et al. (2010) *Geomorphology*, 121, 122-132. [4] Tokano T. (2010) *Aeolian Research*, 2, 113-127. [5] Werner B.T. and Kocurek G. (1999) *Geology*, 27(8), 727-730. [6] Hayes A.G. et al. (2012) *Internat. Planet. Dunes Workshop III*, Abstract #7057. [7] Aharonson O. et al. (2009) *Nature Geoscience*, 2, 851-854. [8] Lucas A. et al. (2012) *LPSC XLIII*, Abstract #2566. [9] Rubin D.M. and Hunter R.E. (1987) *Science*, 237, 276-278. [10] Lorenz R.D. et al. (2012) *Internat. Planet. Dunes Workshop*, Abstract #7014. [11] Iversen J.D. et al. (1976) *Icarus*, 29(3), 381-393. [12] Newman C.E. et al. (2011) *Icarus*, 213(2), 636-654. [13] Schneider T. et al. (2012) *Nature*, 48, 58-61.

Determining physical properties of Titan's empty lake basins through radar backscatter modeling.
R. J. Michaelides¹ and A. G. Hayes¹, ¹Cornell University, Ithaca NY 14853; rjm342@cornell.edu.

Abstract: We use repeat SAR observations to study the scattering properties of Titan's paleo-lake basins. The best-fit coefficients to standard quasi-specular plus diffuse backscatter models show that the bright basin floors have a higher dielectric constant, but similar RMS surface roughness, to surrounding terrain. This suggests that floor deposits are compositionally distinct to their surroundings, consistent with the interpretation that these basins are partially filled with evaporitic deposits, as previously suggested by their relative brightness at mid-infrared wavelengths. The basin floor deposits also express a larger diffuse component to their backscatter, suggesting variations in subsurface structure causing increased volume scattering.

Background: Surface conditions on Titan occur over a temperature and pressure range near the triple-point of methane, potentially allowing solid, gaseous, and liquid phases to co-exist. On Titan, methane and ethane act like water on Earth; raining out of the atmosphere, carving channels, and forming lakes in polar basins [1]. Observed lacustrine features on Titan are found in varying states of liquid fill (Figure 1) [2]. The dark features are interpreted as lakes and/or seas of liquid methane and ethane. Bright features of similar plan-view morphologic expression to the filled lakes, which are found to be hundreds of meter deep depressions and compositionally distinct from surrounding terrain, are interpreted as empty paleo-lake basins that are potentially filled with evaporitic deposits [2,3]. Lacustrine features of intermediate brightness, which are above the noise floor of the Cassini RADAR instrument but still dark relative to their surroundings, are interpreted as either shallow lakes that are penetrable by radar or saturated regolith.

While the larger Mare (Ligeia, Kraken and Punga) have fluvial networks flowing into them, the smaller lakes are not associated with any obvious surface drainage at the ~300 m resolution of Synthetic Aperture Radar (SAR) images [2]. In the absence of surface drainage, these lakes either interact directly with the atmosphere or have sub-surface drainage networks linked to an underground alkanofer [2]. If lacustrine features exhibit significant exchange of liquids either through surface run-off, evaporation or sub-surface infiltration, then their evolution may be observable and leave traces behind such as evaporitic or sedimentary deposits. Furthermore, if the liquid inputs of a lake are in disequilibrium with its outputs, we can expect the lake to evolve over time. The interpretation of intermediate brightness lakes as

shallow and bright lakes as evaporated lake depressions suggests that the shallow lakes may be a transitional morphology as dark lakes evolve into empty lakes and vice-versa. Analysis of SAR backscatter curves of south polar lakes has supported the conclusion that observed differences in some small southern lake features are consistent with temporal variability of the liquid level [4]. Observations of the north polar region, however, have so far shown no unambiguous changes in lake level [4]. Systematic variability (as a function of observational geometry) in the backscatter of lacustrine features in both hemispheres, however, have suggested compositional and/or structural differences between the lake basins and their surrounding terrain [1,4]. These differences are the focus of this work.

Methods: The Cassini Mission's entrance into its second extended mission has resulted in repeat SAR coverage of several areas of Titan's north polar region, which in some locations have been observed up to seven times. In addition to providing temporal coverage, these observations represent an opportunity to analyze the scattering properties of lacustrine features at varying incidence angles. The T86 swath for example, which was acquired on 09/27/12, contains partial overlap with swaths T28 (04/10/07) and T29 (04/26/07) and was acquired as significantly larger incidence (~50° in T86 vs. ~20° in T28/T29). The overlap of these three swaths is particularly interesting because it contains an area of concentrated partially-filled and empty lakes. The SAR returns of the lacustrine features in T86 are remarkably different from those of T28 and T29. These differences can be used to discern the relative variation in the physical properties of lacustrine features as compared to their surrounding terrain.

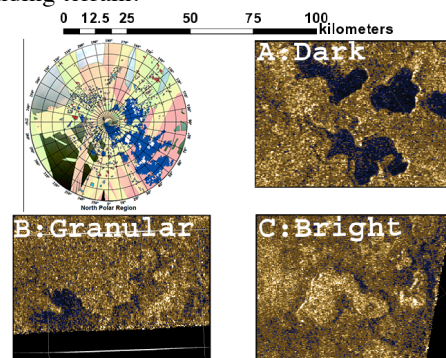


Figure 1: Examples of the three lake classes observed on Titan. **A:** Dark features are interpreted as liquid-hydrocarbon filled lakes. **B:** Granular features, are interpreted as a continuum between saturated regolith and partially-filled lakes. **C:** Bright lakes are interpreted as empty basins. Adapted from [2].

Herein we take advantage of the repeat RADAR coverage of Titan's polar terrain to study the backscatter properties of the bright empty paleo-lake basins. SAR images have the highest resolution of all operational modes (up to ~ 250 m/pixel). However, SAR imaging is typically restricted to a fairly narrow range of incidence angles [5]. By combining SAR with HiSAR and closest-approach altimetry, a wide range of viewing geometries can be investigated (scattering angles of $\sim 0^\circ$ - 50°) for specific lacustrine features at spatial scales of a few km.

The bright paleo-lake basins have the highest backscatter returns of all lacustrine features and are interpreted as 200-300 m depressions consistent with previously filled lakes [1]. The bright returns from the floor deposits in these features are interpreted by [3] as evaporite based on their relative brightness at 5 μ m. Additionally, it was recently shown that while the relative depths of empty lake basins vary over a range of several hundred meters, the absolute floor elevations of north polar empty lakes are clustered around the elevation of Mare shorelines [6]. While prior investigations have pointed out the unique scattering properties of empty lake basins by comparing off-axis SAR to nadir-pointed altimetry [1] for one empty lakes feature, we expand upon previous work by investigating multiple features with multiple overlapping datasets, permitting quantitative assessment of their scattering properties.

The Cassini RADAR's ability to infer physical and compositional properties of observed features on Titan is dependent upon knowledge of different scattering models frequently employed in radar and planetary science. For solid surfaces, RADAR backscatter is typically modeled using a quasi-specular facet model, which models the surface as a series of planar facets oriented at varying angles with respect to the normal of a perfectly smooth surface. Each facet produces a coherent reflection, and these reflections sum to the specific radar cross section (σ_0 , defined as the area of an isotropic scatter normal to incidence required to yield the observed RADAR echo intensity, normalized by the actual surface area of the region of interest) [9],[10]. Quasi-specular models relating σ_0 to the angle of incidence, θ , have been successfully used to infer the surface properties of terrestrial planets (Mercury, Venus, Earth, Mars, and the Moon) [see, for example, 10]. On Titan, the transparent properties of water-ice and hydrocarbon solids necessitate the addition of a diffuse term to allow for subsurface volume scattering [9]. In this study, we have fit observed backscatter to quasi-specular plus diffuse models that use Hagfors, Gaussian, and Exponential quasi-specular terms and a \cos^n diffuse term as in [9]. Our models are dependent upon the surface dielectric constant, surface RMS facet angle (i.e., roughness),

and amplitude of the diffuse term. We use a Levenberg-Marquadt least squares minimization to find the best-fit model coefficients for the bright paleo-lake basins and their immediate surrounding terrain (Figure 2).

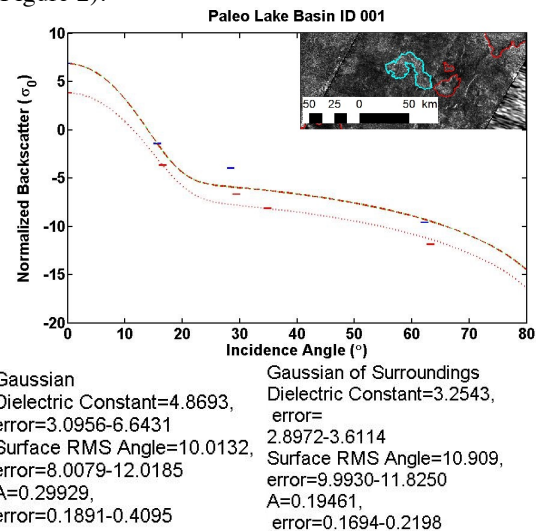


Figure 2: Example scattering curves and best-fit model coefficients for empty lake feature 001 and its surroundings. The Gaussian, Hagfors, and Exponential models all predict a higher dielectric constant and diffuse term for the feature with respect to its surroundings, and comparable RMS angles.

Results: Results from modeling 7 features suggest that the empty lake basins have a higher dielectric constant than their surroundings, but a similar RMS angle to within error (68% CI). This is true regardless of which quasi-specular model (Hagfors, Gaussian, or Exponential) is used to fit the observations. Additionally, all three models predict a higher diffuse amplitude for the basins than the surroundings, suggesting either an increased subsurface volume scattering component or increased small-scale roughness (wavelength-scale as opposed the facet-scale). Future work will focus on spreading the above-mentioned methods to all paleo-lake basins that have been imaged with SAR sufficiently to allow the derivation of model coefficients. These results will help to constrain the physical properties and formation mechanisms of the paleo-lake basins, and provide insight into their role in Titan's surface processes.

References: [1] Stofan et al. (2007), *Nature*, 445. [2] Hayes A. G. et al. (2008) *GRL*, 35. [3] Barnes J. W. et al. (2011) *Icarus*, 216. [4] Hayes A. G. et al. (2011) *Icarus*, 211. [5] Elachi et al. (2004) *Space Sci. Rev.*, 115 [6] Hayes A. G. et al. (2013) EPSC. [7] Hagfors T. (1964), *JGR* 69. [8] Elachi C, (2006) Introduction to the Physics and Techniques of Remote Sensing. [9] Wye L. C. (2007) *Icarus*, 188. [10] Pettengill (1978), *Annual Reviews* Vol. 16.

A CONSTRAINT ON SHOCKED MINERAL ABUNDANCE IN THE JACK HILLS ZIRCON SUITE.P.E. Montalvo¹, A.J. Cavosie^{1,2}, and J.W. Valley²¹University of Puerto Rico-Mayagüez, ²University of Wisconsin-Madison

Introduction: Numerous studies have confirmed that 3.0 Ga metasedimentary rocks from the Jack Hills, Western Australia, contain abundances of ~10% Hadean (>4.0 Ga) detrital zircons [1]. Detrital shocked zircons eroded from known impact structures such as Vredefort and Sudbury have been reported in modern siliciclastic deposits [2,3], including distal alluvium [4]. The Jack Hills zircon suite, which contains grains ranging in age from 4.4 to 3.0 Ga [1,5], thus offers an opportunity to evaluate if detrital shocked zircons eroded from Hadean impact structure are preserved. Here we report the results of an SEM survey of 1400 Jack Hills zircons for shock microstructures. No shocked grains were identified, which places a maximum constraint of $\leq 0.07\%$ for the abundance of shocked zircons in the Jack Hills suite, if indeed they are found to be present.

Earth's early impact history: The lack of a terrestrial rock record older than ~4.0 Ga hampers the study of early impact process. The oldest evidence of impact are ca. 3.5 Ga spherule deposits [6], however source craters have not been identified. The oldest shocked mineral is quartz from a 2.6 Ga spherule deposit [7], and the oldest confirmed and well-dated structure is the 2.0 Ga Vredefort Dome [8,9].

Detrital shocked minerals: Shocked minerals provide diagnostic evidence to confirm an impact [10]. Shocked zircons have been shown to survive post-impact thermal conditions, uplift, erosion, and distal sedimentary transport [2-4]. While quartz is susceptible to erosion, shock microstructures in zircon resist annealing [11,12].

Sample/Methods: The studied grains are from sample 01JH13 [13], the same layer as the well-known sample W74 [14]. The rock sample is a clast-supported quartz cobble metaconglomerate. Zircons were hand-picked and mounted on scanning electron microscope (SEM) stubs for backscatter electron (BSE) imaging of grain surfaces.

Results: A total of 1,400 undated detrital zircons were analyzed. Grain morphologies are variable, ranging from euhedral grains with little evidence of abrasion (Fig. 1a) to anhedral rounded grains. No shock microstructures were identified.

Discussion: The absence of shocked zircons allows a constraint of $\leq 0.07\%$ (less than 1 in 1400) to be placed on the abundance of shocked grains in this Jack Hills suite. Of the 1400 grains, 10% were likely Hadean; the maximum constraint for the Hadean grains is thus $\leq 0.7\%$ (less than 1 in 140), if present.

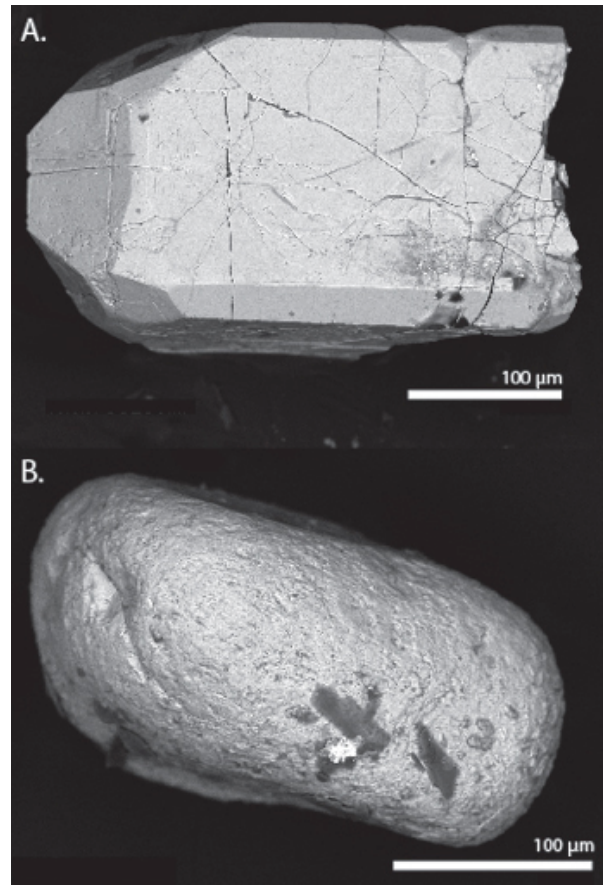


Figure 1. BSE images of detrital zircon grains from Jack Hills sample 01JH13 showing (a) euhedral and (b) anhedral morphologies.

References: [1] Cavosie A. J. et al. (2007) *Earth's Oldest Rocks*. [2] Cavosie A. J. et al. (2010) *GSA Bull.*, 122, 1968-1980. [3] Thompson O. A. et al. (2014) *GSA Bull.*, in press. [4] Erickson T. M. et al. (2010) *GCA*, 107, 170-188. [5] Valley J. W. et al. (2014) *Nature*, in press. [6] Byerly G. R. et al. (2002) *Nature*, 297, 1325-1327. [7] Rasmussen R. and Koeberl C. (2004) *Geology*, 32, 1029-1032. [8] Kamo S. L. et al. (1996) *EPSL*, 144, 369-387. [9] Moser, D. E. (1997) *Geology*, 25, 7-10. [10] French and Koeberl (2010) *ESR* [11] Timms N. E. et al. (2012) *Meteoritics & Planet. Sci.*, 47, 120-141. [12] Erickson, T. M. et al. (2013) *Am Min*, 98, 53-65. [13] Cavosie A. J. (2005) PhD Thesis, Univ. Wisc. [14] Compston W. and Pidgeon R. T. (1986) *Nature*, 321, 766-769.

SULFUR COMPOSITIONAL EFFECTS ON SPACE WEATHERING

Jeffrey N. Murl
Department of Geology and Geophysics
School of Ocean and Earth Science and Technology
University of Hawai'i at Mānoa
POST Building, Suite 701
1680 East-West Road
Honolulu, HI 96822 USA

ABSTRACT

The reflectance spectrum of visible and near infrared light off of airless bodies in our Solar System gives us insight to surface mineralogy. However, this method of remote sensing is subjected to the space weathering effects of darkening and reddening optical spectra, along with changes to the depths of absorption bands over time. These optical changes are caused by nanophase iron blebs as a result of micrometeorite impacts and solar wind radiation. These two space weathering processes create melt and vapor deposits that coat mineral grains. The amount of vapor and melt is a function of mineral composition. We seek to understand the effects of sulfur on a refractory composition such as anorthosite, which is commonly found in the regolith of the moon's highlands and possibly Mercury. X-ray spectrometry from the MESSENGER mission, Nittler (2011), returned a "sulfur abundance of up to ~4% weight in surface materials". We will use sulfur compositions of 0%, 2%, 4%, and 8% weight in anorthosite samples. In line with NASA's Strategic Goals of understanding processes and surface evolution of solar bodies, this experiment investigates the effects of sulfur composition on simulated space weathering of anorthosite. The results of this experiment show that the presence of sulfur in the Mercurian soil can contribute to 16% darker and 72% redder spectra; However, sulfur does not fully explain the 1.5 times lower in reflectance as compared to immature lunar highlands materials. Additional means are necessary (e.g., impact shock and melting) to explain the difference in brightness between the Moon and Mercury.

REFERENCES

Nittler, L. R., Starr, R. D., Weider, S. Z., McCoy, T. J., Boynton, W. V., Ebel, D. S., Ernst, C. M., et al. (2011) The major-element composition of Mercury's surface from MESSENGER X-ray spectrometry. *Science*, 333(6051), 1847–50. doi:10.1126/science.1211567

FIGURES

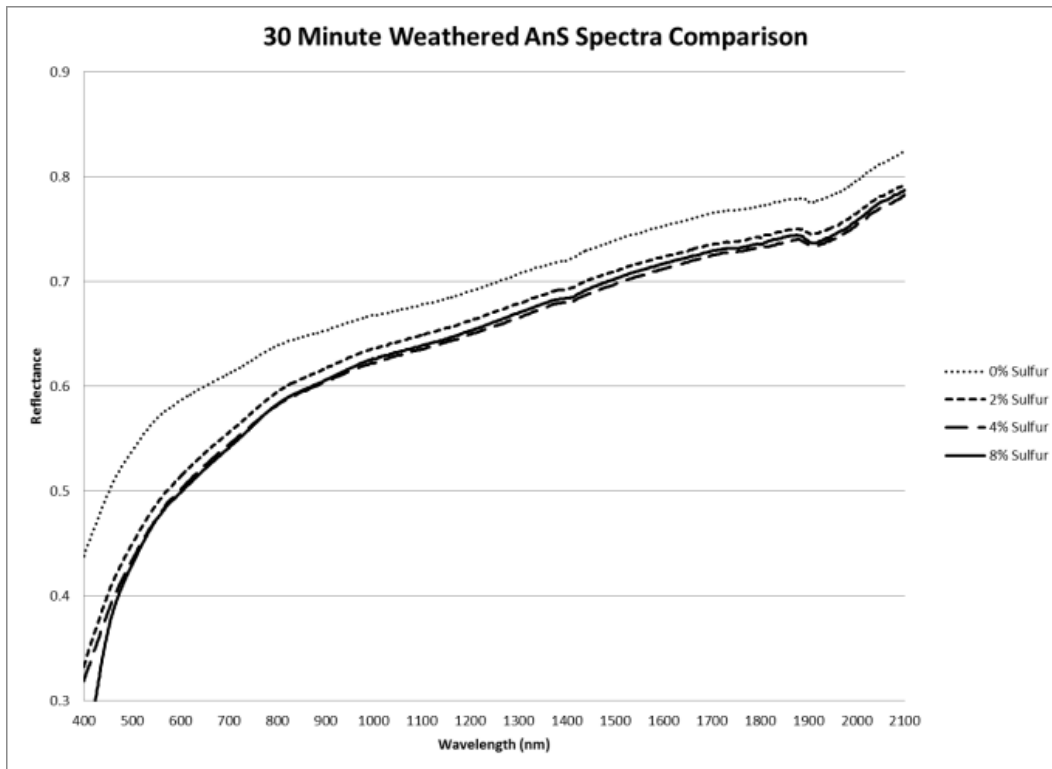


Figure 1: Spectra after 30 minutes of pulsed-laser simulated space weathering

0% Sulfur - Darkening at 550nm			
Minutes	Reflectance	% Change	Overall Δ
0	0.65111056	0	-12.63
5	0.63304221	-2.78	Mean
10	0.62524145	-1.23	-2.22
15	0.60651438	-3.00	SD
20	0.59627298	-1.69	0.61
25	0.58318059	-2.20	SDM
30	0.56888513	-2.45	0.25

0% Sulfur - Reddening at 750 to 1800nm					
Minutes	750nm	1800nm	Slope	% Change	Overall Δ
0	1	1.17494535	0.00016661	0	33.88
5	1	1.191988324	0.00018285	9.74	Mean
10	1	1.199594277	0.00019009	3.96	5.03
15	1	1.214851925	0.00020462	7.64	SD
20	1	1.216421704	0.00020612	0.73	3.01
25	1	1.222233334	0.00021165	2.69	SDM
30	1	1.234213596	0.00022306	5.39	1.23

2% Sulfur - Darkening at 550nm			
Minutes	Reflectance	% Change	Overall Δ
0	0.67031003	0	-27.29
5	0.64107343	-4.36	Mean
10	0.6113602	-4.63	-5.15
15	0.56891593	-6.94	SD
20	0.53173737	-6.53	1.97
25	0.52414288	-1.43	SDM
30	0.48735014	-7.02	0.81

2% Sulfur - Reddening at 750 to 1800nm					
Minutes	750nm	1800nm	Slope	% Change	Overall Δ
0	1	1.151077792	0.00014388	0	91.56
5	1	1.179096466	0.00017057	18.55	Mean
10	1	1.200013435	0.00019049	11.68	11.56
15	1	1.229307784	0.00021839	14.65	SD
20	1	1.260291893	0.00024790	13.51	5.16
25	1	1.265547165	0.00025290	2.02	SDM
30	1	1.289408592	0.00027563	8.99	2.11

Figure 2: Spectral data comparison of two weathered samples

METHODOLOGY OF WIND TUNNEL EXPERIMENTS APPLIED TO GRAVEL MEGARIPPLE FORMATION ON EARTH AND MARS. E. M. Neely¹, M. G. Spagnuolo², S. L. de Silva³, N. T. Bridges⁴, J. R. Zimbelman⁵, ¹Department of Geology, Portland State University, 1825 SW Broadway, Portland, OR 97201 (emneeson@pdx.edu), ² IDEAN, UBA-CONICET Ciudad de Bs. As., Argentina, ³College of Earth, Ocean, and Atmospheric Sciences, Oregon State University, Corvallis, OR 97331, ⁴JHUAPL, Laurel, MD 20723, ⁵CEPS/NASM MRC 315, Smithsonian Institution, Washington D.C. 20013-7012.

Introduction: Aeolian transport is the most active geomorphic agent on Mars today. Transverse Aeolian Ridges (TARs) are a landform intermediate in morphology between dunes and megaripples [1,2]. The origin and evolution of TARs has been debated in the literature [1-5], in large part because, until recently, suitable terrestrial analogs were lacking. However, recent work shows that the gravel megaripples in the Argentine Puna have many morphologic similarities [6], making the study of this region critical for understanding TARs. Part of this investigation is to quantify the wind speeds needed to move the megaripple material. These gravel bedforms are built on a local substrate of ignimbrites and composed of a bimodal association of dense ($>2 \text{ g/cm}^3$) lava and metamorphic clasts up to 2.5 cm in diameter (here called “lithics”), and pumice clasts ($<1.5 \text{ g/cm}^3$) up to 5 cm in diameter.

Samples of megaripple materials were used in wind tunnel experiments at the Arizona State University Wind Tunnel (ASUWIT). The objective was to determine threshold wind velocities for movement of these clasts. Once threshold velocities are established, they can be applied to similar landforms on Earth and ultimately on Mars (TARs) by scaling to Martian gravitational and atmospheric density conditions [1]. Several experiments were made, changing environment conditions: (1) Fluid, where the only lateral force was the wind (2) Quartz Impact, in which sand were dropped from the upwind hopper and (3) Scoria Impact, in which scoria material were dropped from the upwind hopper. The experiments were recorded in oblique view to be able to see the type of movement of the clasts (e.g. saltation). The results of this work are also described in [6] and [7]. The focus of this abstract is on the methodology.

Methods: In order to quantify the movement of clasts and the threshold velocities we used Kinovea software, which allows precise video measurements. Before the data could be analyzed, the wind tunnel

data were calibrated to get proper measurements of clast size, migration direction, and speed.

In order to determine the diameter of moving clasts, accurate reference dimensions of the wind tunnel experiment floor were measured. Because the camera views of the experiments were oblique, obtaining an accurate scale for each clast required consideration of camera angles and distances.

Diameters measured in pixels from images taken from the experiment videos were most accurately obtained with rounded, spherical clasts. In cases where the moving clast was elongated and/or angular, the diameter could not be measured in the same way, as it provided a skewed measurement in one direction.

Once a clast was observed as moving, the diameter was measured in pixels parallel to the width of the wind tunnel. The width of the wind tunnel was also measured at the location of the clast and a conversion measurement was then determined (Fig. 1).



Fig. 1. Perspective view of ASUWIT experiment showing one clast and tunnel width measurement.

The clast was then classified according to movement type (vibrating, sliding, rolling, or saltating), composition (pumice or lithic), and location (patch or edge and up- or down-wind). Freestream wind velocities were obtained at the time of beginning of clast movement (Fig. 2).

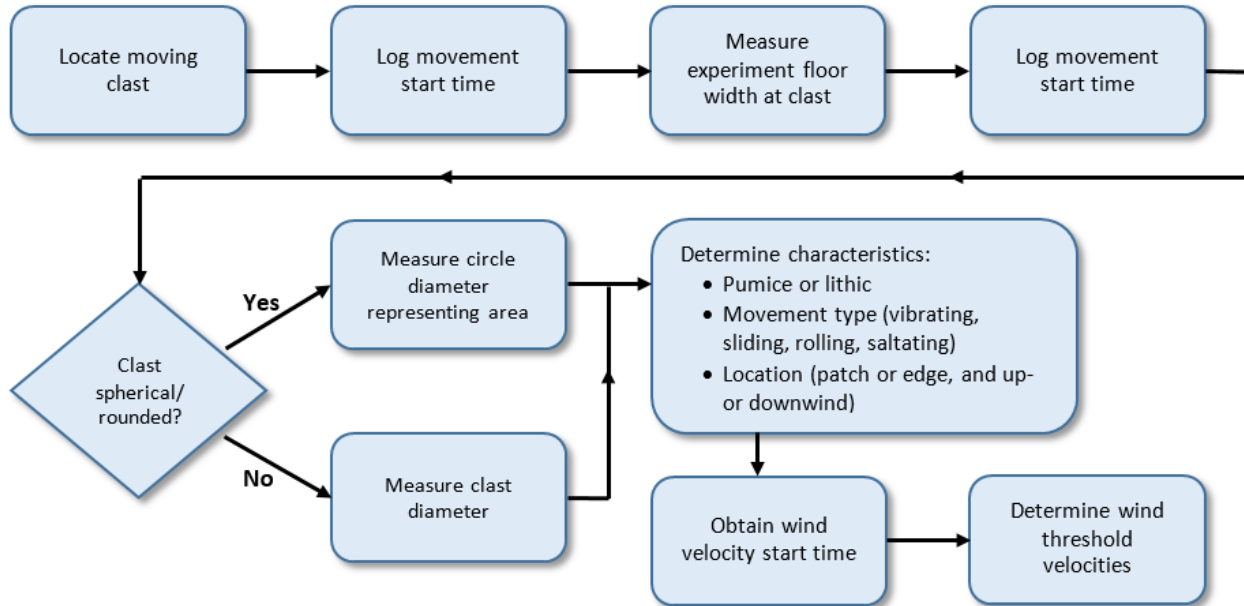


Fig. 2. Flow chart showing the methodological steps for clast analysis within the Kinovea software.

These data estimate wind threshold velocity for different types of grains. The same sets of measurements were completed for one of the experiment videos by two people separately and measurement sets were compared to each other. The coefficient of determination showed the regression line fit the data well and the comparison showed sufficient method reliability (Fig. 3). These data are the first (that we are aware of) of threshold speeds for large clasts that compose megaripples in the Puna, and possibly Mars.

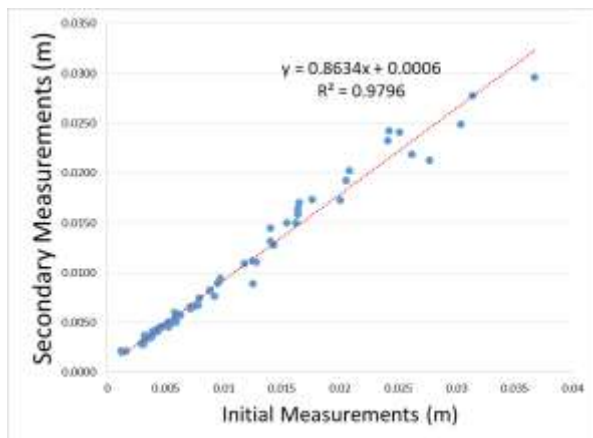


Fig. 3. Two measurements of the same clast diameters by different people using the same experiment video.

Results: A table was constructed with all of the computed values for each clast, providing a semi-quantitative analysis of the experiments. Preliminary results show a correlation between the clast diameter and saltation threshold wind speed. Some dispersion is

caused by clasts shapes and the fact that only one direction of the clast was measured. Nevertheless this technique allows comparison of data between different experiments and even with field data (An abstract describing extended results is presented at this conference [7]).

References: [1] Zimbelman, J.R. [2010], *Geomorph*, 121, 22-29. [2] Shockey, K.M. and J.R. Zimbelman [2013], *Earth Surf. Proc. Landforms*, 38, 179-182. [3] Balme, M. et al. [2013], *Geomorph*, 101, 703-720. [4] Kerber, L. and J.W. Head [2011], *Earth Surf. Proc. Landforms*, <http://dx.doi.org/10.1002/esp.2259>. [5] Berman, D.C. et al. [2011], *Icarus*, 213, 116-130. [6] de Silva, S., Spagnuolo, M. G., Bridges, N., Zimbelman, J. R. (2013) *GSA Bulletin*, 125, 1912-1929. [7] Bridges, N.T. et al., *Lun. Planet. Sci*, XLV.

COMPRESSION STRENGTH OF PUMICE. E. B. Patmore¹, M. M. Strait¹, G. J. Flynn², and D. D. Durda³
¹Dept. Of Chemistry, Alma College, 614 W. Superior St., Alma MI 48801 (patmore1eb@alma.edu), ²Dept. Of Physics, State University of New York-Plattsburgh, Plattsburgh NY 12901, ³Southwest Research Institute, 1050 Walnut Street Suite 3400, Boulder CO 80302.

Introduction: Asteroid impacts produce small particles that contribute to interplanetary dust particles, micrometeorites and meteors, all of which have the potential to reach the earth. Impact experiments have been conducted for several years at the NASA Ames Vertical Gun Range (AVGR) involving terrestrial and extraterrestrial samples [1]. Many asteroids are believed to be highly porous because their densities are considerably lower than the minerals out of which they are formed [2]. Pumice is a very porous material, so it is being used as a sample material to investigate the disruption of such materials. To better understand the characteristics of the rock, the density of the pumice needed to be determined. During cratering experiments at Ames, a low mass of ejecta was noted when pumice samples were impacted. It was also noticed that it takes more energy to disrupt porous targets than to disrupt non-porous targets; this implies that much of the energy goes into compaction of the target [3]. The compression strength of the pumice samples needs to be measured to help make sense of the transfer of energy that happens when the samples are cratered instead of disrupted.

Methods: A sample of pumice was acquired to find density and compression strength. Density was determined based on the standard density equation: $\rho = \frac{m}{V}$. The sample was cut into rectangular pieces averaging a mass of about 1 gram and a volume of about 2 cm³; the same samples were subsequently used to find the compression strength. Ten samples were prepared and measured.

The Brazilian Disc Test is typically used to find the compression strength of various materials. A force is applied to a thin, circular disc until failure; the strength is then found using an equation involving the ratio between the force applied and the diameter and thickness of the disc [4]. Using the rock saw in our lab to cut the samples, a smooth, thin disc was too difficult to replicate consistently for accurate results. Instead, the samples were cut into rectangular pieces. Several attempts were made to find the strength of these rectangular pieces. First a c-clamp and a force sensor were connected to the sample. When the c-clamp was turned it applied a force to the sample being compressed. The results from this method had an error of ~90% when compared to the published value [5]. Next, the sample was set on a table and free weights were stacked on the sample until it crushed. During most measurements using this method, the weights became unbalanced and fell before the sample reached the frac-

ture point. Finally, the sample was set between two smooth, flat metal surfaces and a 10-liter container was placed on top of the metal plates. Water was slowly added to the container until the fracture point was reached and the sample crushed. The container and its water was weighed and used to find the force using $F = m \cdot a$. Using the contact area of the sample and the force calculated from the mass of the container, the compression strength could be calculated using the following equation: $\sigma = \frac{F}{A}$.

Results and Discussion: The first method was not successful because when the c-clamp was turned, the screw took away some of the force being applied so the sensor could not get an accurate reading. The second method ultimately failed because the weights were not balanced, which would cause the sample to crush before the failure point, giving inaccurate results. Compared to the published value of the compression strength of pumice [5], the third method was the most successful. When the error was high, it was because the sample needed an extra container that introduced more error.

Ten samples were measured using the final method. The overall density was 0.538 ± 0.059 g/cm³. This compared with other measures of the density done on the same rock using image processing [6].

Samples 1, 5 and 8 shifted during the measurement of compression strength, making the point at which they crushed unclear, resulting in higher error. After removing these samples from the calculation, the average compression strength was 854 ± 195 kPa.

To better understand the energy transfer in the disruptions, a value for compression strength specific to our samples needed to be found. More measurements of the pumice samples will be made to improve the precision of our value and in the future this method will be used to find the compression strength of different materials.

Acknowledgements: This work was supported by NASA Planetary Geology and Geophysics Program Project Number NNX11AP22G. Support was also provided by the National Science Foundation via the PRISM grant to Alma College. Additional support is provided by Alma College.

References: [1] Lipman M. D. et al. (2010) *Lunar and Planet. Sci. Conf. XLI* #2442. [2] Flynn G. J. et al. (2014) *LPS XLV*, Abstract. [3] Flynn, G. J. et al. (2012) *43rd LPSC*, Abst #1091. [4] Li D. and Wong L. N. Y. (2013) *Rock Mech. Rock Eng.*, 46, 269-287.

[5] Jutzi M. et al. (2009) *Icarus*, 201, 802-813. [6] Strait M. M. (2013) *Met. and Planet. Sci.*, 48, #5286.

Table 1: Density and compression strength of pumice for the ten samples measured. Compression strength for samples 1, 5 and 8 were not used in further calculations. The percent error was calculated in comparison to the literature value of 1000 ± 250 kPa [5].

Sample #	Density (g/cm ³)	Compression Strength (kPa)	% Error
1	0.605	360	63.9
2	0.585	959	4.19
3	0.495	1190	19.1
4	0.453	642	35.7
5	0.473	562	43.6
6	0.566	742	25.6
7	0.561	911	8.7
8	0.618	692	30.7
9	0.551	649	35.1
10	0.477	882	12.8

QUANTITATIVE INVESTIGATIONS OF RELATIONSHIPS BETWEEN TUMULI MORPHOMETRICS AND LAVA FLOW EMPLACEMENT. S. Sangha¹ (sangha@oxy.edu) and S. Diniega², ¹Occidental College, Los Angeles, CA, ²Jet Propulsion Laboratory, California Institute of Technology, Pasadena, CA.

Background: We focus on inflated lava flows found on both Earth and Mars and characterized by a domed, rigid upper crust that has been lifted and insulated by a mobile, fluid interior [1]. This flow morphology forms when a lava flow is allowed to cool, but not completely solidify, so as to retain the fluid interior. Injections of lava from successive events propagate through pathways that offer the least resistance to horizontal flow. As cooling of the fluid interior continues, these subsurface lava pathways narrow, resulting in an increase in internal pressures, obstacles, and abrupt corners. All of these variables contribute to increasing resistance to the horizontal transport of flow, until lava preferentially inflates the rigid outer crust vertically rather than advancing the flow front forward [1]. Localized inflation can form distinctive surface features called tumuli—small-scale positive topographic features ~10 m in width with rounded shapes [2-6]. Such surface features may thus record information about the pathway structure of the lava flow’s fluid interior [Fig. 1] [2-5].

In our broader study, our goal is to develop ways to use tumuli as records of both flow structure on both Earth and Mars [7]. In this presentation, we first aim to justify that tumuli are likely good records of flow structure. In particular, we establish that a strong correlation exists between the observed distribution of tumuli orientation and the general lava flow directions.

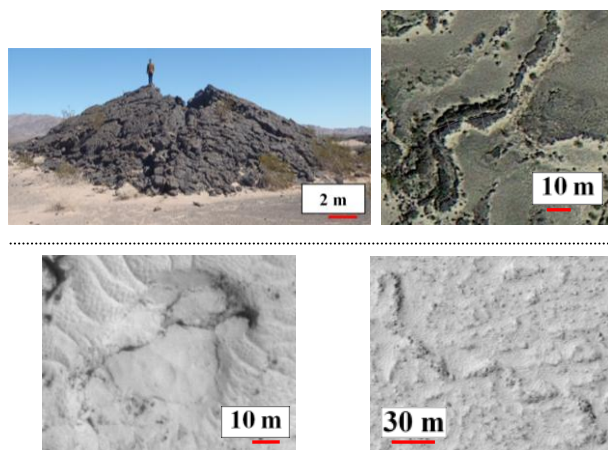


Figure 1. A tumulus from the Amboy Crater Lava field, CA (top left) and a tumulus from the southern edge of Elysium Planitia, Mars taken from HiRISE image PSP_007685_1850 (bottom left). To the right of each of these are images of chains of tumuli atop of lava pathways in each lava field.

Datasets: The Shuttle Radar Topography (Mission) dataset was used for terrestrial flow slope analyses with a vertical accuracy of ≤ 30 m and a horizontal accuracy of ≤ 50 m, while the Mars Orbiter Laser Altimeter (MOLA) dataset was used for Martian flow slope analyses with a vertical precision of ≤ 10 m and a horizontal accuracy of ≤ 100 m. As tumuli are a few tens of meters in size, we use HiRISE images (≤ 50 cm/px) for our Martian survey and Google Earth (≤ 2.5 m/px) for our terrestrial survey. We have compiled the largest interplanetary database of tumuli, with >2400 tumuli through seven fields within the Elysium Planitia region of Mars and >1300 tumuli through six diverse terrestrial fields. We continue to look for more Martian fields through detailed tumuli identification criteria [8].

Results: In this investigation, analyses were limited to flows where we could deduce general and local flow directions from a discernible flow terminus and/or elevation profiles [e.g., Fig. 2]. (A generally decreasing elevation away from the source vent was assumed to be a good approximation for the general flow direction.) We also focused on simple flows (i.e., flows that appeared to develop in one period, versus compound flows). The flow direction then was compared with the aggregated distribution of tumuli orientations [Fig 3].

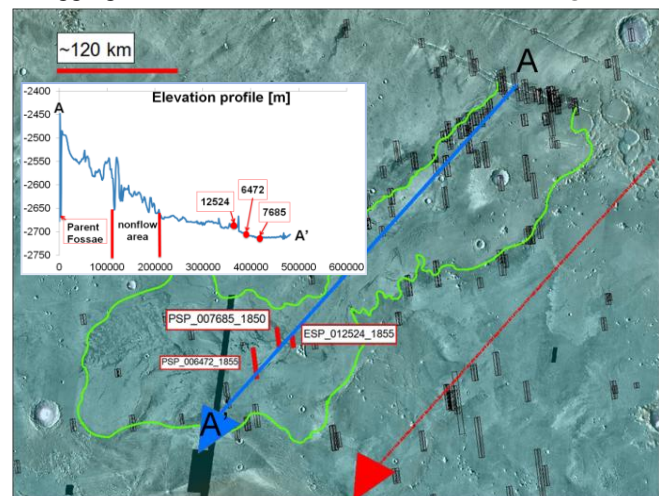


Figure 2. A lava field from Elysium Planitia, Mars with mapped flow margins in green and surveyed HiRISE image ID footprints in red. Inset of elevation profile along apparent flow direction taken from the blue A \rightarrow A' line on the map.

A tumulus' orientation is defined by its long-axis, restricted to the 180° extending in the downflow direction (as one cannot visually distinguish the “front” from the “back”; e.g., tumuli oriented NW/SE are binned together). In all mapped images, the dominant flow direction is indicated by the purple arrow with the “transverse” flow direction roughly perpendicular to the arrow. We find that:

- A. for most flows, aggregate tumuli orientations have two dominant directions; these correlate with the the general flow direction and roughly transverse to the general flow direction [Fig. 3].
- B. while the number of tumuli oriented with the general flow direction increases gradually with distance away from the source vent and towards the flow terminus, the number of tumuli oriented transverse to the general flow direction is relatively consistent [Fig. 4].

Discussion: We are particularly interested in a specific type of simple, *fan-lobe* inflated lava flow within which tube growth occurs primarily in the overall flow direction. However, many bifurcations of the pathways result in transverse spreading directions. Thus, the pathways create a “fan-shaped” flow. Within flows of this type, we expect to find that tumuli long-axis orientations broadly correlate with the field's flow direction, but with a significant secondary population that align with the transverse flow direction. In general, this was observed in seven fields.

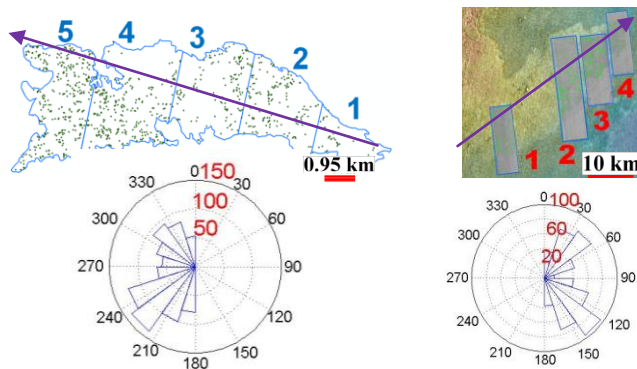


Figure 3. Aggregate tumuli orientation rose diagrams for the 1651-3 Mt. Etna flow (left) and “Field 3” in Elysium Planitia, Mars (right) within mapped flow boundaries.

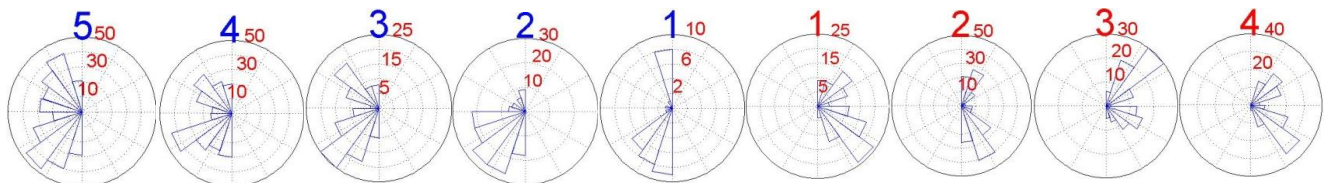


Figure 4. Rose diagrams plots of regions in Fig. 3 maps, numbered in order of increasing distance from the source vent. 1851-3 Mt. Etna Flow, Italy (blue/left) and Field 3 from Elysium Planitia, Mars (red/right).

Only within a few extremely large fields did we not observe tumuli to be oriented with the general and transverse flow. Generally, we think that this is due to a survey bias as, in exceedingly large fields, we measured only a representative population of tumuli that extended along a single margin. Thus, we expect tumuli will only be orientated towards the local flow direction where lava tubes that terminate along the margin dominate and may thus be oblique with respect to the general and transverse flow directions. However, if we completed a survey of an entire field and found tumuli to solely be oriented with the general flow direction (as may be the case in the Nesjahraun lava field) this would suggest that the field is dominated by *finger-lobe flows*. These are a different type of inflated flow whereby lava tubes expand in the general flow direction, without much bifurcation (thus forming a series of “fingers” pointing in the same direction). Within this type of flow, we expect nearly all tumuli to be oriented in the general flow direction [9].

Future Work: In our broader investigations of how tumuli can be used as records of lava flow structure on Earth and Mars, we have found interplanetary similarities in: (1) tumuli morphometrics, (2) trends in tumuli morphometrics through the length of lava flows, and (3) correlations between tumuli orientation and general/local flow direction. Based on these results, we aim to clearly define ways in which tumuli can be used as direct records of lava flow structure in order to interpret emplacement conditions and pre-erosional flow extent.

References: [1] Keszthelyi (2000) *JGR* 105, 15027-49. [2] Hon et al. (1994) *GSA* 106, 351-70. [3] Calvari & Pinkerton (1999) *J. Volcanol. Geotherm. Res.* 90, 263-80. [4] Anderson et al. (2012) *Bullet Volcanol.* 74, 931-46. [5] Walker (1991) *Bullet Volcanol.* 53, 546-58. [6] Rossi and Gudmundsson (1996) *J. Volcanol. Geotherm. Res.* 72, 291-308. [7] Sangha et al. (2013) *GSA*, 45, A7, 239. [8] Diniega et al. (2012) *LPS XLIII*, Abstract #2537. [9] Duncan et al. (2004) *J. Volcanol. Geotherm. Res.* 134, 173-87.

DISSOLUTION OF NONTRONITE IN BRINES: IMPLICATIONS FOR HABITABLE ENVIRONMENTS ON MARS R.E. Schofield¹, M. H. Steiner¹, E. M. Hausrath¹, ¹University of Nevada, Las Vegas 4505 S Maryland Pkwy, Las Vegas, NV 89154, schofi35@unlv.nevada.edu.

Introduction: Clay minerals form in the presence of water, and thus are key indicators of past water activity. Clay minerals may also hold the key to the beginning of life due to their ability to preserve organic matter and hold water and various elements within their mineral structure [1]. Clay minerals could also host chemical processes that contribute to the origin of life, such as forming components of RNA [2].

Nontronite is an iron rich clay mineral found both on Earth and on Mars, as documented by the Mars Reconnaissance Orbiter and Mars Opportunity Rover [3, 4]. Nontronite is found on Mars in vastly ancient terrains (> 3 billion years)[3] and thus it is likely that nontronite has been altered since its formation.

Waters on Mars may have been very concentrated brines [5], and since brines and dilute solutions have very different implications for life, dissolution experiments were performed in both dilute solutions and brines.

Studying the dissolution of nontronite will help interpret alteration conditions on Mars, and possibly suggest if there could have been or could be habitable environments on Mars.

Methods:

Materials: The mineral used, NAu-1, is green nontronite from Uley Mine, South Australia, from the Source Clays Repository (Figure 1)[6]. To obtain the desired 45-150 μm size fraction, an agate mortar and pestle was used to reduce the particle size, with subsequent sieving until nearly 30 g of the desired size fraction was sieved. The desired size fraction was then cleaned by gently

agitating and sonicating in ethanol several times at 3 minute intervals, decanting the supernatant each time until the supernatant was clear [7-10].

Two solutions were made for batch dissolution experiments. A dilute (0.01 M) NaCl solution was prepared by mixing 0.5844 g of high purity NaCl in 1 L of DI water. The second solution, a saturated (23.8%) NaCl solution, was prepared by mixing 300 g of high purity NaCl in 736 ml of DI water [11]. Two liters of each solution were made (two 1 L bottles for each solution) in order to simplify the pH adjustment process. Each 1 L bottle was adjusted to the desired pH of 3 or 5 using HCl.

Experimental Setup, Analyses, and Calculations: Dissolution experiments were carried out in duplicates at pH values of 3 and 5. A total of 12 batch reactor vessels were used in this experiment. Each 250 ml LDPE vessel contained 0.5 g of washed nontronite and 200 ml of one of the prepared solutions (Figure 2). The 12 batch reactor vessels were placed in an agitated water bath at a constant temperature of 25°C (Figure 3).

Samples were collected from the vessels every hour for the first 2 days, and once a day for 3 days thereafter. Dissolution rates were measured by the batch initial rate method and samples were analyzed for calcium by flame atomic absorption, and the molal release rate of Ca calculated using the equation [12, 13]:

$$m = m_{t-1} + (c_{(t)} - c_{(t-1)})V_{(t-1)} \quad (1)$$

Results:

The concentration of calcium increases over time in dilute solution. Establishing a

confident release rate in saturated solution was difficult, but overall the concentration appears to increase as well. This difficulty may be due to an exchange of Ca in the interlayer of the mineral with Na in the solution. Our results also indicate that pH had little effect at high salt concentrations in solution.

Conclusions and Future Work:

The release of calcium from nontronite increased over time, and is enhanced in more acidic conditions in dilute solutions. In saturated solutions there may be cation exchange of the Na in the solution with the Ca in the interlayer site.

On Mars, brines may be significantly affected by interaction with clay minerals, and clay minerals affected by interaction with brines.

In future work, , Si and Fe will be analyzed to determine dissolution rates from the tetrahedral and octahedral sites, respectively, which will be less affected by cation exchange than the interlayer site.

Acknowledgements: Funding for this research was provided by the Microbiology REU funded by NSF Grant DBI REU 1005223. This research was also funded by the NASA Mars Fundamental Research Program, and the UNLV Faculty Opportunity Award.

We would also like to thank Dr. Regner for his support and assistance, Chris Adcock and Megan Elwood Madden for helpful information that greatly improved this research, Minghua Ren for EMIL access and use of the SEM, Seth Gainey for his useful information and knowledge of nontronite, and Valerie Tu for her support.

References: [1] McKeown, N. K., et al. (2009) *Journal of Geophysical Research E: Planets* 114(11). [2] Fernández-Caliani, J., et al. (2004) *Clays and Clay Minerals* 52(1),

106-114. [3] Thomson, B. J., et al. (2011) *Icarus* 214, no. 2, 413-432. [4] Poulet, F., et al. (2005) *Nature* 438, no. 7068, 623-627. [5] Bishop, J. L., et al. (2013) *Planetary and Space Science* (0). [6] Keeling, J. L., et al. (2000) *Clays and Clay Minerals* 48(5), 537-548. [7] Bickmore, B. R., et al. (2001) *American Mineralogist* 86(4), 411-423. [8] Dogan, Meral, A., et al. (2007) *Clays and Clay Minerals* 55, no. 5, 534-541. [9] Hausrath, E. M. and S. L. Brantley (2010) *Journal of Geophysical Research E: Planets* 115(12). [10] Miller, M. A., et al. (2012) *Clays and Clay Minerals* 60(6), 616-632. [11] Pritchett, B. N., et al. (2012) *Earth and Planetary Science Letters* 357-358, 327-336. [12] Welch SA, Ullman WJ (2000) *Chemical Geology* 167, 337-354. [13] Rimstidt, J. Donald, and William D. Newcomb. (1993) *Geochimica et Cosmochimica Acta* 57, no. 9, 1919-1934.

PATERAE ON IO: COMPOSITIONAL CONSTRAINTS FROM SLOPE STABILITY ANALYSIS.

T. Slezak^{1,2}, L.P. Keszthelyi¹, C. Okubo³, D.A. Williams², ¹Astrogeology Science Center, U. S. Geological Survey, 2255 N. Gemini Dr., Flagstaff, AZ 86001; ²School of Earth & Space Exploration, Arizona State University, Tempe, AZ 85287; ³Astrogeology Science Center, U. S. Geological Survey, 1541 E. University Blvd., Tucson, AZ 85721

Introduction: Observations from the *Voyager*, *Galileo*, *Cassini*, and *New Horizons* missions have greatly advanced our understanding of Io's geology, however many questions remain unresolved. Persisting from *Voyager*'s initial observations is the dispute regarding the relative roles of sulfurous and silicate materials in Io's crust. This study provides new compositional constraints at scarps on Io, using numerical slope stability modeling to gain new insight into the roles of such materials in subsurface processes by testing the Jaeger and Davies (2006) [1] model for Io's crust.

Previous Work: Clow and Carr [2] conducted slope stability analysis of scarp formations on Io using the Mohr-Coulomb failure criterion, and our study seeks to replicate the methodology used, but differs in its capabilities with 30+ years of technological advancement, and a significantly improved Io dataset. Preliminary results of this study were provided by Keszthelyi et al. (2010) [3] and yield the basis from which this study was done.

Methodology: In order to characterize a compositional profile for the observed, 1-4-km-tall, near-vertical, scarps on Io, observed structural characteristics allow compositional limitations to be applied. An analysis of the supporting force required to maintain such scarps constrain the mechanical properties of the material(s) of which a formation is comprised. Maintaining consistency with previous work [e.g., 3], we employ the Slide software [4] for numerical slope stability modeling and the Mohr-Coulomb and Bishop simplified failure criteria used therein.

Model parameters vary slope angle θ and material density ρ , against an assumed cohesion σ , and values for internal friction ϕ are assigned up to a Factor of Safety (FS) = 1. A Factor of Safety less than 1 indicates a tendency for slope failure, whereas a Factor of Safety greater than 1 indicates that slope failure is unlikely. The models equipped in this study have assumed isotropy, representing uniformity in material particle characteristics at static temperature. It is imperative to simplify the parameters of our results prior to the introduction of anisotropic elements to later quantify isothermal boundaries.

Due to the large amount of tidal stress Io incurs from Jupiter, incorporation of dynamic stress (e.g., seismicity) into some models provides a representation of the iquakes that must occur as a result of Io's flexing lithosphere and voracious volcanic flux. The dy-

amic loads presented in the models are prescribed by a pseudostatic horizontal ground acceleration acting in the out-of-slope direction [5] related to a dimensionless seismic coefficient. In terms of Io, this seismic coefficient effectively describes the maximum horizontal acceleration due to iquakes as a fraction of the acceleration due to gravity on Io's surface ($g_{Io} = 1.796\text{m/s}^2$).

Results: Work conducted thus far now provides constraints at both static and dynamic conditions for material (mechanical) properties ranging from snow to SO_2 solid to mafic rocks.

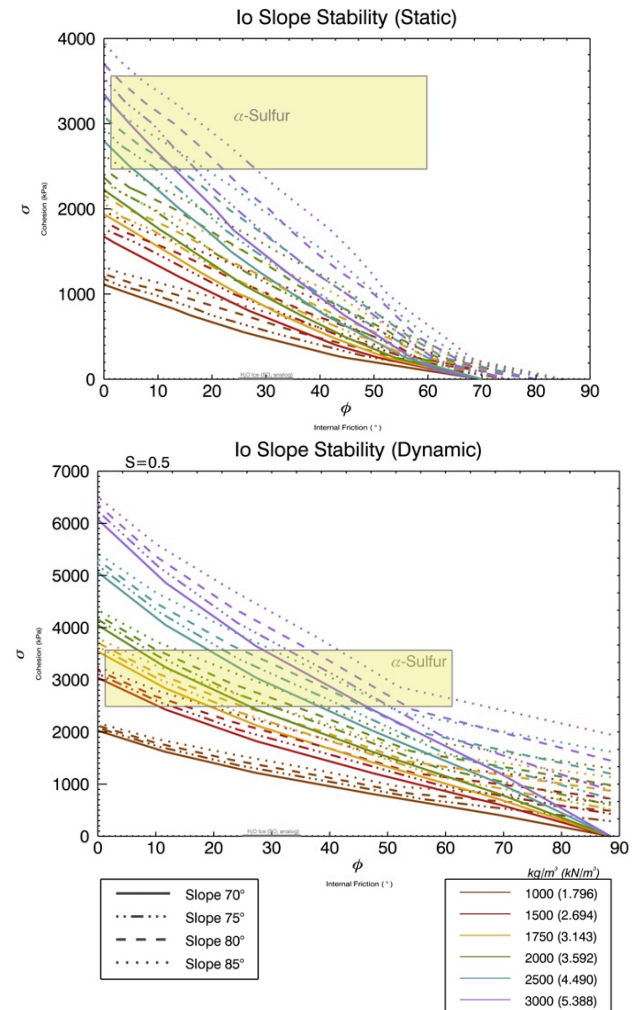


Figure 1. Plots of modeled results corresponding to a Factor of Safety = 1 under static and dynamic conditions at various steep-angle slopes for densities spanning tested compositional end-members.

Cohesion values are expected to be 10-40 MPa for mafic rocks [6], 3 MPa for (orthorhombic) sulfur [2] and snow (analogous to SO₂ frost) 1-10 kPa [7]. Values of internal friction for most terrestrial rocks range from ~25°-35° [8] and ~32°-52.7° for Martian soil [9]. Clow and Carr [2] provide internal friction coefficients for ductile and brittle SO₂.

Figure 1 displays the threshold between allowed and disallowed mechanical properties in the modeled 3-km-tall scarp, under static and dynamic conditions respectively. Materials with mechanical properties above the threshold lines given in the plot denote materials that are viable constituents representative of the materials that could allow such scarps to persist. Materials with mechanical properties placed on the plot below a threshold line indicates that the material will result in slope failure and collapse under prescribed conditions. Pale yellow boxes describe the mechanical property parameters of α -sulfur, mafic rock far exceeds maximum cohesion values represented by the plot, and snow falls below all threshold lines.

We find that α -sulfur is at the threshold of failure only for unrealistically high densities. When seismic shaking is added in the model, sulfur remains plausible, but is consistently at the threshold for failure. Even moderately weathered mafic rock is capable of accommodating the supportive force for the scarp and is able to withstand mild-quake loads. The plausibility of solid sulfur dioxide remains largely unknown as its mechanical properties are largely unconstrained, however the modeled density of solid sulfur dioxide (2000kg/m³ [10]) borders the mechanical property capacity of α -sulfur in both static and dynamic conditions at approximately the same magnitude, possibly an indication of diagenesis.

In summary, slope stability does not provide a definitive conclusion about the composition of Io's upper crust. However, if the scarps on Io are actively collapsing (i.e., are right at the threshold of failure), a sulfur-rich composition may be the most likely.

Future Work: While photogrammetry derived scarp height estimates [11] are sufficient in establishing end-member limitations, more realistic constraints provided via DEM would greatly improve the accuracy of these results as the accuracy in elevation dictates the translational dependency of our model. Further modifications to be made to the variables already in play include modification of scarp height and affixing various other seismic factors to the model. While general orientations of trending lines in manipulation of these variables may be established a priori, successive definition will allow the subtleties of model variables to be exploited and further explored. Additionally, the incorporation of anisotropic elements into the model is a

necessary evolution in the course of determining if our empirical results and the Jaeger and Davies (2006) [1] model are correlative.

References: [1] Jaeger W. L. and Davies A. G. (2006) *LPS XXXVII*, Abstract #2274. [2] Clow G. D. and Carr M. H. (1980) *Icarus*, 44, 268-279. [3] Keszthelyi, L.P., Jaeger, W.L., Okubo, C., (2010). *LPS XXXI*, Abstract #2244. [4] Slide 5.0, Rocscience Inc. 2003, Slide Version 5.0 - 2D Limit Equilibrium Slope Stability Analysis. www.rocscience.com, Toronto, Ontario, Canada. [5] Okubo, C.H., Tornabene, L.L., Lanza, N.L., 2011. Constraints on mechanisms for the growth of gully alcoves in Gasa crater, Mars, from two-dimensional stability assessments of rock slopes. *Icarus* 211, 207–221. [6] Lockner, D.A., 1995. Rock failure, AGU Reference Shelf. American Geophysical Union, Washington, D. C., pp. 127–147. [7] Shapiro, L.H., 1997. Snow Mechanics. [8] Davis, George H., Stephen J. Reynolds, and Chuck Kluth. *Structural Geology of Rocks and Regions*. Hoboken: Wiley, 2012. Print. [9] ElShafie, A., Chevrier, V.F., Dennis, N., 2012. Application of planetary analog mechanical properties to subsurface geological investigations. *Planetary and Space Science* 73, 224–232. [10] Milazzo, M.P., Keszthelyi, L.P., McEwen, A.S., 2001. Observations and initial modeling of lava-SO₂ interactions at Prometheus, Io. *Journal of Geophysical Research: Planets (1991–2012)* 106, 33121–33127. [11] Radebaugh, J., Keszthelyi, L.P., McEwen, A.S., Turtle, E.P., Jaeger, W., Milazzo, M., 2001. Paterae on Io: A new type of volcanic caldera? *Journal of Geophysical Research* 106, 33005–33020.

Acknowledgements: This research was funded by National Science Foundation Grant AST-1004107. Additionally, the authors wish to acknowledge and thank the NAU Physics and Astronomy REU program, the United States Geological Survey Astrogeology Science Center, and the Ronald Greeley Center for Planetary Studies (the NASA Regional Planetary Information Facility (RPIF) at ASU) .

SHARAD REFLECTORS IN UTOPIA PLANITIA, MARS CONSISTENT WITH WIDESPREAD, THICK SUBSURFACE ICE. C.M. Stuurman¹, G.R. Osinski¹, T.C. Brothers², J.W. Holt², M.Kerrigan¹,¹Centre for Planetary Science and Exploration/Dept. of Earth Sciences, University of Western Ontario, London, ON, Canada ²University of Texas Institute for Geophysics, University of Texas at Austin, Austin, TX, USA

Introduction: Characterising the extent and distribution of sub-surface ice in the middle latitudes of Mars is an ongoing endeavour, with applications to both paleoclimate and future missions. Utopia Planitia has been posited as a potentially ice-rich area by climate models [1], gamma-ray spectrometer results suggestive of high hydrogen concentrations [2], and due to the high density of putative periglacial and glacial landforms [3-4].

The SHARAD (SHARAD) instrument on the Mars Reconnaissance Orbiter is a radar sounder which transmits a 15-25 MHz chirped pulse. The data is recorded in the time delay and can be used to map and characterize Mars' subsurface through analysis of relative dielectric constants at depth [5].

SHARAD has identified several features in the mid-latitudes of Mars that are indicative of ice-rich subsurface material. Analysis of lobate debris apron features in the mid-latitudes revealed a dielectric constant consistent with nearly pure water ice, both in the northern and southern hemispheres [6-7]. Pedestal craters in the mid-latitudes have also yielded results suggestive of water ice composition [8]. A massive, radar-transparent layer in Arcadia Planitia has also been discovered, and results suggest the composition of material overlying the reflecting interface is nearly pure water ice [9].

This study represents part of an ongoing SHARAD investigation linked to mapping of potential periglacial and glacial landforms in Utopia Planitia. We present the discovery of a subsurface reflecting interface in SHARAD data over western Utopia Planitia. The interface spans approximately 400,000 square kilometers. This work discusses the plausibility of an ice-rich composition for the material overlying the reflectors using dielectric analysis and morphological evidence.

Utopia Planitia: The Utopia Planitia region is a circular depression ~3,300 km in diameter centred at 49.7° N and 118.0° E, thought to be the result of an impact event early in Mars' history. Motivated by obliquity-driven atmospheric deposition, the depression has acted as a depocentre for infill material composed of a mixture of ice and dust [9].

Recently, a revised map of Utopia Planitia has been proposed. This work identifies a new unit ABp which is characterized by the presence and dominance of periglacial landforms such as polygonal terrain, scalloped depressions, and debris flow features [10]. Near-

ly all reflectors found in this work are contained within periglacial unit ABp (Figure 2). An outlier occurs within Vastitas Borealis marginal unit ABvm.

SHARAD Observations: The mapped interface is located in southwestern Utopia Planitia, and spans from 75°-90° E in longitude and 40-50° N in latitude. Several hundred SHARAD tracks were analyzed, and a total of 88 tracks exhibited verifiable reflectors. Some reflecting interfaces were anomalously far from the bulk of the reflectors, and coverage bias in SHARAD may, in part, explain the gaps in the reflecting unit. Noise in the data and geological variation are also possible explanations for the gaps.

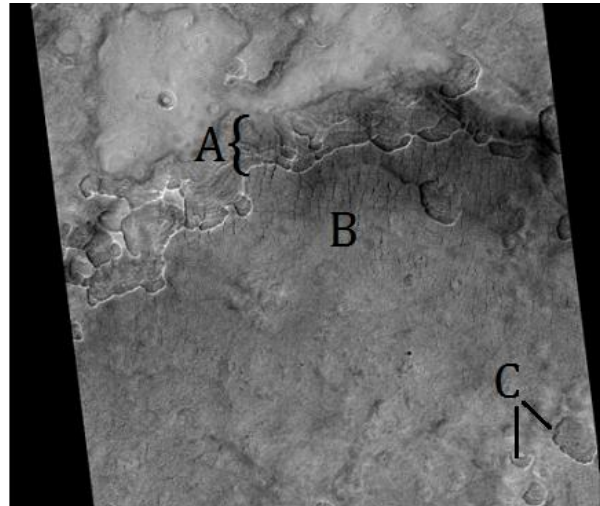


Figure 1: HiRISE image ESP_026385_2225. A scarp within unit ABp exhibiting (A) layering, (B) large polygons, and (C) scalloped depressions. Many similar features were found in SHARAD reflecting unit; reflections often terminate at edge of scarps. HiRISE image is 6 km wide.

Many layered scarps (Figure 1) are found within the reflecting unit; however, some regions are more continuous than others. In cases where reflections are found in the vicinity of a scarp, they consistently terminate where scarps expose a lower unit. This suggests that the layered deposits are the source of the SHARAD reflectors. The heights of the scarps range from 85 to 110 m relative to their bases. Using time delays derived from SHARAD radargrams, relative dielectric constants of 3 to 4.5 have been calculated for these thicknesses. These dielectric values are consistent

with pure to relatively pure water ice. This interpretation is supported by the prevalence of periglacial morphologies throughout the region [10].

Discussion/Future work: The reflecting interface strongly correlates with recent ice accumulation models from [1] (Figure 3). Results from this model suggest that Utopia Planitia has the highest ice accumulation budget of the northern hemisphere, and the reflectors found in this work lie within the 10-14 mm/yr range.

Dielectric analysis, morphological analysis, and ice accumulation models consistently support the hypothesis that the material overlying the Utopia Planitia SHARAD reflector is composed of pure to nearly pure water ice.

By creating a database of scarp elevations across the reflecting unit and the associated radargram time delays at each location, a simple inversion for the average relative dielectric constant should be possible. This will help to constrain the dielectric constant in a comprehensive and quantitative manner.

Possible relationships between the reflecting interface found in this work and the expansive reflecting

unit found in Arcadia Planitia will be investigated further. More mapping to the east and west of the reflecting unit is to be completed, as there is evidence that the reflectors extend further than what is currently mapped.

References: [1] Madeleine, J.B. et al. (2009) *Icarus*, 203, 390-405. [2] Boynton, W.V. et al. (2002) *Science*, 297, 81-85. [3] Lefort, A et al. (2009) *JGR*, 114, E04005 [4] Séjourné, A. et al. (2011) *Planetary and Space Science*, 59, 412-422. [5] Seu, R. et al. (2007) *JGR*, 112. [6] Holt, J.W. et al. (2008) *Science*, 322, 1235. [7] Plaut, J.J. et al. (2009) *GRL* 36, L02203. [8] Nunes, D.C. et al. (2011) *JGR*, 116 [9] Head, J.W. et al (2003) *Nature*, 426, 797-802. [10] Kerrigan, M.C. (2013) *MA thesis, U of Western Ontario -- Electronic Thesis and Dissertation Repository*. 1101.

Acknowledgements: This work was supported by the Natural Sciences and Engineering Council of Canada. We thank the SHARAD team for data acquisition and processing.

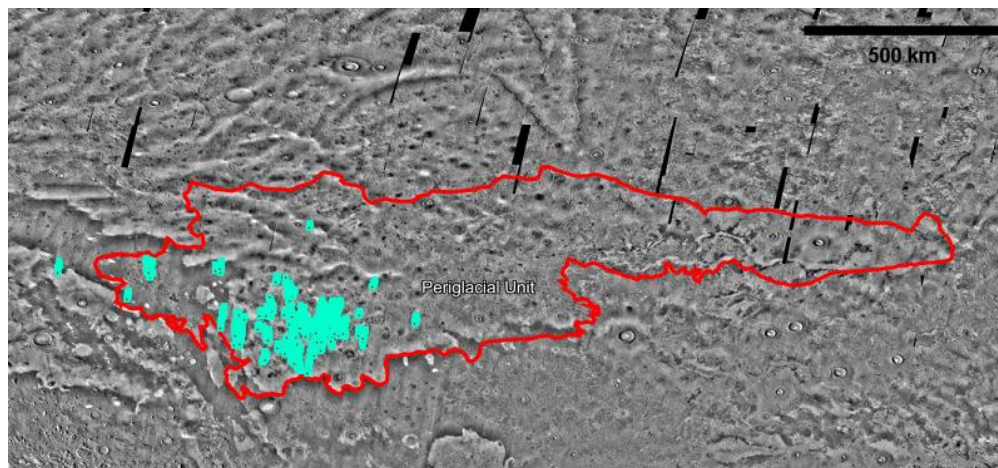


Figure 2: Map of reflector locations (blue) over Kerrigan's (2013) periglacial unit ABp on a THEMIS daytime IR mosaic basemap.

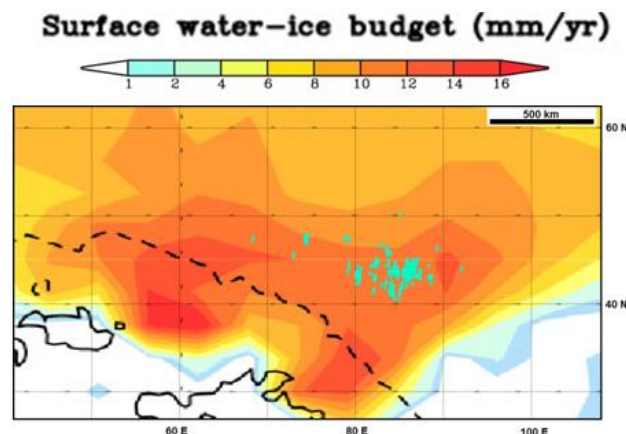


Figure 3: Correlation of reflecting unit locations (blue) with ice accumulation model results. Modified from [1].

Biosynthesis of the Standard Amino Acids of the Genetic Code

¹Kerian Trice, ¹Onyilagha, J. and ²Freeland, S.

¹University of Arkansas Pine Bluff, 1200 North University Drive, Pine Bluff, AR 71601

²Interdisciplinary Studies, University of Maryland Baltimore County, MD 21250

Correspondence to: keriantrice@yahoo.com

Abstract

Three main theories have been advanced in order to explain the emergence of the 20 standard amino acids of the genetic code. These theories include: *The Stereochemical Theory* – established that codon assignments of amino acids are based upon physiochemical affinity between amino acids and nucleotides, *The Adaptive Theory*—based upon natural selection shaping the genetic code which biochemically assigned similar amino acids and codons, and *The Co-evolution Theory*— based on idea that the genetic code coevolved with amino acid biosynthetic pathways, and that the division of codons for precursor amino acids have been redistributed to translate for product amino acids. This study explores the assertions of *The Co-evolution Theory* proposed by Wong, in relation to new available data. It is hypothesized that recent data will give better understanding of the pathways through which the standard amino acids of the genetic code evolved. This present study will allow us to understand whether metabolic pathways found in living organisms are an accurate guide to ancient evolutionary events. Recent information from KEGG & MetaCyc databases were used to construct new amino acid pathways. Although a useful theory, however our results show some that levels of discrepancy exist between the two assertions of *The Co-Evolution Theory* and available new data.

DON'T GET BURNED! PROTECTION FROM ICME RELATED SEP EVENTS IN INTERPLANETARY SPACE. S. E. Vogler¹, ¹Lamar University, Beaumont, TX 77710, sevogler@my.lamar.edu.

Introduction: One of the most significant challenges regarding interplanetary travel, facing the scientific community today is space radiation. Specifically, high energy particles contained in coronal mass ejections (CMEs) that have traveled a sufficient distance through the interplanetary medium to become Interplanetary counterparts of Coronal Mass Events (ICMEs).

Preliminary Designs: The purpose of this literature review is to determine the necessity and relevance of a new method for ICME detection and radiation shielding on interplanetary spacecraft. The proposed method consists of a three part warning system and a six-part shielding system.

ICME Warning System. The three part warning system is designed to detect ICMEs with 30 or more spacecrafts at approximately 0.723 AU, sharing Venus' orbit Each of these crafts would relay a craft-specific signal using a magnetic dipole antenna or similar device.

An interplanetary spacecraft would have two antennas, on opposite sides of the spacecraft's body. These antennas would have detectors suitable for the transmitted signals, in an X pattern. The signal from the detection spacecraft would be perceived by any interplanetary craft in a line-of-sight, with a geometric time delay relative to signals from any of the other 30 spacecrafts that detected the CME.

The interplanetary spacecrafts' onboard computer would then analyze the signal to determine the craft that sent it, correlate that information received from all the craft signals, and determine the time of impact for the edge of the ICME. The minimum time frame that any one craft would have to implement the safety protocols is estimated at 4 hours.

Spacecraft Safety Protocols. The six-part shielding system would start with a warning to the onboard crew of automated procedures to take effect after a certain countdown. The countdown should be stopped in the event of an extra vehicular activity (EVA) in progress, or other circumstance that makes the protective protocols detrimental to life. If the countdown is not stopped, then the automatic process described below will be initiated. If the countdown is stopped, the processes can be resumed by the crew when the EVA is complete and the crew is prepared for the events to follow.

Once the countdown has finished or the automated processes have been initiated by the crew, the onboard computer will start preparations for the oncoming

ICME by shutting down all non-essential systems. This includes personal communication systems, hot food preparation, any experiments that are onboard and would not be irreparably damaged by a shutdown and reboot, etc. This catalogue of systems should be maintained by a specific member of the crew and/or mission control at all times.

After the systems have been shut down, a magnetic field surrounding the craft will be brought online. The poles of the spacecraft's magnetic field will pass through a liquid, sufficient in density and volume to diminish the energy of the particle radiation, in a similar way that the Earth's Ionosphere does in correlation with the cusp region of the Magnetosphere.

By this time, the computer, mission control, and flight commander (as he is responsible for the safety of the crew and mission) will have determined the relative strength of the ICME and the duration of required shielding. If necessary, the crew members will be directed to more interior quarters with additional shielding.

Minutes before the onset of the ICME, additional systems may be brought down. These systems will be determined by mission control and the flight commander. At the same time, detection systems for the ICME mounted on the exterior surface of the spacecraft and inside the crew cabin will come online. These systems are meant to monitor the levels of radiation to assess when the ICME has passed. They will also store data for analysis to improve future systems.

When the onboard computer believes the event is over, an automatic communication will be initiated between the crew and mission control. When the 'all clear' is received all systems will come back online.

Methods: Verifying the necessity of these designs began with "Coronal Mass Ejections: an introduction", a book by Timothy Howard [1]. The process then moved onto literature review of sources from NASA and scholarly and professional journals. A significant effort was put towards the derivation of relevant equations, and adapting them to sustain our hypothesis.

Findings: ICMEs begin their life as CMEs. When a CME has reached about 50 solar radii (R_{\odot}) it has interacted with the interplanetary medium to such an extent as to change its velocity and possibly change its composition. An ICME's kinetic direction is also more strongly controlled by fluid dynamics of the solar wind verses the magnetic forces from the Sun [1]. Venus is approximately 150 R_{\odot} away from the sun, so all space-

craft that would benefit from the preliminary designs would come into contact only with ICMEs.

ICMEs do share the structure of their CME counterparts. The leading edge is followed by a cavity. The cavity is surrounding the filament. The brightness of the leading edge and the filament are caused by the scattering of white light due to free electrons [1]. The darkness of the cavity is then logically an indication of a lower electron density.

A CME can have any angular size but is typically several tens of degrees [1]. In 2010 Dr. Tony Phillips of NASA reviewed, in his article *Solar Storms can Change Directions, Surprising Forecasters*, the work done by Byrne et al. He summarized how CMEs can have their direction changed by the solar wind, and the solar magnetic field. They are deflected from high latitudes and turned back toward the ecliptic plane [2]. The interactive video imbedded in Dr. Phillip's article also showed the shape of the CME as essentially a projection against the solar "surface" [2].

CMEs can travel at speeds greater than 4000 km/s but usually travel at between 400 and 1000 km/s. ICMEs accelerate or decelerate to match the velocity of the solar wind through which they travel, creating a front shock wave, and travel at a constant velocity at distance from the sun of more than 0.3 AU [1,3]. The ambient solar wind travels at about 400 km/s [4] and the Solar Energetic Particles (SEPs) related to ICMEs can travel up to 239,834 km/s (0.8 c) [5].

When a CME forms with a corresponding solar flare, SEPs gather behind the shock front of the CME. Then they travel with the CME behind that shock wave [6]. SEPs can reach Earth anywhere from 30 minutes to 24 hours after leaving the Sun, while CMEs take 1-4 days [6]. Therefore, SEPs can travel ahead of the shock wave.

The threshold energy to pass through human tissue is about 10 MeV [6]. Therefore, SEPs are so dangerous because they have energies from keV to GeV [5].

There are currently nine spacecraft functioning that record measurements used in CME research [1]. Out of these, the Solar Dynamics Observatory (SDO), Solar Heliospheric Observatory (SOHO), and Solar Terrestrial Relations Observatory (STEREO) seem to me to be the most used. The Japanese plan to launch Solar-D in the 2020s, and this spacecraft will provide the first look at the sun from outside the ecliptic. (The Joint Solar-C Assessment Committee decided to implement Solar-C's Plan A as Solar-D.) [7]

A team from Trinity College Dublin maintains a website which daily reports a statistical assessment that solar flare events could occur in any specific region of sunspot activity [8]. Montana State University has been

working on a method to determine the locations on the solar surface from where a CME might originate [9].

Current Radiation shielding ideas for long duration interplanetary missions include methods such as magnetic fields, being researched under NIAC grants [10], and regolith shielding, like the work done at the Georgia Institute of Technology [11].

Conclusion: The preliminary designs contain an overall acceptable solution to current radiation dangers. The detection system will need to be modified to detect SEPs arriving in advance of a CME, and the window of response for interplanetary craft will be significantly shorter for those events. Also, more research will be needed to refine the placement of the detection spacecraft, to ensure that a CME or SEP does not travel around, over, or under them. In general, this is an acceptable starting place for an efficient system design.

Acknowledgements: I would like to thank Dr. Cristian Bahrim for his advice and support in writing this paper.

References: [1] Howard, T. (2011) *Coronal Mass Ejections: an introduction*, Springer: New York, 4-6. [2] Phillips, T. (2010) *Solar Storms can Change Directions, Surprising Forecasters*, NASA Science: Science News, 2/19/2014 Online. [3] Démoulin, P. (2010) *Interaction of ICMEs with the Solar Wind*, AIP Conference Proceedings 1216, 329-334. [4] Hathaway, D. (2012) *Solar Physics: Solar Structure: The Solar Wind*, NASA/Marshall Solar Physics, 2/20/2014 Online. [5] Department of Physics and Astronomy (2014) *Solar Energetic Particles*, University of Delaware 2/20/2014 Online. [6] Spence, H. (2010) *Energetic Particles, Radiation Effects, and Manned Spaceflight*, Heliophysics Summer School Slides, 2/20/2014 Online. [7] ISAS/JAXA SOLAR-C Working Group (2012) *The Next Space Solar Mission: Solar-C*, National Astronomical Observatory of Japan, 2/20/2014 Online. [8] Gallagher, P. (2014) *Flare Prediction System*, www.SolarMonitor.org, Trinity College Dublin, 2/20/2014, Online. [9] McKenzie, D. (1999) *Coronal Mass Ejection Prediction Page: "S" Marks the Spot!*, 2/20/2014 Online. [10] Hoffman, J. et al. (2005) *Use of Superconducting Magnet Technology for Astronaut Radiation Protection: Final Report for NIAC Phase I Contract CP 04-01*, NIAC, 2/20/2014 Online. [11] Globus, A. (1995) *Problem Two: Radiation Shielding*, GA Tech, 2/20/2014 Online.

BALLISTIC CASCADING AS A FORMATION MECHANISM FOR LUNAR COLD SPOT CRATERS: CONSTRAINTS ON THE IMPACT PROCESS FROM DIVINER THERMAL MEASUREMENTS. C. E. Watkins¹, P. O. Hayne², J. L. Bandfield³, and the Diviner Lunar Radiometer Science Team ¹St. Olaf College (watkinsc@stolaf.edu), ²Jet Propulsion Laboratory, California Institute of Technology (Paul.O.Hayne@jpl.nasa.gov), ³Space Science Institute.

Introduction Cold spots are a class of fresh impact craters recently revealed by their unusual thermal signatures in Diviner Lunar Radiometer data [1, 2, 3]. Though the details of their origins remain unknown, the near-crater deposits can be explained by a laterally propagating granular flow created by impact in the lunar vacuum environment [3]. Further from the source crater, at distances of 10–100 crater radii, regolith surfaces appear to have been “fluffed-up” without the accumulation of significant ejecta material. Our hypothesis is that these features form by a ballistic collisional cascade of ejecta particles. We utilized Diviner nighttime temperature data to derive near-surface thermal inertia profiles that can be used to characterize the physical properties of the regolith within the cold spots and test the formation hypothesis.

Characterization of Observed Cold Spots: Nighttime regolith cooling data from Diviner can be accurately fit [4] with exponential depth profiles of both conductivity and density, ρ , with the form:

$$\rho(z) = \rho_0 - (\rho_0 - \rho_s)^{-z/H},$$

where ρ_s and ρ_0 are the density at the surface and at depth $z \gg H$, respectively. The parameter H has units of length, and characterizes the thickness of extremely low thermal inertia regolith in the upper ~10 cm [5]. Larger H -values indicate a lower density regolith.

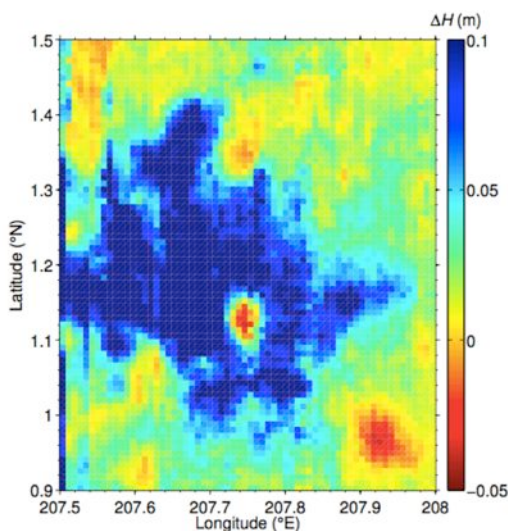


Figure 1: Example map of the upper regolith thickness parameter H .

From the extensive Diviner dataset, we generated 128 pixel-per-degree maps of H , and collected radial profiles of this parameter (Fig. 1). We were particularly interested in whether or not the cold spot radial profiles follow a consistent power law, which could be used to constrain formation models. For example, if the cold spots represent emplaced ejecta material, the thickness $H(r)$ might follow a similar distribution to the canonical power law relation for ejecta thickness,

$$t(r) = t_0 (r/R_c)^{-\beta}$$

where r is distance from the crater rim (radius R_c), and β (≈ 3) is derived from lunar crater data [6].

We selected 10 equatorial cold spot craters of simi-

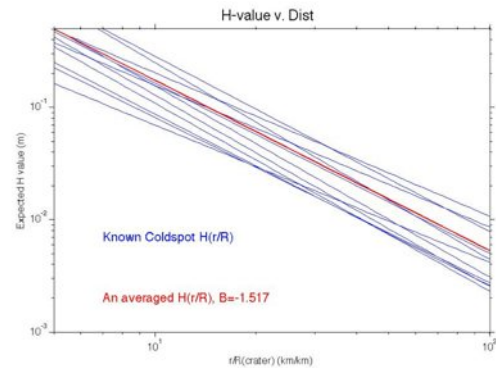


Figure 2: Log-log plot of ΔH vs. distance from crater rim for 10 equatorial cold spots (blue lines), along with the average power law fit of $\sim 3/2$ (red line)

lar size where observational artifacts from slope features have the least effect on the H -parameter calculation from Diviner thermal data. Figure 1 shows an equatorial cold spot map of ΔH , which is the difference from typical lunar surfaces. The pattern of a small warmer (negative ΔH -value) region surrounding the crater is indicative of the effects of small rocks and debris, which offset the H -parameter calculations of thermal inertia. This near-crater rocky region of regolith limited the search for power law attributes of the H -parameter to a more distal ~10 to ~50 crater radii, as farther than ~50 crater radii the cold spot signature dropped off precipitously. Each of the cold spot ΔH maps was fitted with a basic power law equation, $\Delta H(r) = A(r/R_c)^{-B}$. In the regions of interest for each cold spot, we found that the thickness parameter fol-

lows the power law $H \sim (r/R_c)^{-3/2}$. In fact, the results indicate a consistent value of B ($B = 3/2 \pm 0.2$), and a larger variance in A (Figure 2). The variance in the A term is not directly linked to crater size. We used ultraviolet “optical maturity” [7] to check whether this parameter correlates with relative crater age, but again did not observe a strong trend.

Modeling: Energy balance provides a way of testing cold spot formation models, given the derived radial density profile power law $B \sim 3/2$. We calculated a detailed energy budget for the cold spot shown in Fig. 1, with expected kinetic energy input K compared to the potential energy ΔU required to change the density profile as manifested in ΔH :

$$\Delta U / g = (\rho_0 - \rho_s)(d'H' - d_0H_0) + \frac{\rho_0}{2}(d_0^2 - d'^2)$$

$$K / g \approx \frac{\rho_s}{2} t(r)r$$

where H_0 is the background H-parameter value, d_0 is the initial depth of the column, and the new depth is given by

$$d' = d_0 + \frac{\rho_0 - \rho_s}{\rho_0} \Delta H$$

We make three basic assumptions: 1) the total change in the effective density profile occurs within the top meter of soil, 2) for the density profile $\rho_s = 1000 \text{ kg/m}^3$ and $\rho_0 = 1800 \text{ kg/m}^3$, and 3) the background H-parameter is 7 cm.

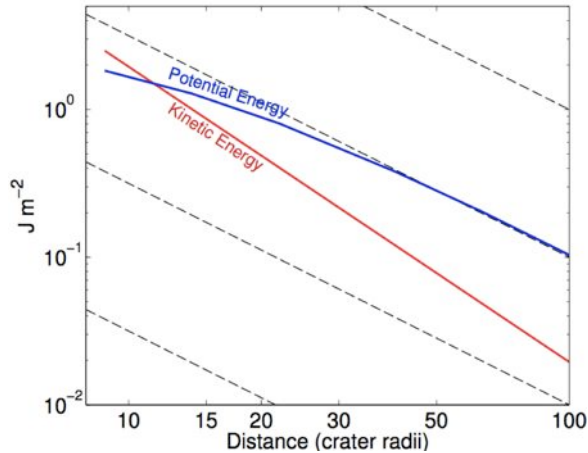


Figure 3: Log-log plot of available kinetic energy from ballistic ejecta particles, and change in potential energy due to regolith decompression for the cold spot in Fig. 1.

Fig. 3 shows the dominance of kinetic energy deposition close to the crater and a deficit beyond $\sim 10 R_c$. The imbalance of imparted kinetic energy and potential energy change provides insight about the possible cold spot formation mechanisms. The excess change in po-

tential energy must come from a redistribution of the thermal and kinetic energy of the impactor. In order to test the possibility of a collisional cascade pushing the kinetic energy radially outward in order to made up for the discrepancy of potential energy, we developed a soft sphere discrete element model (SSDEM). The model follows the methodology of Kruggel-Emden [8], tracking particles to understand how ballistic impact velocity affects the directionality and energy of the tertiary ejecta particles.

From the experiments of Salisbury *et al.* [9], we can assert that particles reaching a maximum height < 10 cm will cause net decompression of the regolith. We ran an ensemble of models to test for the maximum height of a collision chain of 10,000 particles and performed a statistical analysis of the results. We also ran the SSDEM with variable secondary impact angles and velocities to understand the change in response from the regolith. The results suggest that as particles travel further, the tertiary ejecta become radially? symmetrical. The power law for $\Delta H(r)$ derived strictly from the SSDEM maximum height resulted in a power of $\beta \sim 1.2$ versus the actual 1.5 from the Diviner data. This similarity suggests ballistic cascading remains a viable explanation for the cold spots, though a more complete dynamical model including thermal dissipation and melting could yield more accurate results.

Conclusions: Data from Diviner show that lunar cold spots display a remarkably consistent power law behavior in their radial regolith density profiles, with $\log H(r) \sim -3/2$. This consistency argues for a common formation mechanism. Our preliminary results suggest ballistic cascading is a plausible formation mechanism for cold spots. The SSDEM methodology presents a novel way of investigating impact cratering through the complex process of particle collisional cascading. The effect yields a behavior which could account for the “pushbrooming” of fluffed regolith in distal regions.

References: [1] Paige D. A. et al. (2010), *Space Sci. Rev.*, 150, 125, [2] Bandfield J. L. et al. (2014) *Icarus*, 10.1016/j.icarus.2013.12.017, [3] Bandfield J. L. et al. (2011) *J. Geophys. Res.*, 10.1029/2011JE003866, 2011. [4] Vasavada et al., 2012, [5] Hayne, P. O. (2013). *BAAS* 45, #9, 107.3, [6] McGetchin T. R. et al. (1973) *Earth and Planet. Sci. Lett.*, 20, 226-236, [7] Lucey P. G. et al. (2000), *J. Geophys. Res.*, 105, [8] Kruggel-Emden H. et al. (2007) *Powder Technology*, 171, 157-173, [9] Salisbury J. W. and J. E. M. Adler (1967), *Nature*, 214, 156-158.

XRD PATTERNS OF SHOCKED AND ALTERED BASALTS AS ANALOGS FOR MSL CHEMIN DATA

B.W. Wernette¹, S.P. Wright¹, and W.H. Farrand²; ¹Department of Geology and Geography, Auburn University, Auburn, AL 36849; ²Space Science Institute, Boulder, CO 80301; Ben.Wernette@auburn.edu

Brief Summary: A database of XRD patterns of basalt with ranges of both alteration state and shock level is being created to compare to hydrovolcanic glasses and interpret XRD data from Mars.

Introduction: X-Ray Diffraction (XRD) is an analytical technique used to determine the mineralogical composition of crystalline materials. Atoms in crystalline materials are arranged in a regular pattern and X-rays, generated by a cathode ray tube [1] in an X-ray Diffractometer, interact with atoms in the material studied. The wavelengths of the x-rays used are on the order of 1 to 2 angstroms, similar to the spacing between atoms in most minerals [1]. This relationship allows x-rays to effectively be diffracted by the atoms that compose a crystal. Bragg's equation [1] describes the relationship between incident X-rays and a crystal lattice. The interaction between x-rays and a material create constructive interference, which can be compared with a database of XRD patterns of known materials.

The Mars Science Laboratory (MSL), or "Curiosity" is equipped with a Chemistry and Mineralogy instrument (CheMin). CheMin is an onboard instrument capable of using X-ray diffraction to analyze the Martian fines, soils, and rocks [2]. Morris et al. [3] discussed Curiosity's most recent task of analyzing the Rocknest soils of the Gale crater. Their analysis showed that along with volatiles, the Rocknest soil contains 27 +/- 14 weight percent X-ray amorphous material [3]. Although it is not known whether these amorphous materials are of volcanic or impact origin, analysis of our terrestrial analogs may provide information that can be used to describe these amorphous materials.

Samples representing hydrovolcanic glasses and fresh/altered/shocked basalts were provided. Samples from Lomar Crater, India are unique in that they provide examples of both shocked and altered basalt [4]. Lomar Crater is a Pleistocene aged (~570 ka) impact crater located in India. This crater provides an analogy to the Martian surface with a history of basaltic volcanism, aqueous alteration, and shock [5]. Hydrovolcanic samples, or "tephras", are from the interaction of basaltic lava flows and groundwater circa the Snake River Plains of southern Idaho [6].

Methodology: A mortar and pestle was used to grind the samples to powders for homogeneity and a proper representation of the bulk sample. After preparation, samples were placed into a glass Bruker specimen holder. For analysis, the samples were placed into a Bruker D2 Phaser, a desktop X-ray diffractometer. Samples were analyzed for an effective total time of

approximately 22 minutes. Analysis started with a two theta value of five degrees, and ended with a two theta value of ninety degrees. Data was collected in 4,205 steps with an interval time of 0.3 seconds. After analysis, samples were saved and cataloged according whether they were tephra/hydrovolcanic or impact melt in origin. Some XRD patterns were analyzed for mineralogical content (**Figures 1, 3, and 4; Table 1**).

Petrographic images (**Figure 2**) of the bulk sample (not powders) were taken for a level of sample characterization that can't be done with rocks and soils encountered by MSL. The main objective of petrography is to identify and estimate the abundance/amount of amorphous glass, all alteration products – both amorphous and crystalline, and primary igneous minerals to compare to current and future XRD results.

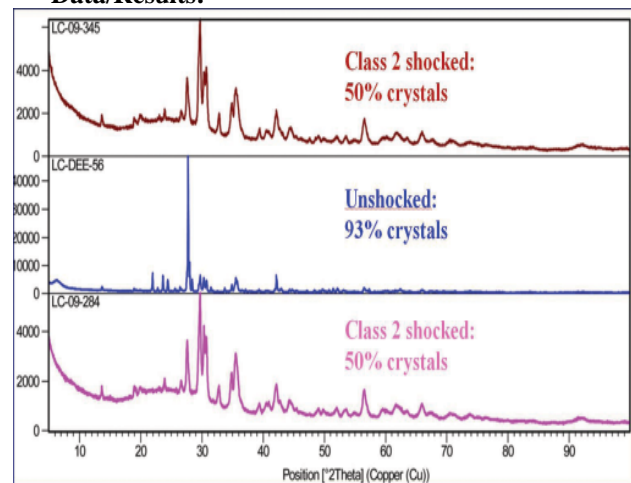
Data/Results:

Figure 1: Two Class 2 shocked basalts [4,5] have lower counts and less crystallinity (and thus more amorphous materials) than unshocked basalt.

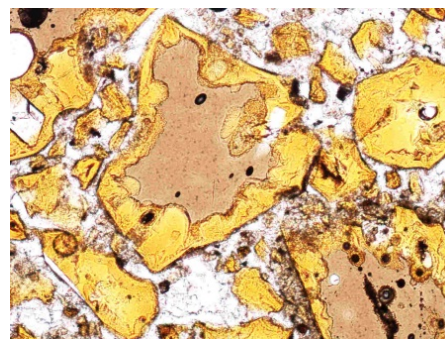


Figure 2. Petrography in PPL of NMB12-07 (see Figure 3 and Table 1) showing brown glass surrounded by a yellow isotropic material (in CPL not shown here).

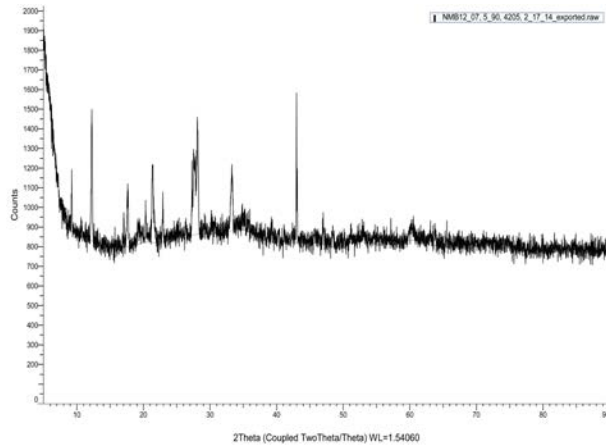


Figure 3: X-ray diffraction pattern of hydrovolcanic sample NMB12-07 from North Menan Butte, Idaho.

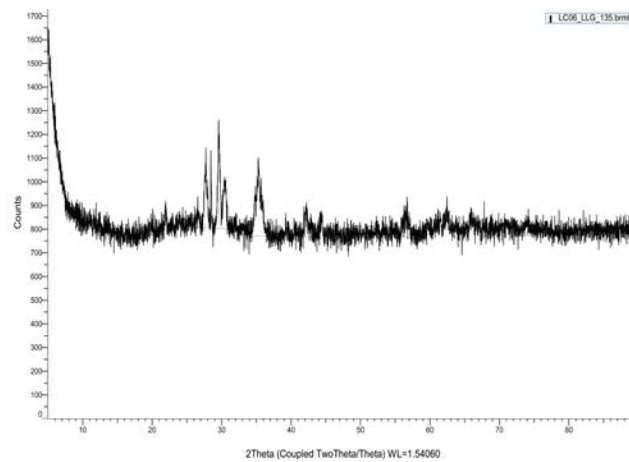


Figure 4: X-ray diffraction pattern of impact melt sample LC06-LLG-135.

Discussion: We made some comparisons between XRD patterns, the limited/preliminary resulting mineralogy data from those patterns, and the abundance of crystalline materials (vs. amorphous) in the glasses and basalts. In Figure 1, the XRD counts are lower for Class 2 shocked basalts [4,5] than unshocked Deccan basalt. Also seen in Figure 1 is a reduction in crystallinity and an increase in the amount of amorphous materials. As the primary difference between unshocked basalt and Class 2 shocked basalt is the conversion of labradorite plagioclase feldspar to maskelynite, we suggest that this conversion of tectosilicate feldspar to glass is the reason for 43% difference in crystallinity, as Deccan basalt typically contain ~45% labradorite.

Several XRD patterns were analyzed for insight into what alteration products are present, with the goal being to compare the alteration products of hydrovolcanic glass to the alteration products of impact melt glass (“Class 5” [4]) and Class 2 shocked basalt. Figures 3 and 4 show the XRD patterns for one hydrovolcanic

glass and one impact melt, respectively, and Table 1 displays the alteration minerals returned. Smectite, a common alteration product of basalt, was found in all four samples, whereas the zeolite philipsite was found in the two hydrovolcanic tephra. Secondary quartz and albite were found in a Class 2 shocked basalt, but these silicates may have been aqueously deposited in ~65 Ma Deccan basalt before shock metamorphism ~570 ka.

An examples of our petrographic images is shown in plain polarized light (PPL) as Figure 2. The hydrovolcanic glass NMB12-07 (also shown as Figure 3 and in Table 1) shows brown glass surrounded by a yellow material we interpret as palagonite. The same view is ~99% isotropic in cross polarized light (not shown here). Similarly, petrography of Lonar impact melts (*i.e.*, Figure 4 and Table 1) show brown and yellow glasses in PPL, and are completely isotropic in CPL [4].

Table 1. Preliminary results of alteration products

Sample:	Type:	Alteration Minerals:
LC09-235	Class 2 shocked basalt [4]	Smectite, Quartz, Albite
LC06-LLG-135	impact melt	Smectite, Calcite
NMB12-03	hydrovolcanic tephra	Smectite, Calcite, Philipsite
NMB12-07	hydrovolcanic tephra	Smectite, Calcite, Philipsite

Future Work: We are comparing the XRD patterns and their analyses of primary and secondary alteration minerals for the hydrovolcanic, shocked, and altered basalt samples. As more data is collected we hope to develop a better understanding of the alteration process seen in both hydrovolcanic and shocked basalts. Ultimately, a data base of XRD patterns representing analogs to Martian processes can be compared to CheMin data for a better understanding of amorphous materials in soils and rocks, including glasses and their alteration products.

References: [1] Nesse W. D. (2011) “*Introduction to Mineralogy*” [2] Zimmerman et al. (2013) IEEE/AIAA, #2062 [3] Morris et al. (2014) LPSC, #1319 [4] Kieffer et al. (1976) 7th LPSC, 1391-1412; Wright et al. (2011) *JGR-Planets*, doi:10.1029/2010JE003785 [5] Wright and Newsom (2012) LPSC, #2765 [6] Farrand et al. (2014) LPSC, #1597

SEARCH FOR ULTRA-CARBONACEOUS PARTICLES IN THE INTERPLANETARY DUST COLLECTION. H. Wiesman^{1,2}, C. Floss^{1,2}, P. Haenecour^{1,3}, and A. Wang.³ ¹Laboratory for Space Sciences; ²Physics Department; ³Department of Earth & Planetary Sciences, Washington University, St. Louis, MO, USA (Email: floss@wustl.edu, hwiesman@wustl.edu)

Introduction: Micrometeorites dominate the flux of extraterrestrial material accreting to the Earth [1] and are an important complement to other types of extraterrestrial samples, such as meteorites and interplanetary dust particles (IDPs). Ultra-carbonaceous Antarctic micrometeorites (UCAMMs) are fine-grained fluffy particles dominated by highly disordered carbonaceous matter [2, 3] enclosing high temperature anhydrous minerals and GEMS-like aggregates [4, 5]. These characteristics, the presence of H and N isotopic anomalies, and abundant presolar grains [4-7] suggest similarities to anhydrous IDPs and primitive carbonaceous chondrites.

The presence of these primitive ultra-carbonaceous particles in the Antarctic micrometeorite collection led us to question whether similar particles may be present in the interplanetary dust collection. After collection in the stratosphere, particles on the collectors undergo preliminary SEM-EDX analysis in order to distinguish true IDPs from likely terrestrial contamination. Among the different types of terrestrial contaminants found on the collectors are numerous particles whose spectra suggest that they are dominated by low atomic number (Z) elements that are typically not detectable by EDX methods (e.g., H, C, N, O). Although classified as terrestrial contaminants, some of these particles may in fact be extraterrestrial ‘low-Z’ IDPs [8], similar to UCAMMs. Here we report the results of a survey of low-Z particles from the JSC cosmic dust collection that we carried out in order to evaluate this possibility.

Experimental: We mounted 22 low-Z particles from eight different collectors (L2008, L2009, L2021, L2036, L2047, U2097, U2098, W7190) on high purity Au foil for elemental and isotopic characterization. Secondary electron images and EDX spectra of the particles were obtained with a JEOL 840a SEM equipped with a LaB₆ emitter and a ThermoNoran Si(Li) light element detector.

Several particles, which appeared most similar to UCAMMs or fine-grained IDPs, were chosen for NanoSIMS analysis to search for isotopically anomalous components. Raster ion imaging of the C and O isotopes, followed by imaging of the C and N (as CN⁻) isotopes, was carried out in multi-collection mode with a Cs⁺ primary ion beam. Analytical methods and data reduction followed standard procedures for presolar grain searches [9].

Raman spectra were obtained on the same seven particles with a state-of-the-art inVia Laser Raman Imaging system [10] using a 633 nm laser wavelength.

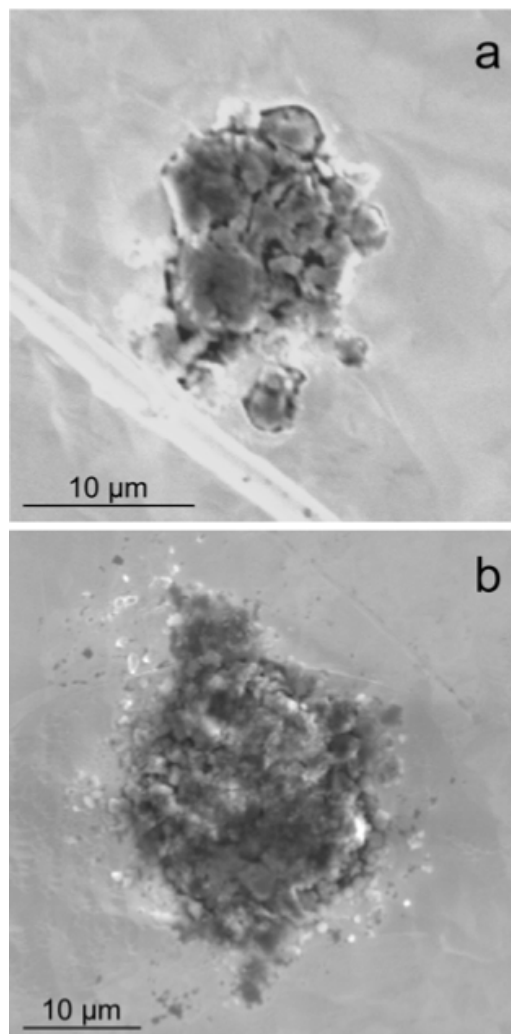


Figure 1. Secondary electron images of ‘low-Z’ particles L2008 H2 (a) and L2008 C7 (b).

Results: As expected, C and/or O were dominant elements in virtually all of the EDX spectra obtained; many of the spectra also displayed the presence of Na. Other elements found in some of the particles included Al, Si, Fe, Mg and occasionally K, Ca, or S. From our set of 22 particles, we selected seven for further analysis on the basis of their textures and/or elemental compositions (Figs. 1, 2). Four of the particles have EDX spectra dominated by C, with essentially no other elements present; texturally, they either consist of aggregates of fine-grained particles or have smooth

uniform morphologies. The other three particles have typical ‘chondritic’ spectra [11], with abundant Fe, Mg, Al and Si, in addition to C and O; S is also present in two of them. All three are aggregates of fine- to medium-grained particles. Particles whose EDX spectra contain Na or K are likely to be terrestrial in origin and were not considered further.

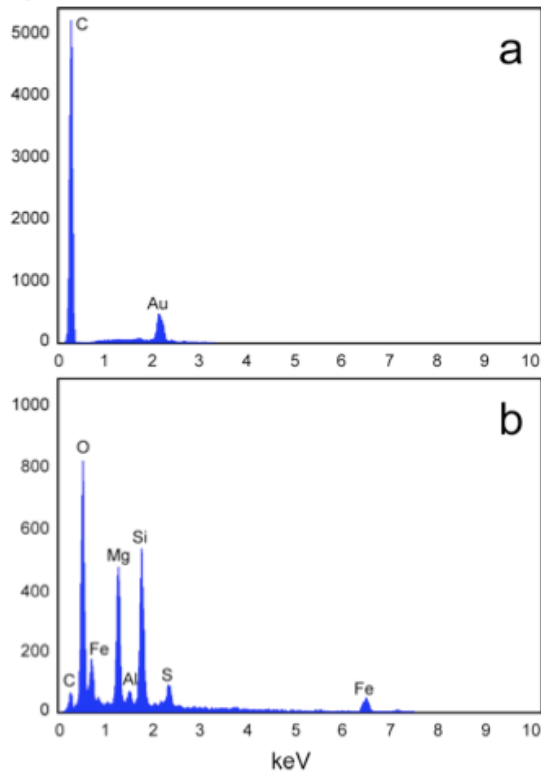


Figure 2. Energy dispersive X-ray spectra of two ‘low-Z’ particles. L2047 B12 (a) and L2008 H2 (b).

The Raman spectra show that all of the particles contain prominent first-order D and G band peaks (Fig. 3). In four of the particles the peaks have sharp and narrow features indicative of disordered graphite [e.g., 12]; these particles also exhibit second-order C peaks at 2662 cm^{-1} . These are the same four particles whose EDX spectra consist primarily of C only (e.g., Fig. 2a).

The D and G band peaks in the other three particles are broader and resemble those of meteoritic insoluble organic matter (IOM) [13-15]. These three particles all have chondritic spectra (e.g., Fig. 2b) and fine-grained textures (e.g., Fig. 1). Two different regions of particle L2008 H2 were measured. In addition to the D and G band peaks, one of the spectra (H2-1) shows a peak at 669 cm^{-1} , consistent with the presence of phyllosilicates. The other spectrum (H2-2) has a small peak at 2139 cm^{-1} , which may indicate a -CN functional group [e.g., 15].

NanoSIMS ion imaging did not show the presence of any isotopic anomalies for C, N, or O.

Conclusions: Our survey showed that, as expected, many of the particles classified as ‘low-Z’ appear to be terrestrial contaminants. However, several of them have characteristics that are consistent with an extraterrestrial origin. Specifically, particles L2008 C7, L2008 H2 and L2047 E39 have chondritic elemental compositions, fine-grained textures and Raman spectra consistent with the presence of IOM. The lack of presolar grains, or other isotopically anomalous components, precludes a definitive categorization of these particles. However, after additional NanoSIMS ion imaging of C, N, and O, and the further absence of isotopic anomalies, it is unlikely that these particles have an extraterrestrial origin.

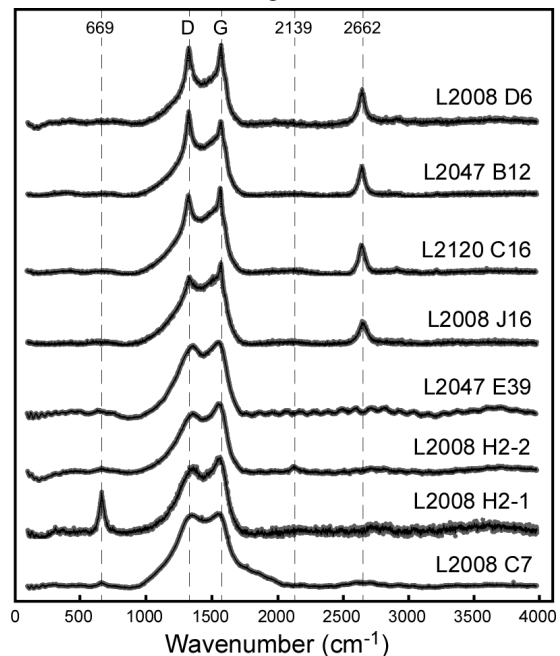


Figure 3. Raman spectra of ‘low-Z’ particles.

References: [1] Love S. G. and Brownlee D. E. (1993) *Science* 262, 550. [2] Nakamura T. et al. (2005) *MAPS* 40, A110. [3] Dobrica E. et al. (2011) *MAPS* 46, 1363. [4] Floss C. et al. (2012) *LPSC XLIII*, #2247. [5] Dartois E. et al. (2013) *Icarus* 224, 243. [6] Duprat J. et al. (2010) *Science* 328, 742. [7] Floss C. et al. (2013) *MAPS* 48, #5230. [8] Cosmic Dust Catalog Vol. 15. [9] Floss C. and Stadermann F. J. (2009) *GCA* 73, 2415. [10] Du H. and Wang A. (2012) *LPSC XLIII*, #2221. [11] Floss C. et al. (2006) *GCA* 70, 2371. [12] Wopenka B. et al. (2013) *GCA* 106, 463. [13] Busemann H. et al. (2007) *MAPS* 42, 1387. [14] Bonal L. et al. (2007) *GCA* 71, 1605. [15] Dobrica E. et al. (2011) *MAPS* 46, 1363.

This work is supported by NASA grant NNX10AI64G (C.F.).

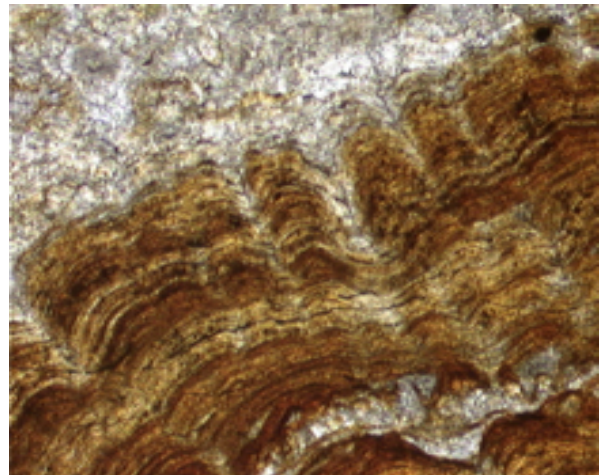
Abstract: The rapid mineralization of carbonates from Crystal Geyser promotes the capture and preservation of cellular and extracellular remains of microbial communities living within the spring environment. Petrographic thin sections cut from teracettes show complex laminar structures reminiscent of larger stromatolite formations found throughout the fossil record. X-ray Powder Diffraction (XRPD) and petrographic studies reveal major mineral phases of aragonite, calcium carbonate, and possible silica polymorphs. Microscopic photography shows some evidence of fossilized cells and extracellular fabric. Such studies help lay a foundation for identifying the most promising sites to explore for a fossil record on Mars, and in the ancient fossil record on Earth.



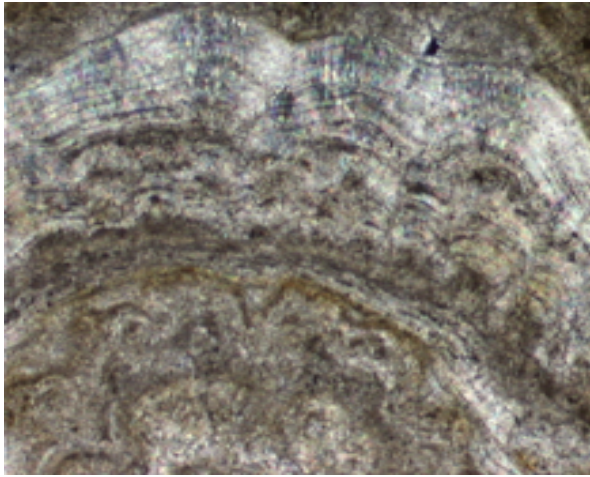
Figure 1: Crystal Geyser viewed from Green River (scale length ~30m).



Figure 2: Close up view of terracettes approximately 3-5 cm wide.



Figures 3 (left) & 4 (right): Laminae show color banding due to variations in Fe-oxide concentrations. Wavy laminations are cross sectional views of microcolumnar forms composed of fibro-radial aragonite. Scale lengths: fig. 3 is ~2.3 mm, fig 4 is 0.4 mm.



Figures 5 (left) & 6 (right): Laminations under cross polarized light. Minerals comprising the laminations have an internal fibroradial microfabric and exhibit a high birefringence, consistent with aragonite. Scale lengths ~0.2 mm.

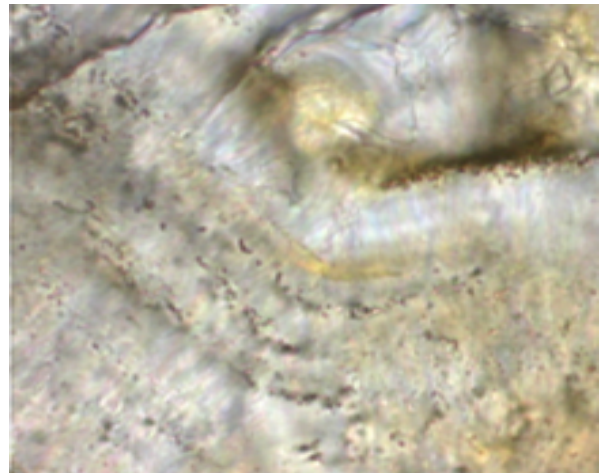
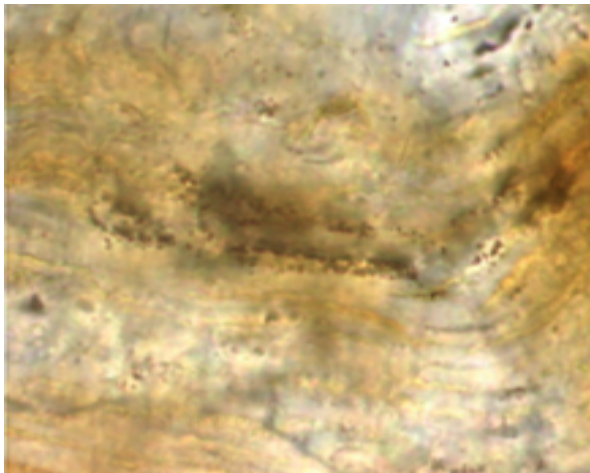


Figure 7 (left) & Figure 8 (right): Clusters of spherical structures embedded along laminations, interpreted to be coccoid forms of bacteria, probably cyanobacteria. Scale length ~450 μm .

